JAERI-M
88-014

JAPANESE CONTRIBUTIONS TO IAEA INTOR WORKSHOP, PHASE TWO A, PART 3

CHAPTER I : INTRODUCTION
CHAPTER II : SUMMARY

February 1988

Sigeru MORI, Ken TOMABECHI, Noboru FUJISAWA
Hiromasa IIDA, Toshihide TSUNEMATSU, Takeshi KOBAYASHI
Tadanori MIZOGUCHI[*1], Bunko IKEDA[*2], Tsutomu HONDA[*3]
Masayoshi SUGIHARA and Ryusei SAITO

日本原子力研究所
Japan Atomic Energy Research Institute

JAERI-Mレポートは，日本原子力研究所が不定期に公刊している研究報告書です。
入手の問合わせは，日本原子力研究所技術情報部情報資料課（〒319－11茨城県那珂郡東海村）あて，お申しこしください。なお，このほかに財団法人原子力弘済会資料センター（〒319-11茨城県那珂郡東海村日本原子力研究所内）で複写による実費頒布をおこなっております。

JAERI-M reports are issued irregularly.
Inquiries about availability of the reports should be addressed to Information Division, Department of Technical Information, Japan Atomic Energy Research Institute, Tokai-mura, Naka-gun, Ibaraki-ken 319-11, Japan.

編集兼発行　日本原子力研究所
印　　刷　日立高速印刷株式会社

JAERI-M 88-014

Japanese Contributions to IAEA INTOR Workshop, Phase Two A, Part 3

Chapter I : Introduction

Chapter II : Summary

Sigeru MORI,[+1] Ken TOMABECHI,[+2] Noboru FUJISAWA, Hiromasa IIDA
Toshihide TSUNEMATSU,[+3] Takeshi KOBAYASHI, Tadanori MIZOGUCHI[*1]
Bunko IKEDA,[*2] Tsutomu HONDA,[*3] Masayoshi SUGIHARA AND Ryusei SAITO

Department of Large Tokamak Research
Naka Fusion Research Establishment
Japan Atomic Energy Research Institute
Naka-machi, Naka-gun, Ibaraki-ken

(Received January 18, 1988)

This report corresponds to Chapter I and II of Japanese contribution report to IAEA INTOR Workshop, Phase Two A, Part 3. The major objectives of the INTOR Workshop Part 3 are to evaluate innovative ideas which would significantly improve the tokamak concept, to study new-selected critical technical issues, that affect the feasibility or practicability of the INTOR concept, to assess scientific and technical data bases, and to conduct critical analyses of the existing INTOR-like designs with the aim of preparing a useful information base for future design work for ITER. To perform the innovations, critical issues, and data base, the following six groups are organized; (A) Impurity control, (B) Operational limits and confinement, (C) Current drive and heating, (D) Electromagnetics, (E) Configuration and maintenance, (F) Blanket and first wall. In addition to

---

+1 Vice President of JAERI
+2 Director General of Naka Fusion Research Establishment
+3 Department of Thermonuclear Fusion Research
*1 On leave from Hitachi, Ltd.
*2 Mitsubishi Atomic Power Industries, Inc.
*3 Toshiba Corporation

those groups, the two disciplinary groups are also organized to do the critical analyses of the existing INTOR-like designs; (G) Physics and (H) Engineering.

Keywords: INTOR, Summary of Japanese Contribution, Tokamak, IAEA, Phase Two A Part 3.

IAEA INTORワークショップフェーズⅡA，パート3報告書

第Ⅰ章： 序
第Ⅱ章：サマリー

日本原子力研究所那珂研究所臨界プラズマ研究部
森 茂[+1]・苫米地 顕[+2]・藤沢 登・飯田 浩正
常松 俊秀[+3]・小林 武司・溝口 忠憲[*1]・池田 文構[*2]
本多 力[*3]・杉原 正芳・斎藤 龍生

（1988年1月18日受理）

この報告書はIAEA主催のINTORワークショップ，フェーズⅡA，パート3の日本の報告書の第Ⅰ章と第Ⅱ章に相当するものである。INTORワークショップ，フェーズⅡA，パート3の主目的は，トカマク炉概念の改善につながる斬新なアイデアを評価する事，INTOR概念の実現性に影響する新たな重要技術課題を検討する事，科学技術データベースの評価，ITERの設計作業に有効な情報となる既存のINTORクラスの設計を解析する事である。上記の作業を実施するために以下の8つのグループが組織された。(A)不純物制御，(B)運転限界と閉じ込め，(C)電流駆動と加熱，(D)電気磁気，(E)構造と保守，(F)ブランケットと第一壁，(G)物理，(H)技術。最後の2つのグループはITERの設計作業に有効な情報となる既存のINTORクラスの設計を解析するためのものである。

那珂研究所 ： 〒311-01 茨城県那珂郡那珂町大字向山801-1
+1 副理事長
+2 那珂研究所所長
+3 核融合研究部
*1 ㈱日立
*2 ㈱三菱
*3 ㈱東芝

PREFACE

This report summarizes the Japanese work performed for the INTOR Workshop during the period of September 1985 through November 1987. The work has been carried out by the Japan Atomic Energy Research Institute with extensive cooperation of universities and industries in Japan. I would like to express also my deep acknowledgement to the IAEA and the other three parties of the INTOR Workshop for their cooperation.

October 1987

S. Mori
Vice President
Japan Atomic Energy
Research Institute

Contents

Chapter I 1

Introduction 1
(S. Mori)

Chapter II 3

Summary 3
(K. Tomabechi)

1. Impurity control 3
(T. Mizoguchi)

2. Operational limits and confinement 20
(T. Tsunematsu)

3. Current drive and heating 40
(N. Fujisawa)

4. Electromagnetics 54
(B. Ikeda)

5. Configuration and maintenance 71
(T. Honda and H.Iida)

6. Blanket and first wall 83
(T. Kobayashi)

7. FER design philosophy 102
(N. Fujisawa and R. Saito)

8. Operational flexibility 122
(M. Sugihara)

9. System analysis of INTOR-like design 137
(H. Iida and T. Mizoguchi)

目　　次

第Ⅰ章 …… 1
序（森） …… 1

第Ⅱ章 …… 3
サマリー（苫米地）…… 3
1. 不純物制御（溝口）…… 3
2. 運転限界と閉じ込め（常松） …… 20
3. 電流駆動と加熱（藤沢）…… 40
4. 電気磁気（池田）…… 54
5. 構造と保守（本多，飯田）…… 71
6. ブランケットと第一壁（小林） …… 83
7. ＦＥＲ設計思想（藤沢，斎藤） …… 102
8. 運転計画の柔軟性（杉原） …… 122
9. ＩＮＴＯＲクラス装置設計のシステム解析（飯田，溝口） …… 137

Chapter I : Introduction

The Workshop of the International Tokamak Reactor, INTOR, started as a collaborative effort in January 1979 among Euratom, Japan, the USA and the USSR under the auspices of the International Atomic Energy Agency, IAEA.

The initial effort called the Zero Phase of the INTOR Workshop was conducted during 1979 to define the objectives and physical characteristics of the next major experiment after the existing large tokamaks of TFTR, JET, JET, JT-60 and T-15, and also to assess the technical feasibility of constructing such an experiment in around 1990. The result of the Workshop was published as the report of the Zero Phase Workshop [1]. The report concluded that an ingnited D-T tokamak was technically feasible provided that supporting R&D would be properly carried out.

As a result of the Zero Phase Workshop, the INTOR Workshop was advanced to the Phase One, in order to develop a conceptual design of the INTOR experiment. The Phase One Workshop completed the conceptual design in 1981, proposing a concept of tokamak having a fusion power of 620 MW. The result of the Phase One Workshop was published in an IAEA report [2].

Then, the INTOR Workshop was advanced to Phase Two A in July 1981 in order to review critical technical issues which were identified during Phase One Workshop. The Phase Two A was extended twice so that the Workshop activities were conducted in the three parts, Part I from July 1981 until the end of 1982, Part Ⅱ covering 1983 to mid 1985 and Part Ⅲ covering mid 1985 to the end of 1987.

During Part I, review was conentrated on issues of plasma performance, impurity cotnrol and first wall, testing requirements, tritium and blanket, mechanical configuration, magnetics and electromagnetics, and cost-risk-benefit. The result of Phase Two A Part I was published in an IAEA repot [3].

Part Ⅱ concentrated on issues of impurity control, RF heating and current drive, transient electromagnetics, maintainability, technical

benefit of component design and fabrication for international collaborative programme. The result of Part Ⅱ Workshop was published as an IAEA report [4].

Part Ⅲ was started in order to investigate issues of impurity cotrol, beta and confinement, heating and current dirve, electromagnetics, configuration and maintenance, first wall and blanket, DEMO requirements, potential innovations for improvement of tokamak concept, and updating INTOR conceptual design. During the course of Part Ⅲ, negotiation for a new international collaborative activity for joint conceptual design of ITER was initiated, so that a part of INTOR Workshop activities was reoriented, resulting in a replacement of updating of INTOR conceptual design by critical analysis of existing INTOR-like designs, which will be used as useful information for ITER activity.

During the Workshop of Part Ⅲ, the work has been carried out, as traditional with the INTOR Workshop, by teams of experts working in their home countries under the direction of the INTOR participants, who met in Vienna periodically.

The results of the Japanese work contributed to the INTOR Workshop during Part Ⅲ are contained in this national report. The work in Japan was carried out by the Japan Atomic Energy Research Institute, JAERI, with the support of the industries; i.e. Toshiba Corp., Hitachi Ltd., Mitsubishi Group and Kawasaki Heavy Industry Co., under contracts between them and JAERI.

Many of the scientists and engineers contributed to the work in Japan were involved also in designing the Fusion Experimental Reactor, FER, a next step machine being studied at the JAERI. Thus, many results derived from designing the FER were contributed also to the INTOR Workshop.

The numberings most of the chapters and sections of this report were made identical to those which will be used in the IAEA Phase Two A Part Ⅲ report, in order to facilitate the readers of this national report.

Chapter II : Summary

1. IMPURITY CONTROL

The impurity control studies during the Phase IIA Part 3 [5] have mainly carried out, (1) an assessment of the experimental and engineering data base for impurity control system based on current experiments, (2) an evaluation of five innovations brought up at the specialist meeting on Jan. 1986 [6], and (3) design studies using sophisticated computational models to extrapolate to the operating parameters and performance of INTOR-like designs. The Impurity Control Physics group have concluded and recommended that the poloidal divertor concept either single null or double null be retained as the reference impurity control system for the INTOR reference design. The pumped limiter concept would remain as a back-up option of the impurity and particle control system for INTOR if this concept could be dimonstrated successfully in experiments.

Five innovations were proposed for the INTOR impurity control system [6], 1) impurity flow reversal, 2) radiatively cooled edge, 3) ergodic limiter, 4) helieum burial, and 5) liquid metal divertor target. It is recommended that further studies for helium burial and liquid metal divertor plates be pursued because of the possibility of near-term applications of those materials. Further studies for other three are encouraged, but required to demonstrate their advantages sufficiently clear before justifing their inclusion in the INTOR design.

As Japanese contributions [10], recent experimental results from JT-60, JFT-2M, JIPPT-IIU and Heliotron-E are presented during INTOR workshop. Experimental results in JT-60 show that a poloidal divertor configuration is very effective for impurity and particle control in a large tokamak. The diffusion coefficient of D = (0.6-1.0) m^2/s observed at JT-60 core plasma is good agreement with those observed at JET and TFTR. JFT-2M tokamak found H-like transitions not only in the open divertor configuration but also in D-shaped limiter bounded plasmas. They also found that H-transition does not depend on heating methods. H-mode discharge, however, are often terminated by the impurity radiation losses. These observations suggest that the compatibility of improved particle confinement and impurity removal from core plasma may be a problem with H-mode discharges.

For design studies, refinement of the model being implemented is the most important task. It has been newly developed two types of two-dimensional fluid code: the one solved by the finite element method and the other solved by the Partice In Cell (PIC) method for numerical treatments. Validation of the latter code is reported by simulating the boundary plasma conditions in Doublet III divertor experiments. The simulation is in satisfactory agreement with the experimental data from DIII. With this code, the preliminary calculation for the INTOR-like divertor plasma revealed that divertor operation of high density and low temperature divertor plasma is possible at a real geometry of open divertor configuration. The electrostatic particle model for divertor plasma is also developed. Several suggestions were made to the fluid model from the particle simulation studies.

1.1 Assessment of experimental data base

JT-60

The major impurities in JT-60 were oxygen, carbon and titanium which were the coating materials of the first wall. A slight amount of nickel, iron and chronium which are constituents of Inconel vessel and linear substrates are observed in divertor discharges. The molibdenum which is TiC coated limiter substrates are also identified in limiter discharges. In ohmically heated discharges the amount of titanium was around 1×10^{-3}% and 8×10^{-3}% at $\bar{n}_e=2\times10^{19}$ m^{-3} in hydrogen and helium discharges, respectively. For NB heated hydrogen plasmas the titanium concentration is about two time higher than that in ohmically heated plasmas. And the quantities of nickel, iron and chronium were below 1/10-1/100 of that of titanium.

The ratio of the light impurity density to proton density is 1.2% or 2.4% if the species are assumed to be totally oxygen or carbon, respectively. The averaged Z_{eff} falls smoothly with the increase of the electron density and minimum Z_{eff} is about 1.5 at $\bar{n}_e \simeq 5\times10^{19}$ m^{-3} as shown in Fig. 1.1. The value of Z_{eff} for NB heated plasmas were slightly larger than that of ohmically heated plasmas.

Fig. 1.2 shows a dramatic effect of the divertor in reducing the radiation loss in the NB-heated and ohmically heated plasma. The radiation loss from the main plasma, P_{rad}, is typically 5-10% of the absorbed power, P_{abd}, in divertor discharges and 30-90% in limiter

discharges. The evidence shows that the divertor is particulary effective in reducing the radiation loss of the NB-heated plasmas. The particle loss in the plasma during the NB heating is enhanced and efficiently transported to the divertor chamber through the relatively narrow divertor throat. Radiation loss in divertor chamber is analyzed by the 2-D fluid model, as shown in Fig. 1.3. Considering the ambiguity of the main and scrape-off plasma parameters, the simulated radiation loss power is in satisfactry agreement with the experimental values.

The neutral particle pressure in divertor chamber was measured with a shielded, fast ionization gauge in a pumping duct connected to the divertor chamber. Compression raties of the neutal pressure of 30 to 40 with ohmic heating and 40 to 60 with NB heating were observed, as shown in Fig. 1.4. The pressure in the divertor chamber indicate to proportional to the square of $\bar{n}_e$. These observations in JT-60 indicate that a poloidal divertor configuration is a good solution of the impurity and particle control system for the INTOR design.

The diffusion coefficient in the core plasma were estimated to $D \simeq 1$ m^2/sec in ohmically heated plasma and $D \simeq 0.8$ m^2/sec and 0.6 m^2/sec in discharges with co- and counter- NB injection, respectively. Fig. 1.5 shows time evolution of soft x-ray diode array signals and TiXXI line intensity of a NB-heated plasma with co- and counter-injection. The line intensity simulated by 1-D transport code shows no significant difference in the impurity transport among those cases, and typically $D_A \simeq$ 0.6-0.8 m^2/sec. In JET and TFTR, the diffusion coefficient of $D \simeq 1$ m^2/sec are observed for impurities. This good agreement for the diffusion coefficient between three large tokamaks offers a reasonable data base on impurity transport for the INTOR-like design.

Disruption characteristics of JT-60 [9] are divided into three types by their causes, namely, 1) disruptions triggered by enhanced MHD activities induced at q_{eff} =2 and 3, 2) disruptions due to a critical density limit, and 3) disruptions caused by impurity introduction. NB heated discharges have suffered only from the type of disruptions caused by impurity introduction. A density limit in NB heated discharge has not yet been observed in JT-60 divertor operation. Plasmas heated by ICRF and LH (for current drive and electron heating) have also suffered from disruptions mainly caused by impurities. ICRF heated plasmas are quite susceptible to disruptions, even after an adquite conditioning.

However, the addition of NB heating completely suppresses the occurrence of disruptions. Probably the additional NB heating power may compensate for the radiation loss induced by impurities.

The maximum current decay rate tends to increase with increase of a plasma current. All data measured so far are below the design value of 380 MA/s. The decay rate for limiter plasmas tends to be larger than that for divertor plasmas.

Based on soft X-ray and PIN diode signals, the decay time for the central PIN diode signals is around 10-100 ms and a characteristic time which is the fastest decay rate at the start of decay is around 1-10 ms as shown in Table 1.1. The energy decay rate is expected to be in a same order as the decay rate of a PIN diode signal through a central plasma region. In TFTR and JET, the energy decay rate of ~0.1 ms, one order faster than that in JT-60, is observed [8,9]. The difference between JT-60 and the other two is not clear. Further studies are required since the faster energy decay rate give a significant impact on the first wall and divertor designs of INTOR-like devices.

JFT-2M

Recent additional heating experiments in JFT-2M have achieved the H-mode in the open divertor configuration with NBI heating. Furthermore, H-like transitions were observed not only in ICRF heated open divertor discharges but also in D-shaped limiter bounded plasma [11]. Improved energy confinement in the limiter plasma reveals that a diverted magnetic configuration is not the necessary condition for an H-transition. As the H-transition, temperature and density pedestals are suddenly formed before the total stored energy increases. This fact suggests that the energy and particle transport near the plasma edge are evidently improved at the H-transition. According to these observations it can say that the transport effects in the edge region of the plasma will determine the energy confinement property of the tokamak plasma. In JFT-2M experiments, H-mode discharges are often terminated by the radiation losses [10]. The emission of FeX does not increase but the emission of FeXV and FeXVIII increases exponentially during H-mode discharge as shown in Fig. 1.6. The emissions from the lower ionization state are depressed like the H_α signal, but the emissions from the higher ionization state increases. Impurity injection (Ar) experiments suggest that the increase in the density of these ions is due not to an

increase in the impurity influx but to improved particle confinement during the H-mode phase.

JIPPT-II U

It is demonstrated that the m=3/n=2 dominant helical field perturbation produced by toroidally localized multipole-field coils induces one or two mini-disruptions and that the 2/1 magnetic island is ergodized by these mini-disruptions. As a results, the temperature flattening process is interrupted and the major disruption is avoided.

The preliminary ergodic magnetic limiter experiments with the m=3/n=1 helical field perturbation are also reported. They observed that application of the local helical field perturbation result in the ergodization of the edge confinement region and favorable effect of suppressing impurity influx. The existance of the threshold of the ergodization was suggested from the dependence of the ergodization on the pulse hight and width of herical perturbations.

Heliotron E

Particle control with conventionals, pumped limiter is demonstrated. About 2-4% of the particles lost from the plasma are removed if the pump limiter is located inside the last closed magnetic flux surface. Little or no particle control is observed if the pump limiter is placed outside the last closed surface.

1.2 Innovations

As Japanese contributions [6], three innovations were proposed, (1) ergodic magnetic limiter, (2) radiatively cooled edge, and (3) liquid metal divertor plates.

Ergodic magnetic limiter (EML) has been considered one of possible impurity control systems in tokamaks for long time. Some concepts of EML had already been proposed in Phase One INTOR [2]. Recently, experimental efforts have been carried out at JIPPT-IIU and CSTN-II at the Nagoya University [10]. In CSTN-II experiments, they show that a set of local helical coils can produce the helical field of mode index around m/n, typically 10/1, specified by the structure of helical coils and the direction of herical coil current. A drastic change in the plasma potential was observed with the application of helical field

perturbation. The increse in the plasma potential was accompanied by the decrease in the local electron density. When the helical field applied the edge plasma contacts with the wall through the magnetic field lines in relatively short connection length. A rapid loss of electrons to the wall should be reduced to generate a positive plasma potential with respect to the wall because of the ambipolarity. The wall loading was found to be extremely nonuniform along the poloidal direction. A rotating helical field was succeeded in making a time averaged loading to the wall uniform along the poloidal and toroidal direction. In JIPPT-IIU as already discribed, the ergodization of the edge confinement region with the local helical field perturbation brought a favorable effect of suppressing impurity influx and decreasing edge plasma temperature. Theoretical calculations predict that the radial diffusion in the effectively ergodized magnetic field seems to be comparable with an anomalous diffusion coefficient. Further studies are encouraged at CNTS-II and JIPPT-IIU (also TEXT, TEXTOR and TORE-SUPRA).

The reactor potential of a radiatively cooled edge had been considered during INTOR Phase IIA part 1 workshop [3]. However the subject was raised again at the innovation specialist meeting [6]. During that period, an interesting operation region called 'detached plasma' in which most of input power was radiated at a narrow edge plasma boundary was found in TFTR [5]. Various model calculations showed that the thickness of the radiating layer was sensitive to assumptions made regarding cross field transport. Also, the radiative loss powers strongly depend on materials of limiter and first wall which are primary impurity sources. Using INTOR-like parameters and assuming carbon graphite as limiter and first wall materials, the possibility of the self-limited impurity production with radiatively cooled edge plasma are analysed intensively [10]. Cross field transport is assumed to be anomarous, $\chi_e \simeq 2\times10^{19}/n_e$ cm^2/s, D^A=0.4 for plasma and $D_K^A = -0.4\times(2r/r_p^2)$ for impurities. It is assumed that $\chi_i = 5\times\chi_i^{NC}$, neo-classical. In scrape-off layer, it is assumed that $\chi_e = \chi_i = D^A = D_A^K = D_B$, Bohn diffusion. These assumptions are based on recent experimental results in JT-60, JET and TFTR. The 70% of input power (or magic alpha power) are radiated at boundary region and 30% of that goes to limiter and first wall directely. The radiation losses due to carbon impurity are

rather small and the radiative layer are somehpw restricted to the narrow region of the limiter shadow. As a results edge plasma temperature at a limiter head is still about 80-100 eV at which erosion of the limiter due to physcial sputtering is very serious. Nevertheless, self-limited impurity production can be achieved with the carbon concentration of 1.2% and the averaged Z_{eff} of 1.5. For the reactor application, the thickness of the radiating layer must be taken into account by an increase in the size of the confinement vessel Besides, the impact of a radiating edge layer upon improved confinement issues should be examined.

1.3 Design studies

The reference design of the INTOR impurity control system is a single null poloidal divertor. For modeling of a diverted plasma, it had been used one dimensional fluid code with two dimentional neutral code. Assuming rather simple divertor geometry, the divertor operation with high density and low temperature divertor plasmas was found with an appropriate heat and particle flux to the region. However, it is necessary to include the radial diffusion process in the scrape-off layer for accurate estimation of particle and energy deposition on a divertor plate. Besides, it is important to analize the behavior of neutral particles in real divertor geometry. As critical issues during Phase IIA part 3, refinement of the model being implemented became a main subject.

Two type of two-dimensional time dependent fluid code have been developed. The first one is the complete two-dimensional fluid code solved by the finite elements method in the plasma equilibrium and real geometry including the scrape-off plasma, the periphery of the main plasma and the divertor plasma. This code being under development is assumed the toroidal axisymmetry under the rectangular toroidal coordinates.

The second one is also the two-dimensional fluid code but emplays Particle In Cell (PIC) method for numerical treatments (Appendix 4.3.2). The fluid flow channels in the scrape-off and divertor region can be applied from poloidal magnetic flux tubes obtained by equilibrium calculation. By the PIC method with a proper geometry, fluid behavior in the computational region is easily solved with free boundary

conditions. Free boundary condition means that the energy flux to the vacent cell across the boundary must vanish at the initial step of the PIC scheme. Transport of the core plasma, however, is not solved in the code. The appropriate particle flux Γ, energy flux Qe for electron and Qi for ion must be assumed at the boundary of the core plasma.

Coupled with two dimensional neutral transport code using Monte-Carlo method, the fluid equation and neutral gas transport are solved in the scrap-off and divertor plasma region. In the vacuum region, only neutral gas transport is solved. The neutral transport package in called every several tenth of the fluid calculation time cycle.

Validation of the above code is shown by simulating the boundary plasma conditions in Doublet III divertor experiments. The distribution of plasma temperature and density in the divertor region were calculated using prescribed values of the cross field transport coefficients (i.e. D=0.5 Bohm and $\chi_e = \chi_i = 4D$) and the input power (1MW) for various values of the plasma particle flow across the separatrix. The results of this calculation are in satisfactory agreement with the experimental data from DIII as shown in Fig. 1.7. It is pointed out that an important parameter besides transport coefficients is the distribution of the pitch angle of the field line B_e/B_T.

For modeling of divertor plasmas, the fluid model has usually been applied. However, it is not clear that the usual fluid equations can describe accurately the scrape-off layer and divertor plasma. By this means, it has been developed the electrostatic particle model which can express correctly the velocity distribution function and the self-consistant electrostatic field. The simulation model is based on a one-dimensional system parallel to the magnetic field.

As simulation results, it is found that Coulomb collisions play a very important role in supplying electrons with large velocities. The pre-sheath with the scale length of the system size is formed by the collisional relaxation of the velocity distribution as well as by the particle source. The ion heat conduction flux becomes important in a high-recycling plasma. This value is found to be much larger than that estimated by the ion temperature gradient.

Several suggestions were made to the fluid model from these studies. In usual analyses by fluid model, the boundary condition for

the flow velocity at the divertor plate is given by $V_{\parallel} = C_s$ where C_s is the sound speed. In a low recycling plasma, however, $V_{\parallel}$ exceeds C_s in the divertor region, while in a high-recycling plasma $V_{\parallel}$ is equal to C_s at the understream just behind the recycling region. It is usually assumed in fluid equations that both electron and ion temperatures are isotropic. The isotropy in the electron temperatuare is almost realized of in high collisionality, $\nu_* > 1$, where ν_* is defined by the ratio of the collision frequency to the bounce frequency of electron, because of effects of the trapping due to the sheath potential. On the contrary, anisotrpy in the ion temperature is large, even when $\nu_* >> 1$. Therefore the parallel temperature of ions, $T_{i\parallel}$, and perpendicular one, $T_{i\perp}$, should be treated separately in fluid equations. When particles are highly recycled near the plate and $V_{\parallel} << C_s$ in the divertor region, the ion heat conduction flux, q_i, becomes very important in the total heat flux.

The preliminary calculation of the INTOR-like divertor plasma is carried out by the newly developed two dimensional fluid code (solved by PIC method). In the simulation studies, the impurity flow equations are added, but the behavior of only He^{+1} ion is included. Assuming $Q_T = Q_e + Q_i = 60$ MW, $\Gamma_p = 1\times10^{22}$ s^{-1} or 3×10^{22} s^{-1}, and $\Gamma_{He} = 0.05\ \Gamma_p$, the maximum temperature T_e in the scrape-off layer is approximately 210 eV as shown in Fig. 1.8. T_e decreases to approximately 20 eV at the divertor plate. Electron density near the divertor plate builds up to $n_e \simeq 2\times10^{20}$ m^{-3} for $\Gamma_p = 1\times10^{22}$ s^{-1} and $n_e \simeq 6\times10^{20}$ m^{-3} for $\Gamma_p = 3\times10^{22}$ s^{-1}. These results indicate that the new code can reproduce the divertor operation with high density and low temperature plasma even in the real geometry. Further studies are encouraged with this code including impurity materials of divertor target and appropriate impurity production mechanism.

Table 1.1 Examples of time decay rates of a PIN diode signal from a plasma center. This decay rates is expected in same order of thermal energy quench time during disruptions.

Heating	Shot No.	t_D (ms)	t_D^* (ms)	I_P (MA)	Configuration
OH	2289 2319	27 40	11 2	2.0 2.0	Div.
IC	2466	16	1	1.5	Div.
LH	3747	26	2	1.5	Div.
LH+NBI	3938	8	2	1.0	Lim.

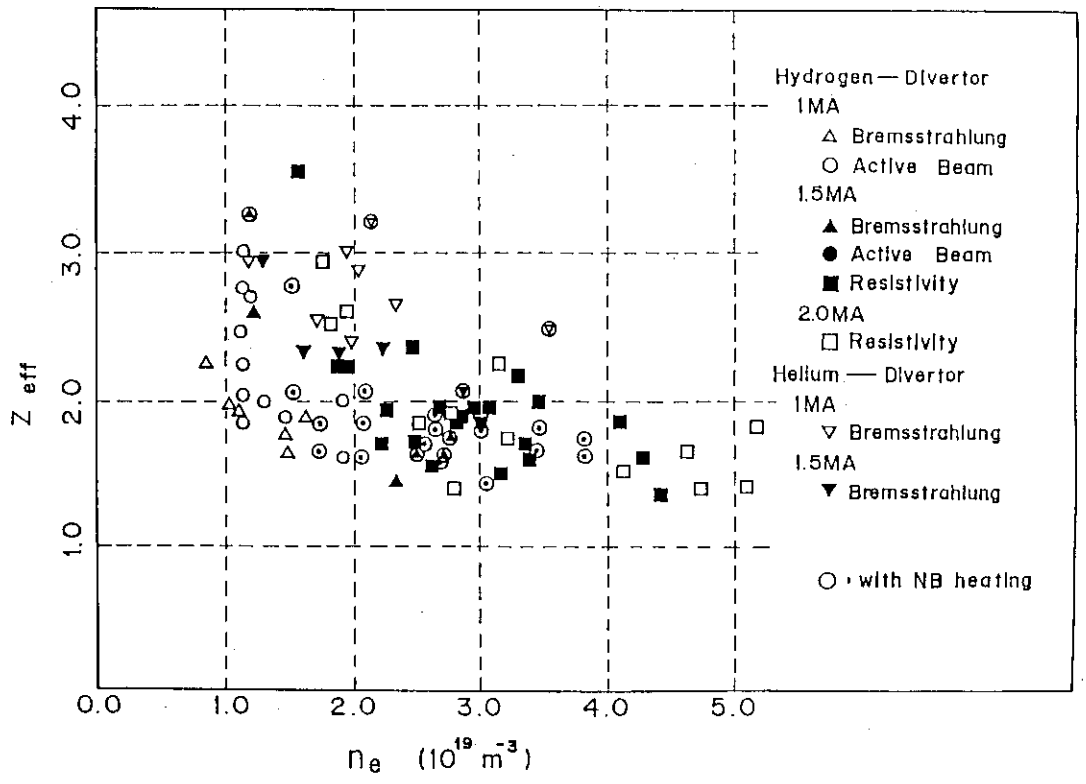

Fig. 1.1 Z_{eff} vs. $\bar{n}_e$ for ohmically heated and NB-heated plasma in JT-60. The relatively low Z_{eff}, less than 1.5, can be achieved with high electron density even in NB-heated plasmas.

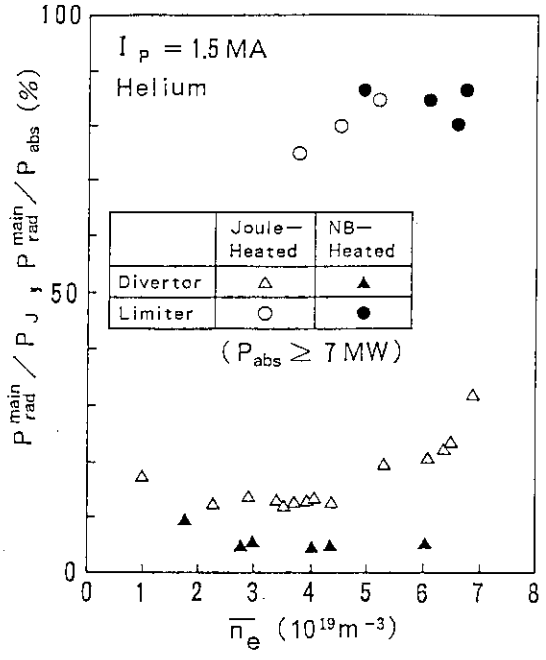

Fig. 1.2 $\bar{n}_e$ vs. radiation power fraction in main and divertor chamber with NB-heated plasma. The fraction of radiation power loss in main plasma over the input power is only 5-10% in NB-heated divertor plasma.

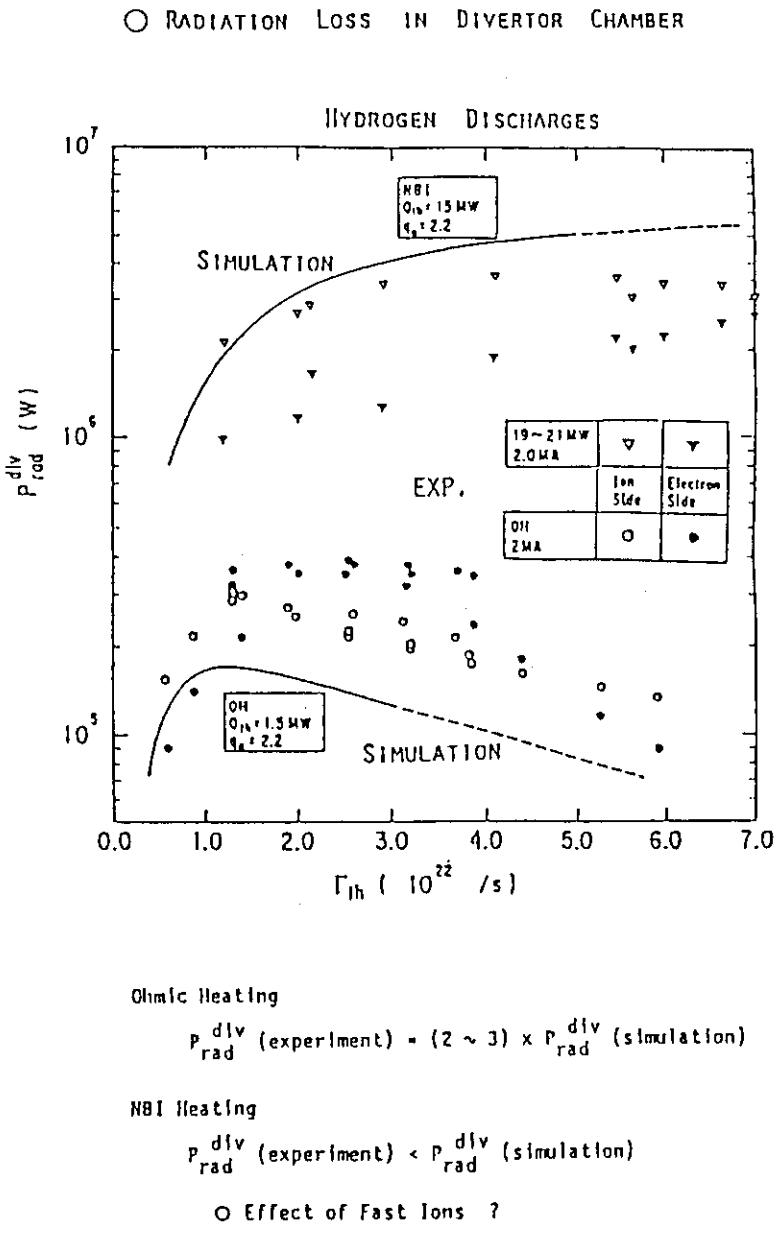

Fig. 1.3 Comparison between the experimental results and simulated results of radiation power in divertor chamber. In ohmically heated plasmas, the radiation power simulated by 2-D fluid model is somehow underestimated by factor of 2-3. On the other hand, the tendency is opposite in NB-heated plasmas.

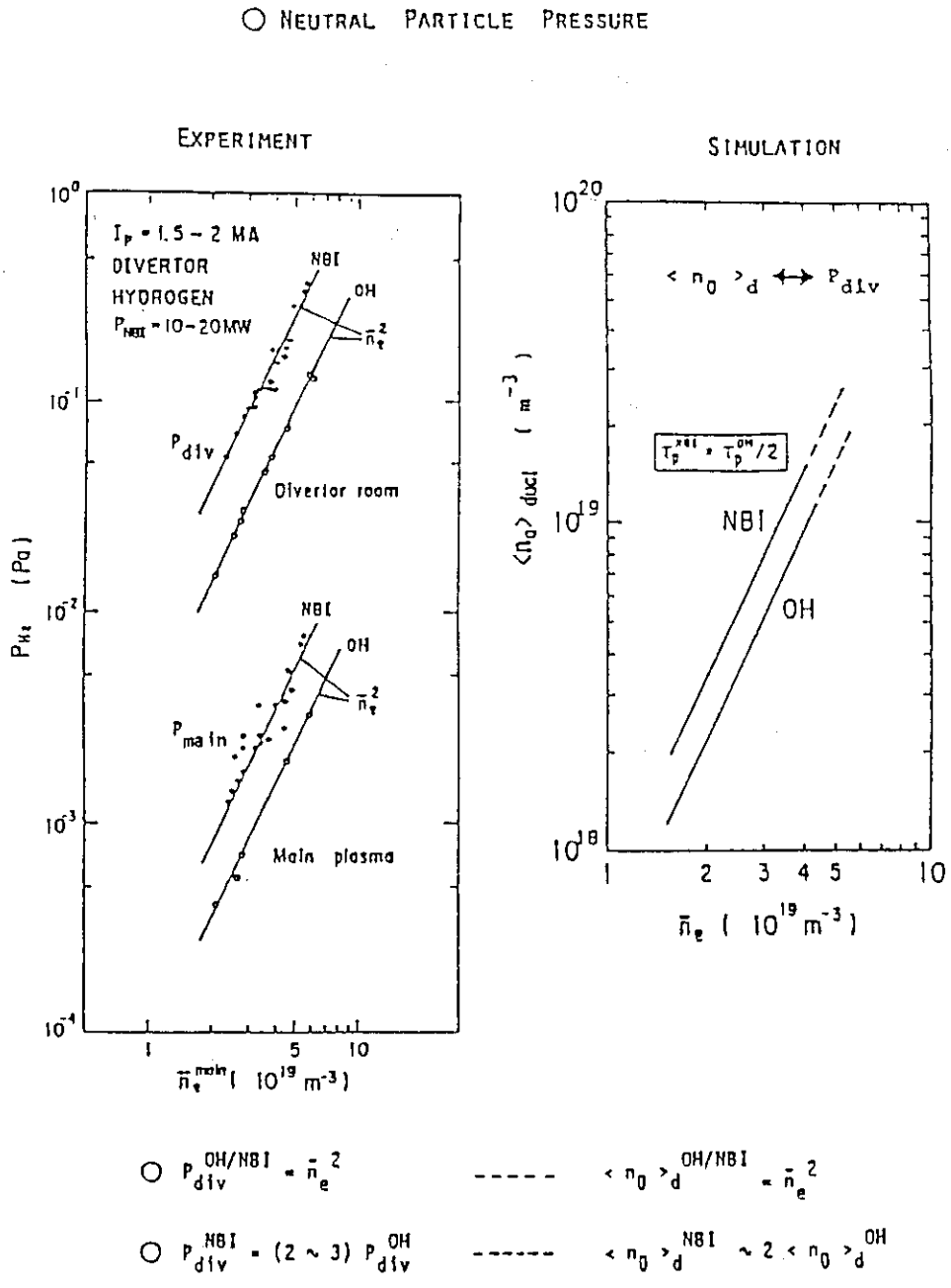

Fig. 1.4 Comparison between experimental results and simulated results for neutral particle pressure in divertor chamber.

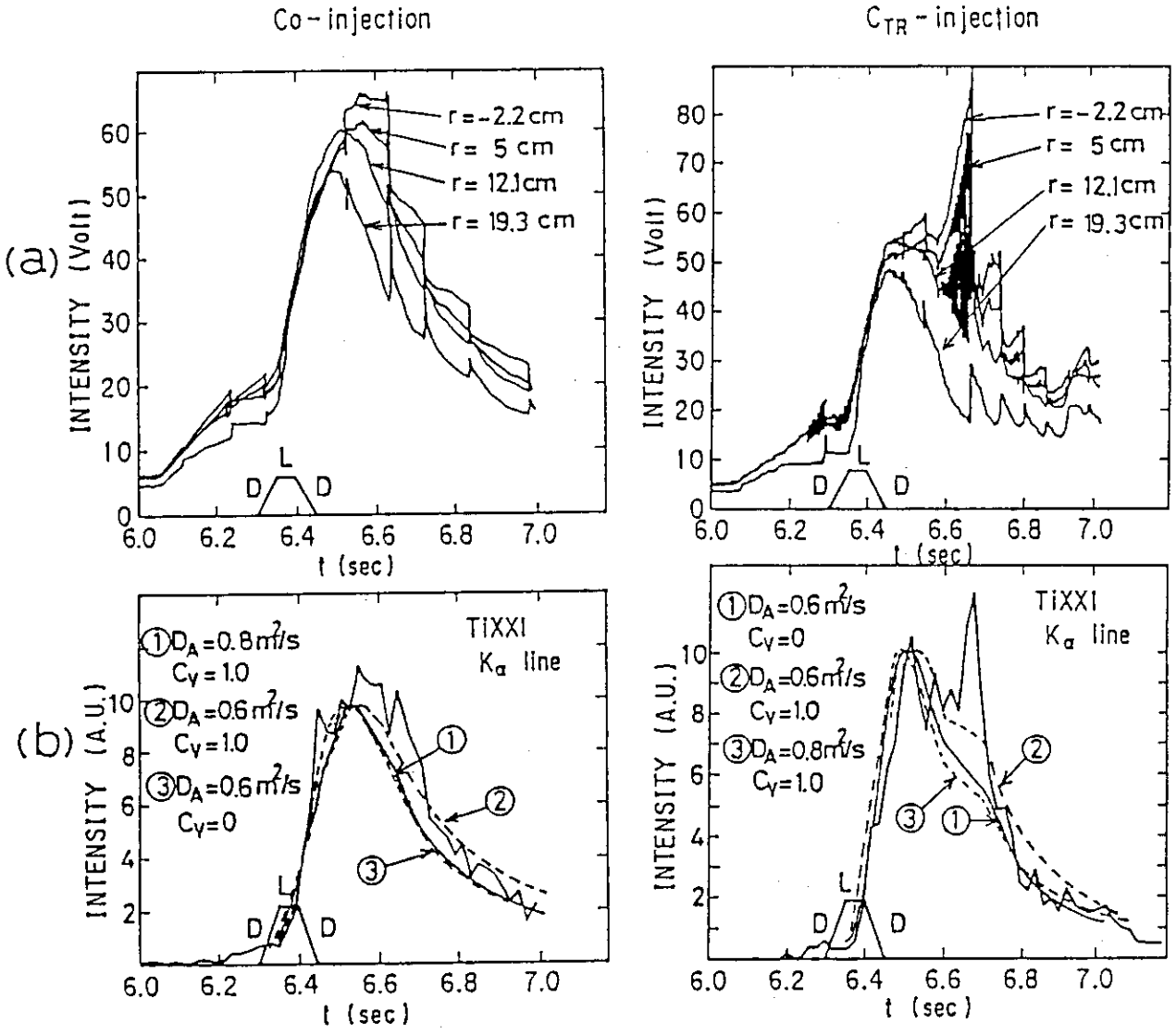

Fig. 1.5 The comparison of time evolution of (a) soft X-ray (b) TiXXI resonance line with co- and counter-NB injection. Titanium was intentionally injected by switching the configuration from divertor to limiter one, and back to divertor as shown in the figure. The fitting results of diffusion coefficient simulated by 1-D transport code are D_A=0.6 m²/s and D_A=0.8 m²/s with C_r=1.0 for counter- and co- NB injected plasma.

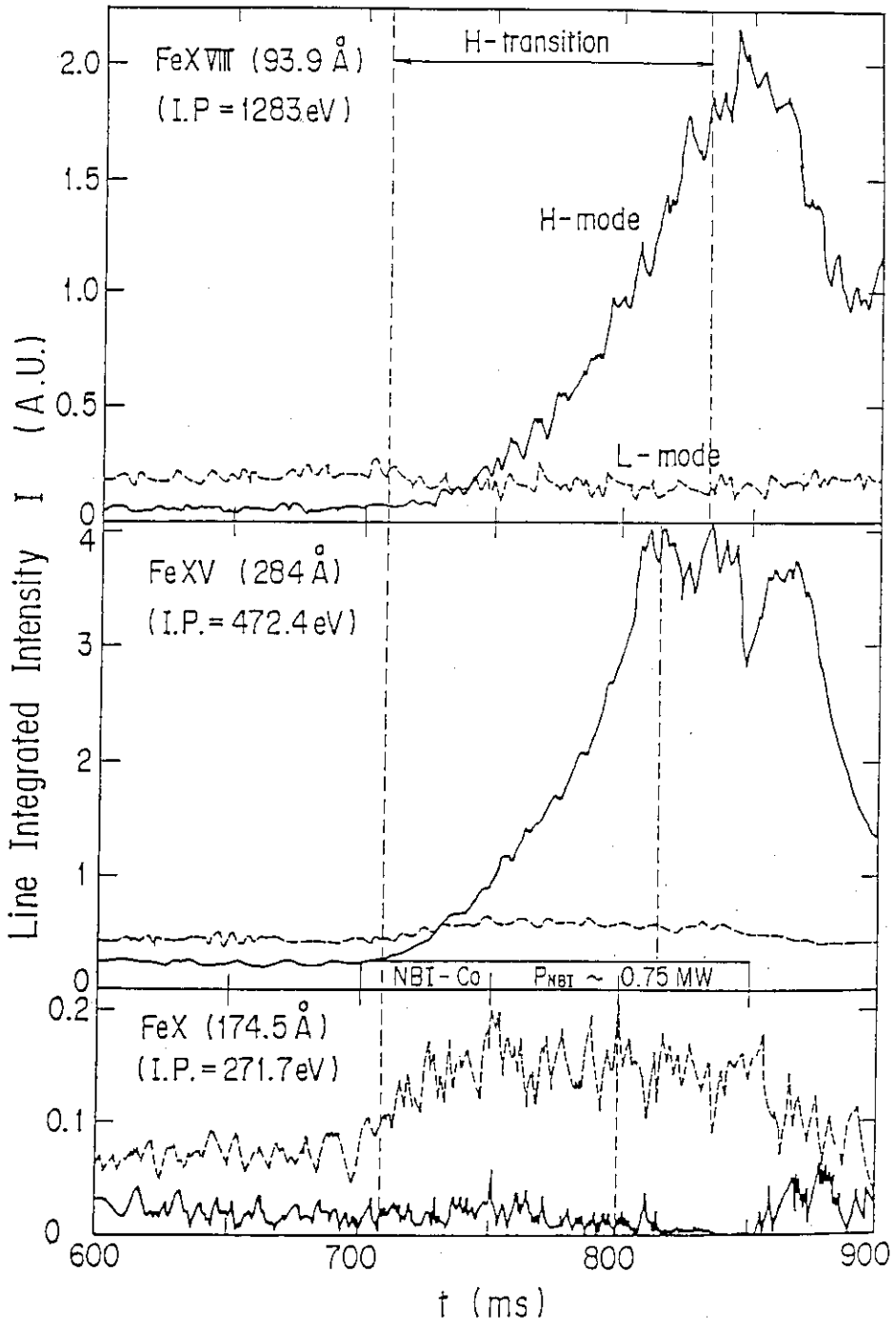

Fig. 1.6 Time evolution of iron line integrated intensity (FeX; λ=17.4nm, FeIV; λ=28.4 nm, FeXVIII; λ=9.4mm) in H-(solid line) and L-mode (dash line) discharges. During H-mode phase, the emission from lower ionized ion are depressed like Hα signals, but the emissions from the higher ionized ion are increased exponentially. The increment of these ion density is not due to the increments of the impurity influx but mainly due to the improved particle confinement during H-mode phase.

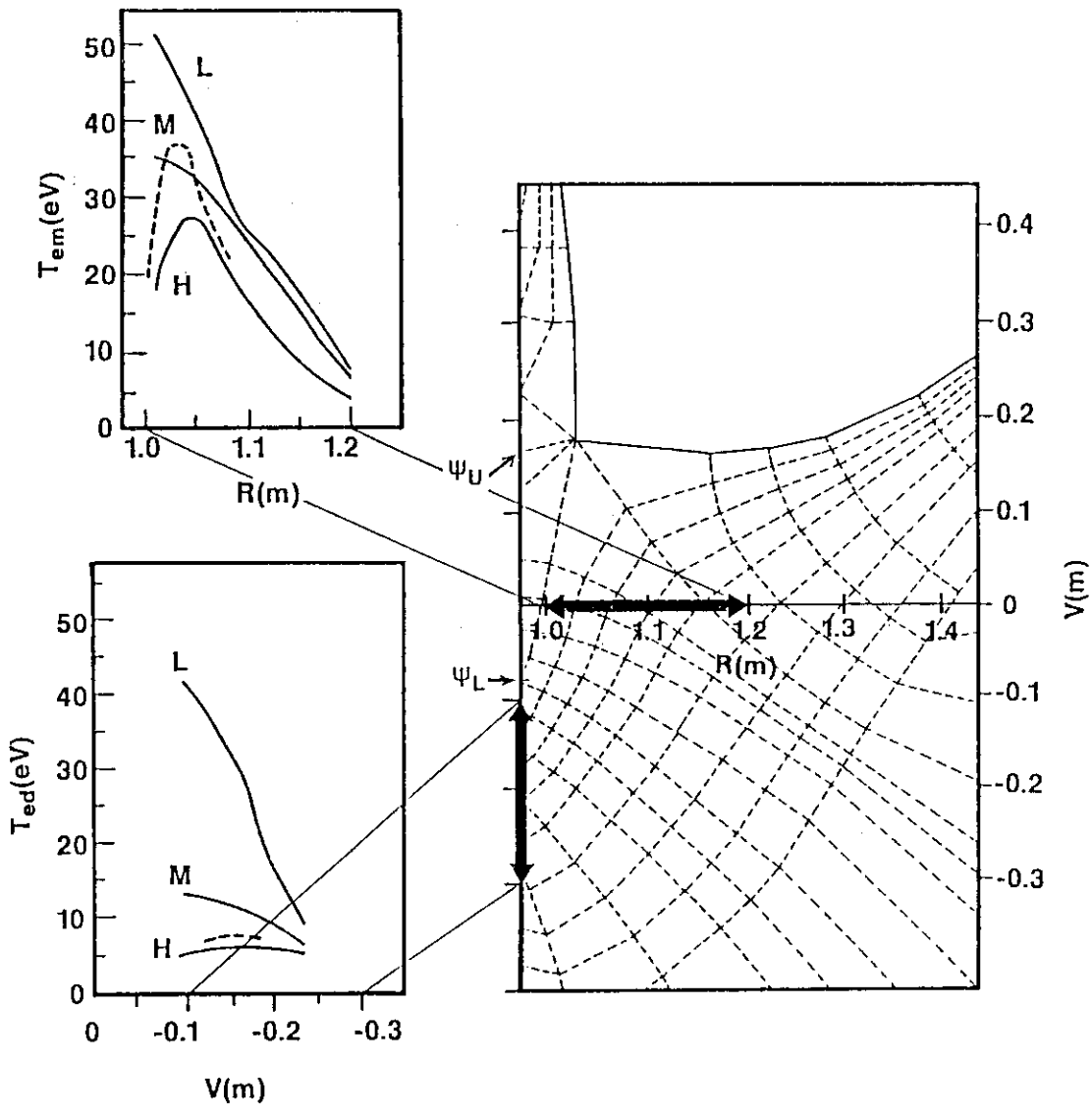

Fig. 1.7 Horizontal profile of the electron temperature T_{em} across the lower divertor channel (device mid-plane: V=0m) and corresponding vertical profiles of T_{ed} on the divertor plate for each particle flux from the core plasma across the separatrix (H: $\Gamma = 1.2\times10^{22}$ s^{-1}, M: $\Gamma = 0.8\times10^{22}$ s^{-1}, L: $\Gamma=0.4\times10^{22}$ s^{-1}). (----) denotes the experimental data for $\bar{n}_e = 3\times10^{13}$ cm^{-3}. The separatrix flux surfaces at the divertor plate (Ψ_U and Ψ_L) are also shown.

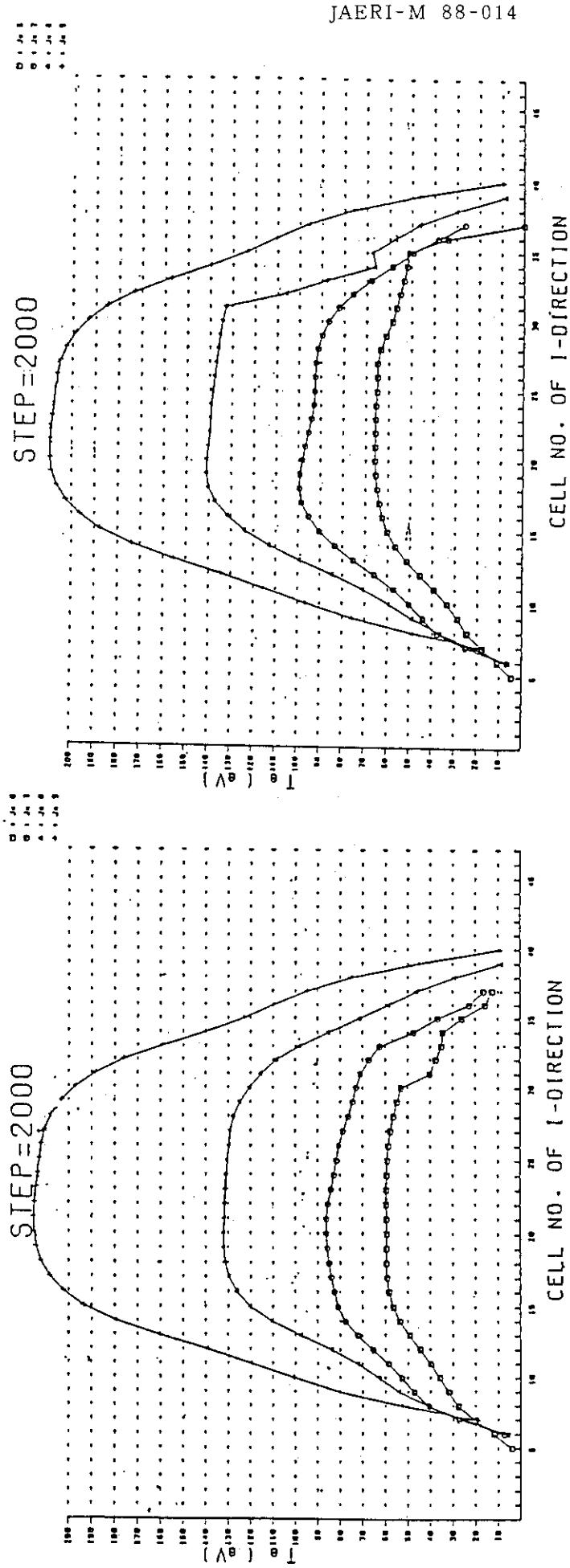

Fig. 1.8 Electron temperature profiles in the poloidal direction for particle flux Γ_p of 1×10^{-22} s^{-1} and 3×10^{-22} s^{-1}. Reasonable low temperatuare plasma in divertor region is evaluated in open diverted FER plasma under appropriate assumptions of impurity and neutral transport based on large tokamak experiments.

2. Operational limits and confinement

It is a critical issue in the design of the INTOR-like reactor to acess the data base on the energy confinement, the beta limit, the density limit etc., and to improve a guide-line by extrapolating the data to the INTOR-like plasmas. In Group B, we presented the experimental data of the H-mode discharges in the JFT-2M tokamak and the results on the analysis of the ideal MHD beta limits during this phase. The scaling laws derived from the data of the JFT-2M, JT-60 and Doublet-III tokamaks were also presented.

2.1 Confinement study

2.1.1 Confinement study of JFT-2M

Experimental data obtained in the JFT-2M tokamak were presented mainly for the H-mode discharges. In JFT-2M, two types of the H-mode discharges are observed; the discharges with the burst of H_α/D_α emission and without the burst. The frequency of the H_α/D_α emission depends on the heating power. In the deuterium discharges where the threshold power for the transition to the H-mode is lower (P_{th} ~250kW) than in the hydrogen discharges (P_{th} ~500kW), the discharges are almost burst-free and the duration of H-mode is limited by the radiation. The threshold power for the transition increases as the safety factor, q, and it depends on the distance between the plasma surface and the limiter at the outside of the torus (Fig.2.1). The threshold power also depends on the location of the null points (Fig.2.2)

The global energy confinement time, τ_E^G, is linearly proportional to the plasma current, I_p, and almost independent of the toroidal magnetic field, B_T; τ_E^G ~$0.15I_p(MA)sec$ (Fig.2.3(a)). The incremental confinement time, τ_{inc} ~$0.115I_p(MA)/\sqrt{B_T(T)}$ (sec) (Fig.2.3(b)). The time, τ_{OH}^P, denotes the maximum energy confinement time in the Ohmic discharges with respect to the density, $\bar{n}_e$. The maximum confinement time, τ_{OH}^P, is linearly proportional to B_T and independent of I_p. The result shows that τ_E^G at minimum q is almost the same as τ_{OH}^P.

The energy confinement time in the H-mode discharge is almost independent of the heating power, P_{tot}, for the ICRF heating up to

P_{tot} ~1.2MW (Fig.2.4(a)) and weakly depends on P_{tot} for the NB heating (Fig.2.4(b)). For higher power, P_{tot}>1.2MW, the discharge tends to the L-mode.

2.1.2 FER scaling (Mirnov-type scaling)

The experimental data of the H-mode discharge during additional heating, obtained in medium-size tokamaks, indicate that the global energy confinement time linearly depends on the plasma current, relatively weak on the elongation and in some devices on the heating power, while it is almost independent of the density and the magnetic field strength. The normalized energy confinement time, $\tau_E/(I_p\sqrt{\kappa})$, obtained in ASDEX, PDX, Doublet-III and JFT-2M, are summarized as the function of the total heating power in Fig.2.5, where I_P and κ denote the total plasma current and the elongation. The confinement time in the H-mode discharges scatters in a wide range and seems to be continuously connected to the L-mode discharge. For example, in PDX, τ_E is strongly degraded by the heating power. The speculated reasons are; (1)the level of the edge relaxation might increase, (2) the excess gas-fuelling might prevent the transition to the H-mode. In Doublet-III, the normalized confinement time has the tendency that the divertor-discharges show better confinement time that the limiter-discharges, although the former cases overlap the latter ones. The confinement time decreases with the heating power and seems to be saturated in the high power region. Those data are fitted in two ways, $(a+b/P_T)$or cP_T^{-d}, with a=0.044, b=0.059, c=0.097 and d=0.35. Both formulae fit the experimental data within the same accuracy. Assuming that the energy confinement time is saturated in a large heating power, the Mirnov-type scaling law can be derived,

$$\tau_E(s) = 0.155a(m)I_P(MA)\sqrt{\kappa} \quad (1)$$

Here the coefficient , 0.155, is obtained by using the minor radius of Doublet-III. On the other hand, there is no or weak degradation in the

confinement time by the heating power in ASDEX and JFT-2M. The maximum confinement time in the best H-mode discharges reaches the level of that in an Ohmically heated plasma. The Mirnov-type scaling described here is pessimistic one by about factor 3 smaller that ASDEX scaling.

2.1.3 Optimized confinement scaling

In an optimized H-mode discharge, the global energy confinement time, τ_E, is as long as that of the Ohmically heated plasma, as shown in Doublet-III, JFT-2M and D-III-Dtokamaks. Therefore it is important to understand the scaling law of the Ohmic plasmas with optimized discharges (discharges with a maximum confinement time). The scaling law of the Ohmic plasmas,

$$\tau_E^{OH} \propto n_e^{\sim 1} R^{\sim 2} a^{\sim 1} q_{cyl}^{\sim 1} \kappa^{\sim 0.5}, \qquad (2)$$

is valid only for relatively lower density. As the plasma density increases, τ_E^{OH} is saturated and gradually decreases as shown in Fig.2.6 except for the cases of the pellet injection. However, a steady-state plasma is not obtained in a pellet-dominated fuelling. Therefore, in a steady state, it is sufficient to obtain the scaling law without pellet injection. The "optimized" energy confinement time is defined as a saturated value of τ_E^{OH} in a high density plasma as shown in Fig.2.6. The critical density, $n_e^c(m^{-3})$, in Fig.2.6 is given by,

$$n_e^c = 6.7\times 10^{19} q_{cyl}^{-1} B_T R^{-1} \sqrt{A_{D,H}} \qquad (m^{-3}) \quad . \qquad (3)$$

The "optimized" energy confinement time is obtained by using eqs.(2) and (3):

$$\tau_E^{OP} = 0.045 R a B_T \sqrt{\kappa} \sqrt{A_{D,H}} \qquad (s) \quad . \qquad (4)$$

The dependence on κ is suggested by the data for relatively low elongation ($\kappa \leqq 1.6$) and the validity in the extrapolation to high κ ($\kappa \geqq 2$) is not clear. The dependence on size, Ra, is not distinguished from a^2 within

present data base. The scaling,

$$\tau_E^{OP} = 0.12\alpha^2 B_T \sqrt{A_{D,H}} \quad (s) \tag{5}$$

is also possible as more pessimistic one in INTOR-like plasma. In good H-mode discharges, the energy confinement time is almost independent of the heating power and proportional to the plasma current. In JFT-2M, the energy confinement time in the H-mode approaches to the optimized Ohmic confinement time, and $\tau_E^H \sim \tau_E^{OP}$ with $q_{cyl} \sim 2.2$ in deuterium plasmas. The optimized confinement times for both Ohmic and H-mode plasmas are summarized in Fig.2.7

2.2 Ideal MHD beta limit

The results of the analysis on the ideal MHD beta limit were presented. The scaling law of the beta limit was investigated and details in the effect of the pressure and current profiles were presented for the D-shaped plasmas. The access to the second region of stability for the ideal MHD mode was proposed as an innovative idea to enhance the beta limit of the non-indented plasmas.

2.2.1 Beta limit of D-shaped plasma

The alternative iteration of the Grad-Shafranov equation and the ballooning equation with zero growth rate gives the marginal pressure derivative in a whole region of the plasma column, from which the beta limit for the "optimized pressure profile" to the ballooning mode is obtained. The FCT algorithm is used to obtain the optimized pressure profile for a fixed profile of the safety factor, $q(\psi)$. The q-profile is given by a profile of the toroidal current density at a low beta state. The calculated data fit the formula,

$$\beta(\%) = \frac{30\kappa^{1.5}}{Aq_s}\left[1+0.9(\kappa-1)\delta - 0.6\frac{k^{0.75}}{q_s} +14(\kappa-1)(1.85-\kappa)\frac{\delta^{1.5}}{q_s{}^4}\right] . \tag{6}$$

The range of parameters are $1 \leqq q_s \leqq 6$, $2 \leqq A \leqq 6$, $1 \leqq \kappa \leqq 1.8$, $0 \leqq \delta \leqq 0.5$ and $q_0 = 1$. The result shows the enhancement in the beta limit due to the

elongation coupled with the triangularity. The 3rd and the 4th terms of eq.(6) are effective in the lower q_s region (q_s<3). There appears the degradation from the scale in $1/(q_sA)$ for q_s<3 (the 3rd term) and it is improved by δ (the 4th term). The sign of the 4th term changes from positive one to negative one for $\kappa \geqq 1.85$. However it should be noticed that the data used in this analysis are limited within $\kappa \leqq 1.8$. It should be also noticed that the formula (6) may be applicable for the moderate current profile. The flat and hollow current-profiles are excluded. The beta limit can be summarized by using the normalized current, $I_N=I_p(MA)/a(m)B_T(T)$, where the toroidal magnetic field, B_T, is measured at the center of the plasma. The beta limit is roughly proportional to the plasma current, $\beta(\%)=gI_N$. In the low current region (high q_s; $q_s>q_{sc}$, q_{sc} depends on κ), g takes about 4 it becomes smaller as I_N increases (Fig.2.8). The degradation in g can be improved to some extent by increasing δ. There appears the degradation in g with κ for a given q_s. Figure 2.9 shows β and g as the function of κ for q_s=3, A=4 and δ=0.3. The beta limit tends to be saturated as κ and g-value decreases. As κ increases, the q-profile obtained from a monotonously decreasing current-density profile becomes flat near the magnetic axis and the marginal pressure gradient becomes small in the flat-q region. The competition between the flat and steep-q regions causes the saturation in the beta limit.

To obtain the beta limit due to the external kink modes, the pressure gradient is increased by $CdP_\infty/d\psi$, where $dP_\infty/d\psi$ is the marginal pressure gradient to the ballooning mode. In the FCT sequence, the constant, C, is adjusted to be $\Delta\beta$=0.2%, where $\Delta\beta$ is the increment of the volume-averaged (toroidal) beta value. The stability of the sequence of the FCT equilibria is studied by using the ERATO-J code and the beta limit is obtained from the marginal equilibrium with $\gamma^2 \leqq 10^{-5}$, where γ is the growth rate in the ERATO-J code. The characteristic time in γ is $\omega_A^{-1} \sim 1\mu sec$ for the INTOR parameters. The squared growth rate of $\gamma^2=10^{-5}$ gives the marginal mode structure in this analysis. Figures 2.10(a) and (b) show the beta limit as the function of q_s for the case

without and with a conducting wall, respectively. For the case with a conducting wall, the wall is placed at a_w/a=1.5, where a_w is the horizontal minor radius of the wall. The broken lines in Fig.2.10 denote the beta limit due to the ballooning mode. The beta limit due to the n=1 external kink mode is smaller than that due to the ballooning mode for the case without a conducting wall. Two limits coincide each other for $a_w/a \leqq 1.5$. The sequence of the equilibria used in this analysis is optimized for the ballooning mode but not optimized the external kink mode. The optimization for the external kink mode can be carried out in the q-profile (or the parallel current density to the magnetic field line, $J_\parallel=\vec{J}\cdot\vec{B}/B$ rather than the pressure profile. The external kink mode is stabilized by reducing $J_\parallel$ near the plasma surface and increasing it near tha plasma center. This rearrangement in $J_\parallel$ gives a large magnetic shear ($S=(V/q)(dq/dV)$, V: the volume surrounded by a magnetic surface) near the plasma surface, which stabilizes the n=1 external kink mode.

There appears a steep degradation in the beta limit near q_s=integer for $a_w=\infty$. The degradation is usually largest near q_s=3. For a given $J_\parallel$-profile, the shear becomes stronger near the plasma surface and weaker (sometimes negative) near tha magnetic axis with the increase in the elongation and triangularity. The degradation for $q_s<3$ is improved for a large elongation. However the weak shear causes an m=1 mode near the magnetic axis. The beta limit due to the n=1 external kink mode is approximately summarized in the Troyon's formula (Fig.2.11),

$$\beta(\%) = (3.2\pm0.5) I_p(MA)/(a(m)B_T(T)) \quad . \tag{7}$$

The modulation near the integer q_s is included in the coefficient.

2.2.2 Second stability access

In the usual stability analysis, $J_\parallel$ is assumed to be a monotonously decreasing function of a plasma radius. If the very flat or hollow current profile (i.e. very flat q-profile) is included, the stability of the ballooning mode is expected to be improved for high poloidal beta

value. We define the flatness of the q profile by $S_w=(q(\overline{\psi}=0.5)-q_0)/(q_s-q_0)$. For the cases 1 and 2 this parameter takes $S_w=0.23$ and 0.05, respectively. A small S_w corresponds to a broad toroidal current profile in a low beta state. Figures 2.12(a) and 2.12(b) show the increase of beta as the function of the iteration in the equilibrium and the marginal stability calculations of the ballooning modes for the cases 1 and 2, respectively. For the case 1 the beta value saturates at the beta limit, whereas it increases unlimitedly as the iteration for the case 2. The pressure gradient, $dP/d\psi$, at the final stage of the iteration is shown in Fig.2.13(a) and 2.13(b) for the cases 1 and 2, respectively. The broken line denotes the marginal pressure gradient to the ballooning modes. For the case 1, $dP/d\psi$ is almost marginal everywhere in a plasma. However, Fig.2.13(b) indicates that $dP/d\psi$ can be increased unlimitedly or plasma enters the second stability region of the ballooning modes in a low shear region, $S\leqq 0.2$, where $S=2V(dq/dV)/q$ and $V(\overline{\psi})$ is the volume surrounded by a magnetic surface.

The mechanism of the access to the second stability region can be explained as follows. Due to the outward shift of the magnetic axis, the negative local shear, $S_\nu<0$, appears in the region of negative curvature of the magnetic field line, $\kappa_\psi<0$, (bad curvature region) where

$$S_\nu = -\frac{\vec{B}\times\nabla\psi}{|\nabla\psi|^2}\cdot\nabla\times\frac{\vec{B}\times\nabla\psi}{|\nabla\psi|^2} \quad , \tag{8}$$

and

$$\kappa_\psi = \nabla\psi\cdot\frac{\vec{B}}{B}\cdot\nabla\frac{\vec{B}}{B} \quad . \tag{9}$$

When the region of $S_\nu<0$ stays only in the region of $\kappa_\psi<0$, the pressure gradient reaches the marginal one everywhere in a plasma. If the negative local shear region extends across the line of $\kappa_\psi=0$, a plasma locally enters the second stability region on the magnetic surfaces which are included in the region of $S_\nu<0$. The local negative shear is produced more easily in a low shear region than in a high shear region.

For the stability analysis of low-n modes the pressure gradient is obtained by using the ballooning mode equation with zero growth rate.

The pressure gradient is increased by $CdP_\infty/d\psi$, where $dP_\infty/d\psi$ is the marginal pressure gradient to the $n=\infty$ ballooning instability at each step of equilibrium calculation. In the FCT sequence, the constant, C, is adjusted to be $\Delta\beta=0.2\%$, where $\Delta\beta$ is the increment of the volume-averaged beta value. The profile of the safety factor is chosen as $S_w=(q(\psi=0.5)-q_0)/(q_s-q_0)\sim0.05$ and $q_s=3.1$. Above the critical q_0, the direct access to the second stability region is possible. For such an equilibrium the profile of the current parallel to the magnetic filed becomes hollow which deteriorates the stability of the external kink modes. Figure 2.14 shows the beta limit of the external kink modes for $\kappa=1.6$ and $\delta=0.3$. The upper and lower lines denote the cases for $a_w/a = 1.2$ and ∞, where a_w and a are the horizontal radii of a conducting wall and a plasma, respectively. Due to the reduction of the global shear, the beta limit decreases as q_0 for the case of no conducting walls. When the conducting wall is placed close to the plasma surface, $a_w/a=1.2$, $\beta\sim11\%$ possible for $q_0=1.5$. The beta limit due to the $n=1$ external kink modes is close to Troyon's beta limit, $\beta=gI_P/aB_t\sim4\%$ for $g=3$, without a conducting wall. The conducting wall placed at $a_w/a=1.2$ increases the beta limit up to $\beta\geq8\%$ and Troyon's factor g becomes $g=6\sim8$. For the case of $\kappa<1.6$, the factor g takes almost the same value. Above the beta limit, the dominant mode is $m/n=4/1$ for the case of no conducting wall and the mode is localized near the plasma surface. When the conducting wall is placed at $a_w/a=1.2$, the dominant component become $m/n=1/1$, which has no rational surface.

When the conducting wall is placed close to the plasma surface, low-n internal modes becomes unstable. Figure 2.15 shows the beta limits of the internal modes as the function of the toroidal mode number. The minimum beta limit is for $n=3$. As n increases the contribution of the driving term changes from the current-driven (kink) term to the pressure-driven (ballooning) one.

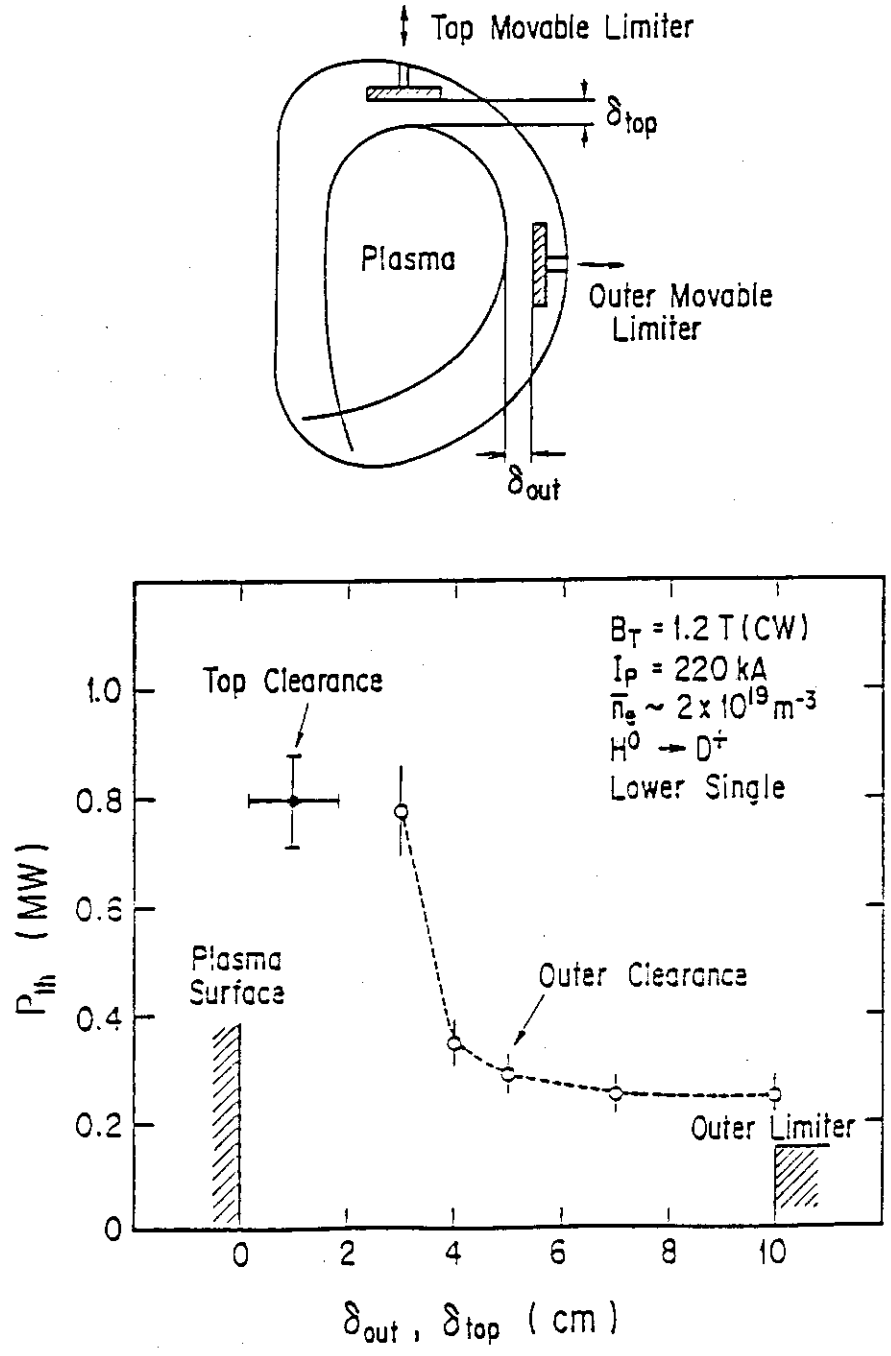

Fig. 2.1 P_{th} vs. clearance(δ). The closed circle denotes P_{th} for the top clearance.

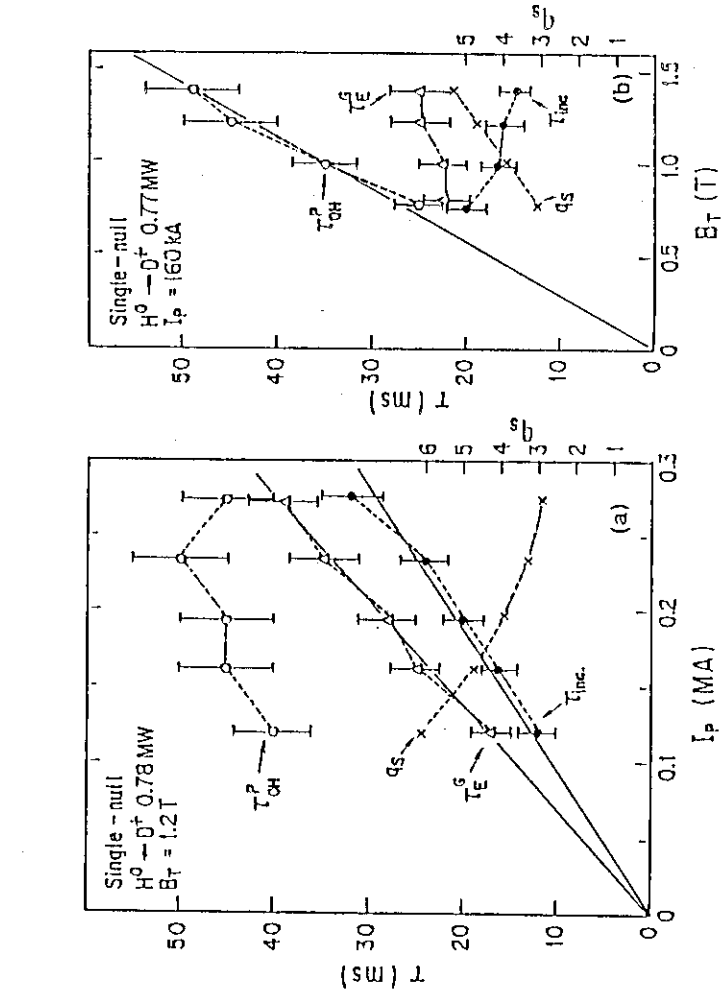

Fig. 2.3 (a) I_p-dependence of global energy confinement time in the H-mode without H_a/D_a burst.
τ_{OH}^P : peak confinement time of OH-phase.
τ_E^G : global energy confinement time near the W_s peak.
$\tau_E^G \equiv W_s/P_T$.
τ_{inc} : incremental energy confinement time defined by $\tau_{inc} \equiv \Delta W_s/\Delta P_T$.
(b) B_T-dependence of confinement time.

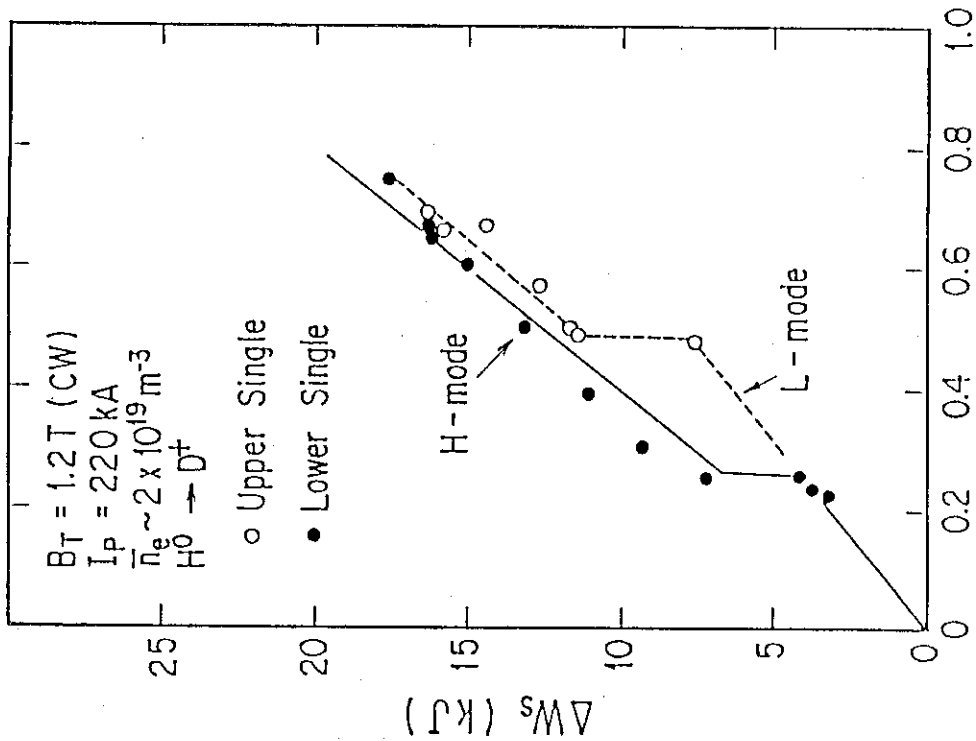

Fig. 2.2 Up-down asymmetry of the threshold power P_{th} for the H-transition. VB toward the null point affects P_{th}. Minimum P_{th} us about 0.2MW.

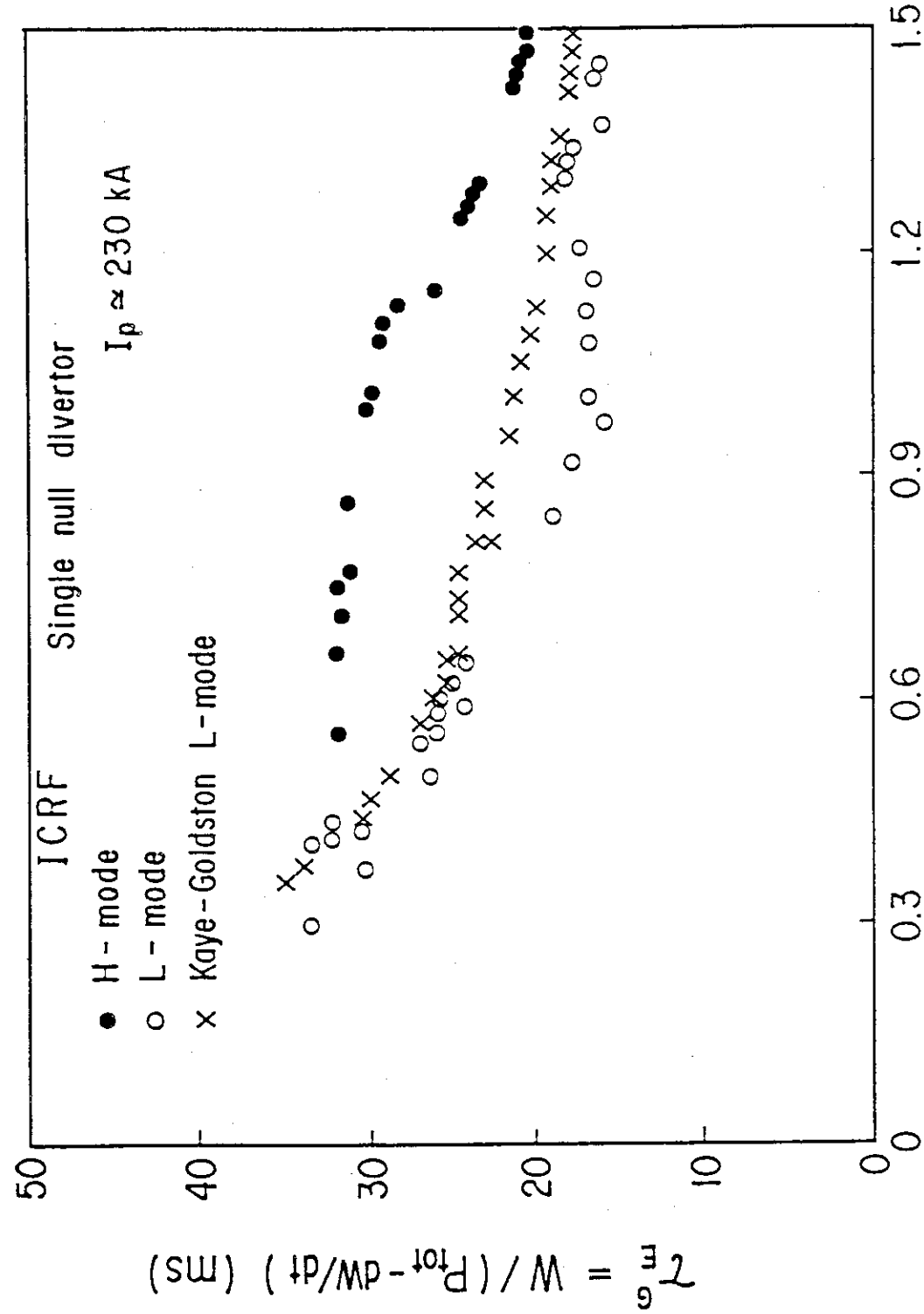

Fig. 2.4(a) Global energy confinement time vs. heating power for ICRF haeting. Symbol, X, denots the confinement time obtained by using the Kaye-Goldston's scaling law.

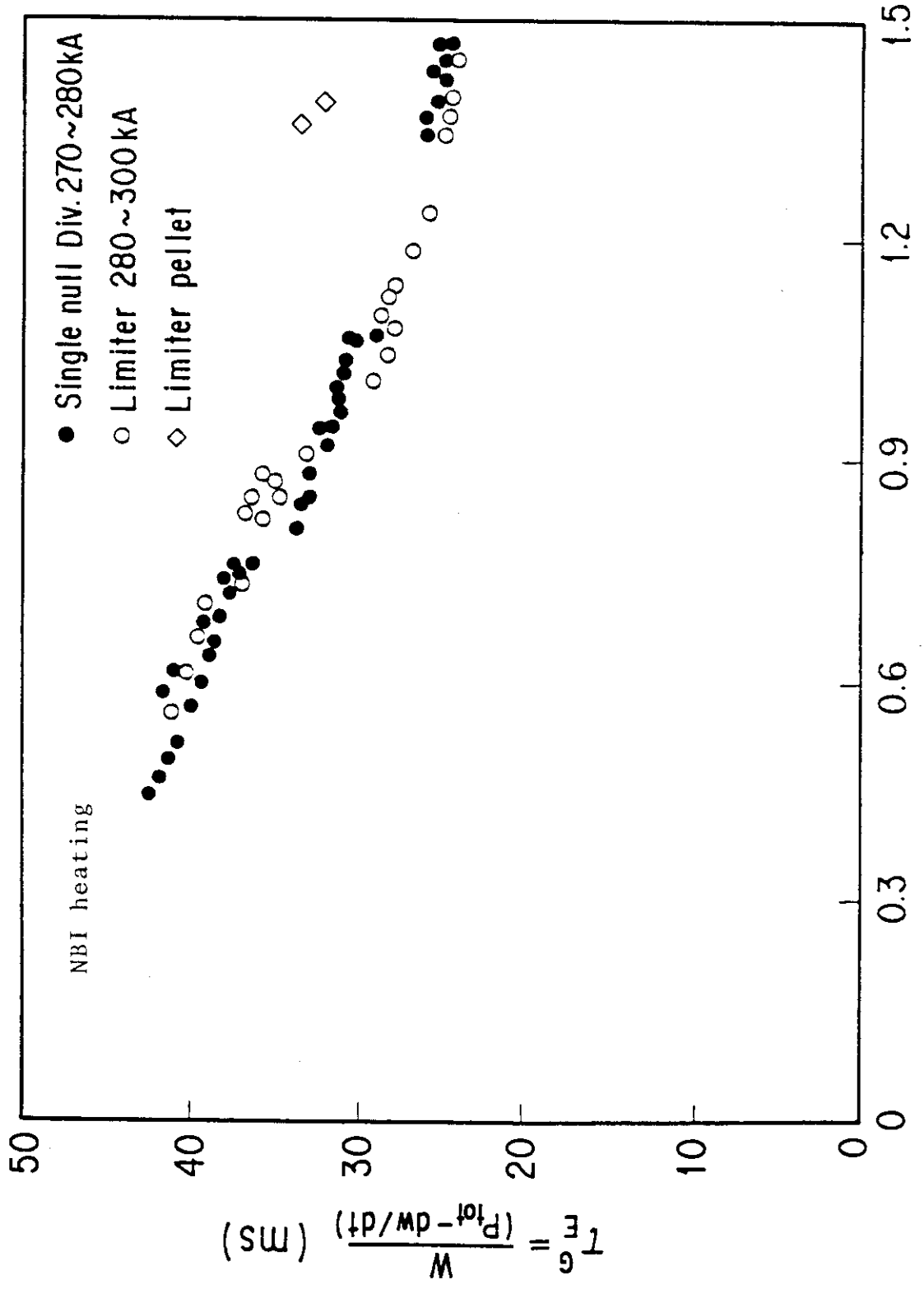

Fig. 2.4(b) Global energy confinement time vs. heating power for NB heating.

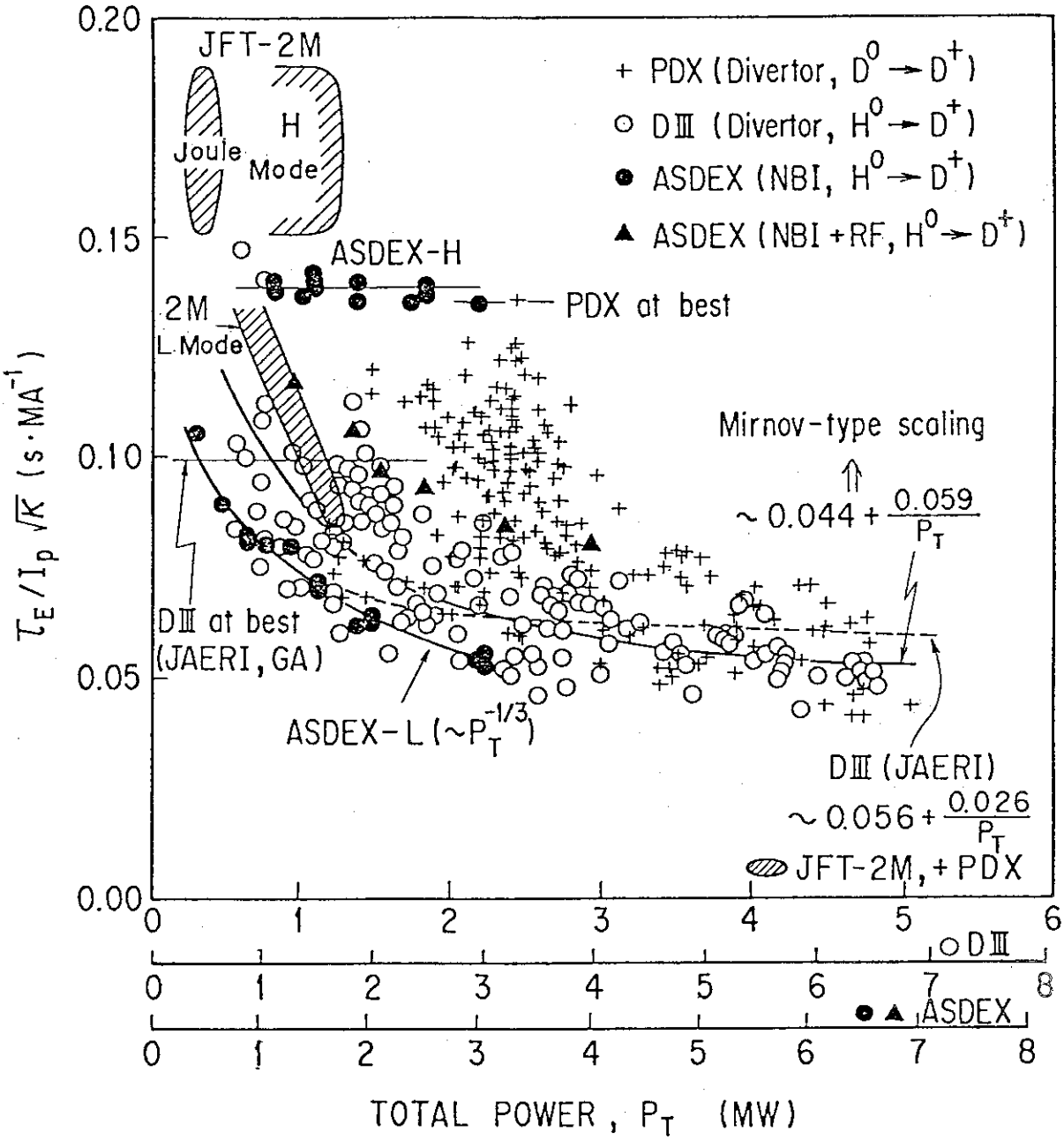

Fig. 2.5 Normalized energy confinement time vs. heating power.

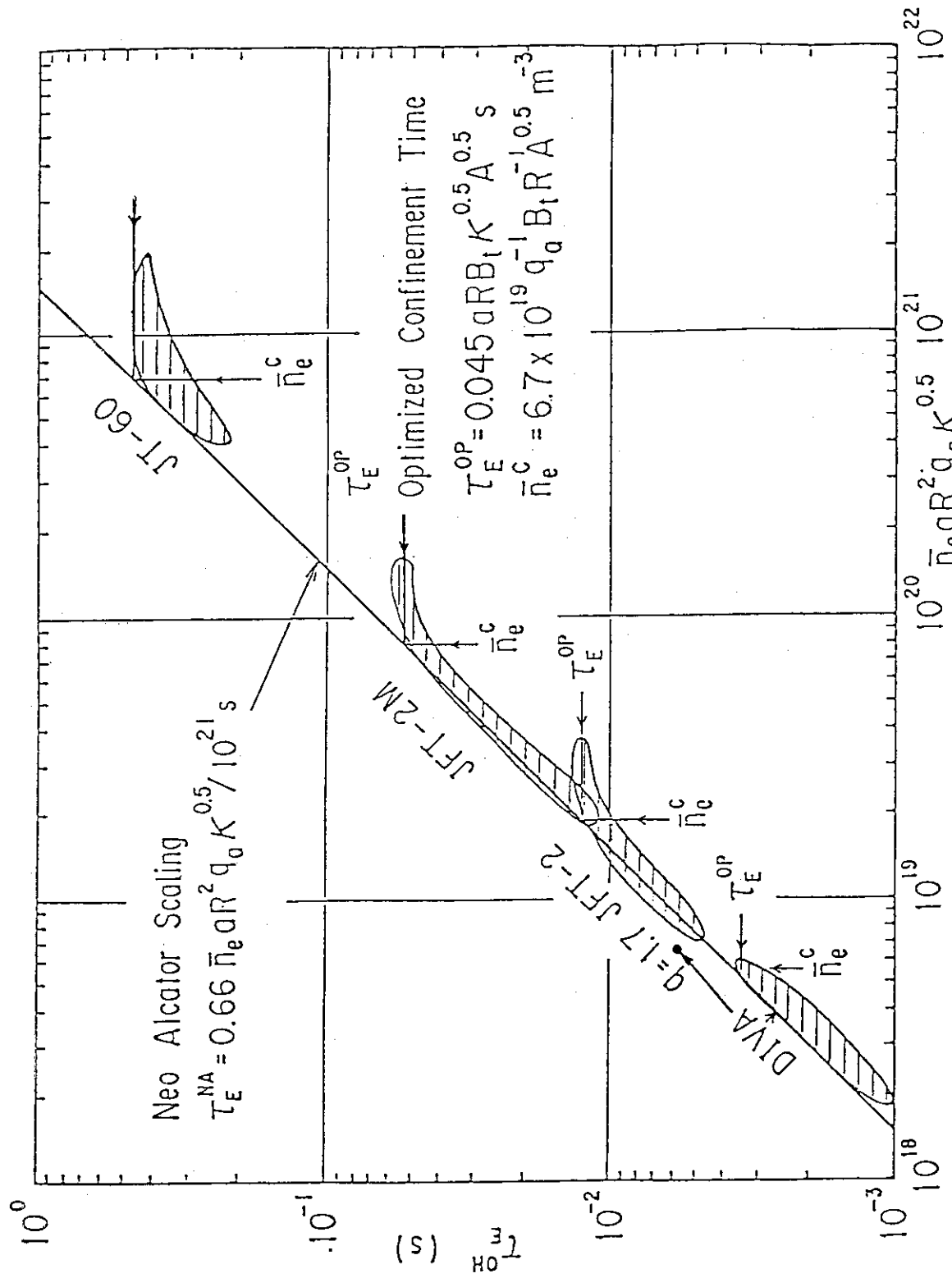

Fig. 2.6 Energy confinement time of ohmic discharges.

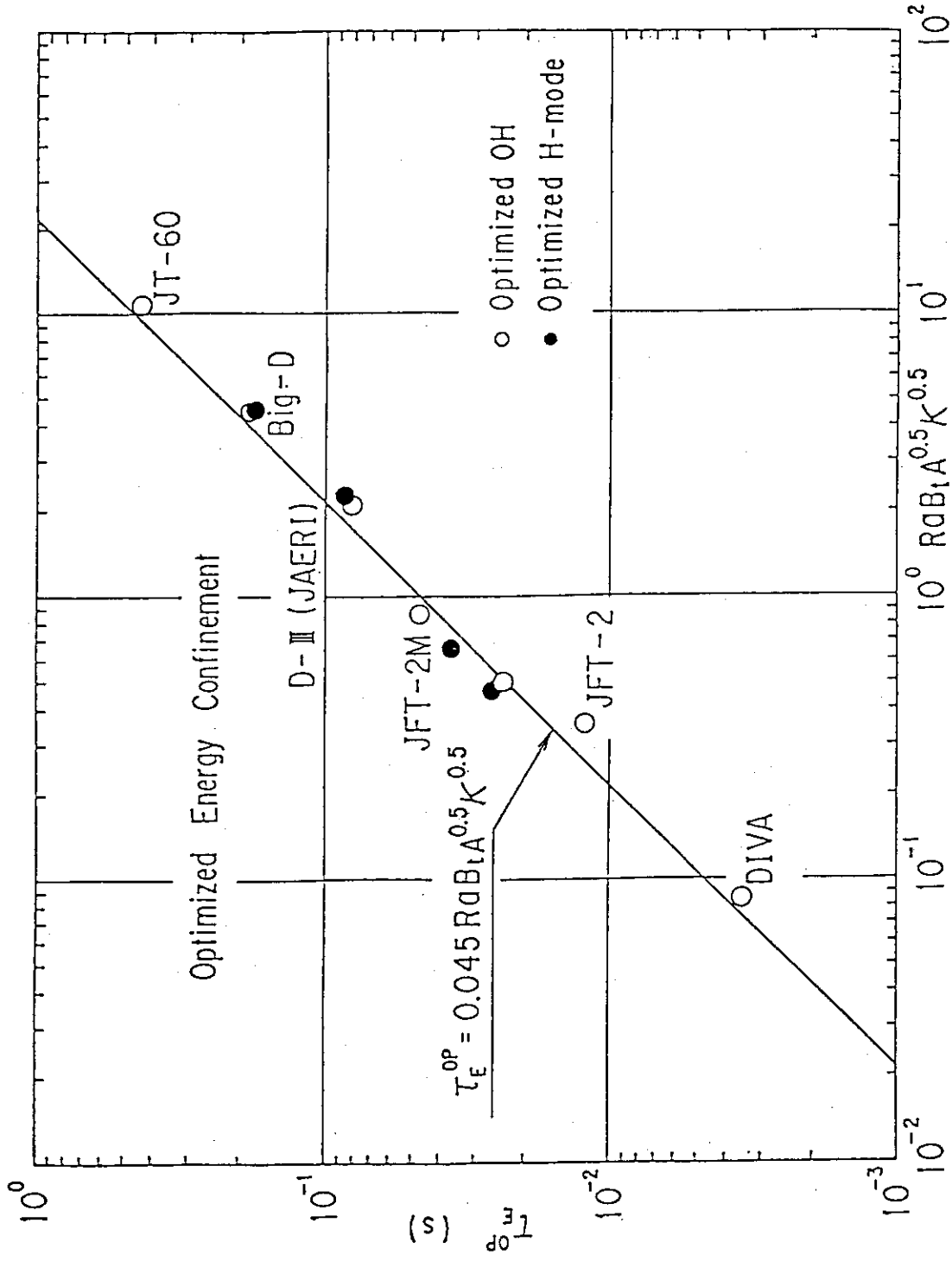

Fig. 2.7 Empirical scaling of optimized confinement time in ohmic and H-mode discharges.

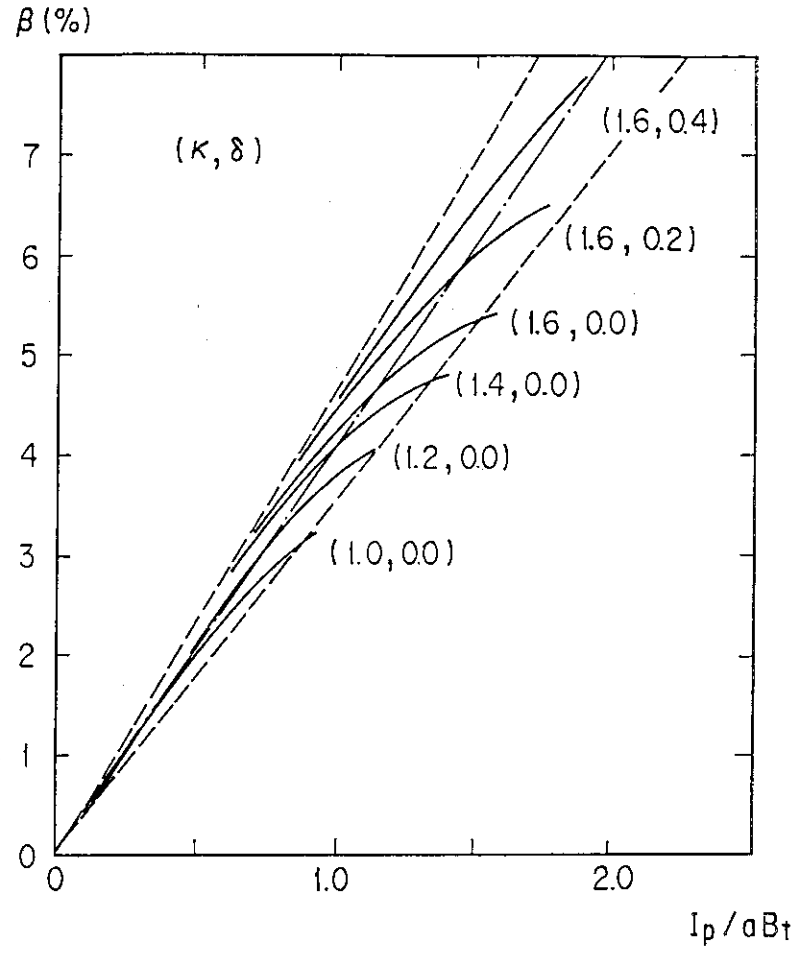

Fig. 2.8 Beta limit due to ballooning mode vs. normalized plasma current

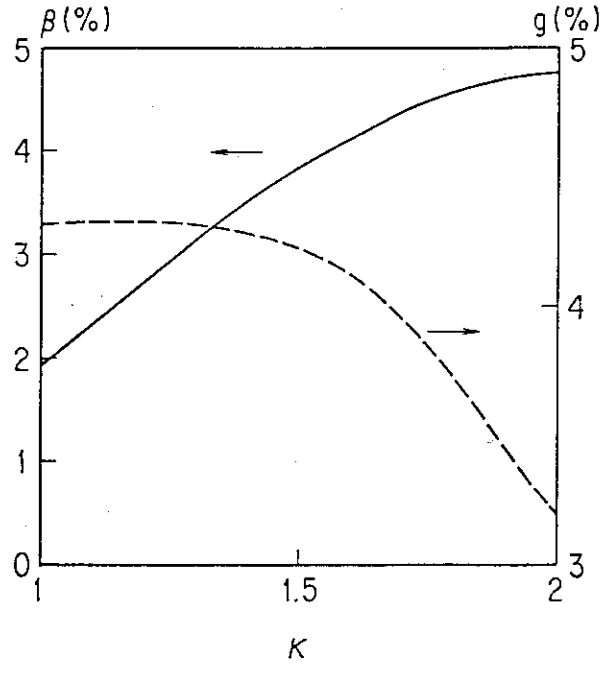

Fig. 2.9 Beta limt and Troyon factor vs. elongation.

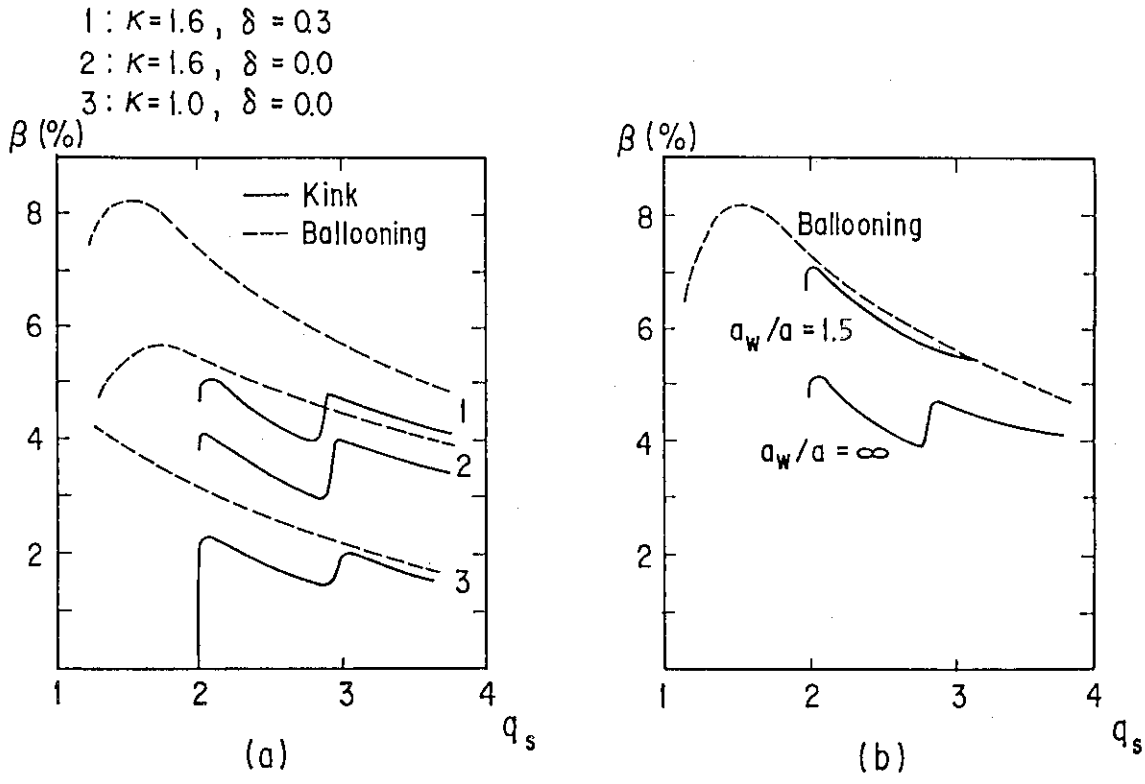

Fig. 2.10 Beta limit due to kink mode(solid lines) vs. q_s for the cases (a) without and (b) with a conducting wall.

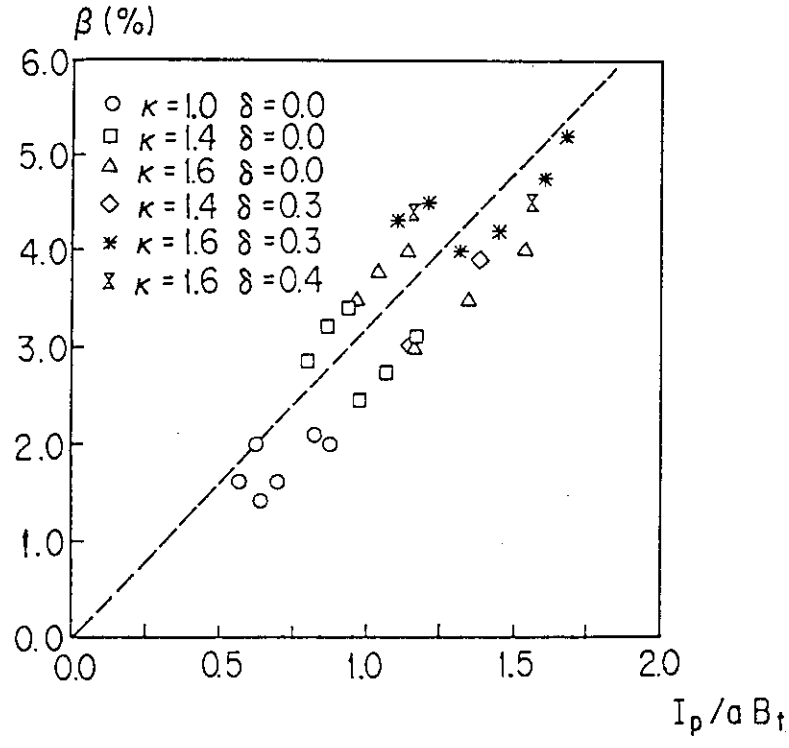

Fig. 2.11 Beta limit due to kink mode vs. normalized plasma current.

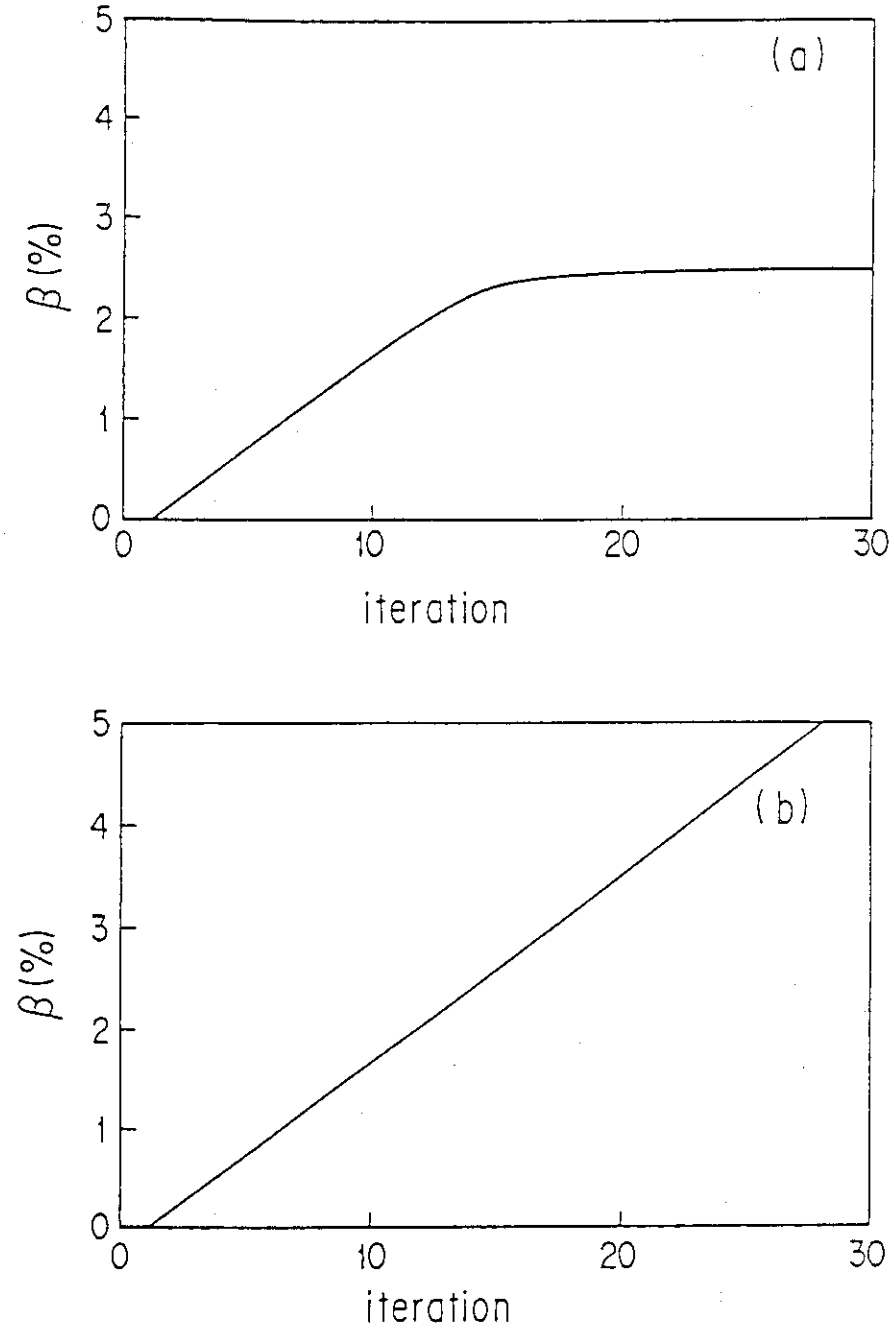

Fig. 2.12 β_t vs. iteration number. Figs.(a) and (b) correspond to the case 1 (S_w=0.23) and the case 2 (S_w=0.05), respectively. For the case 1, the beta value saturates at the beta limit.

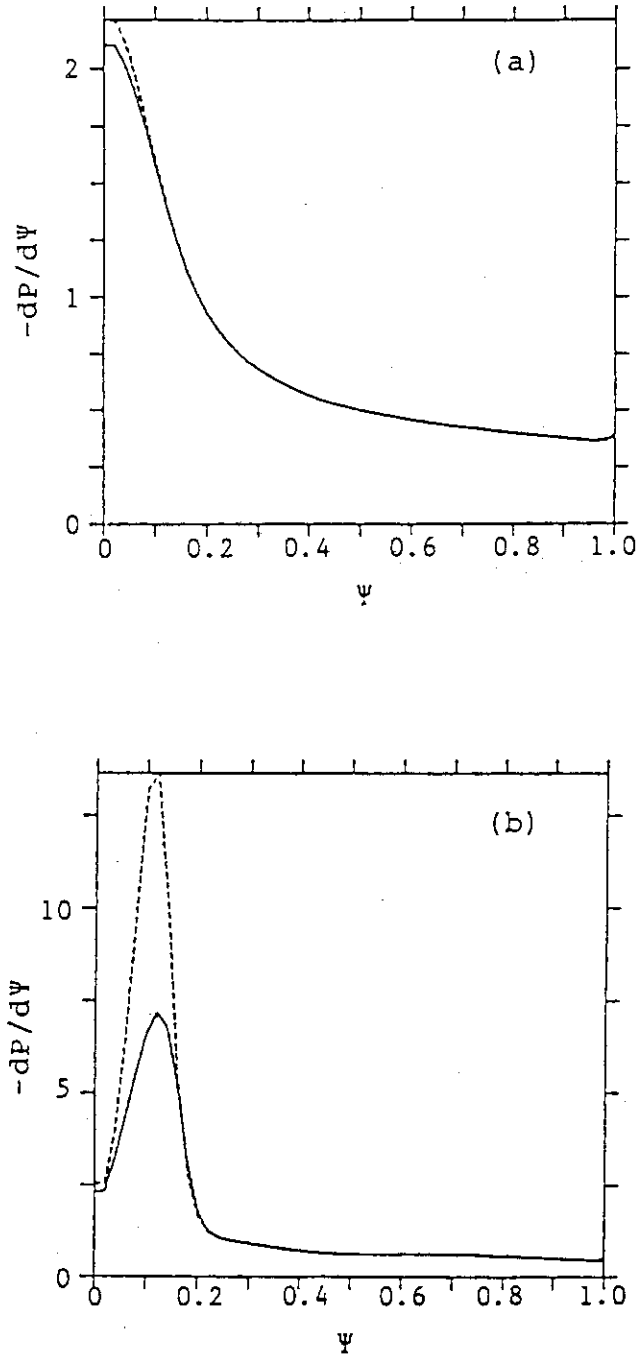

Fig. 2.13 The pressure gradient as the function of $\bar{\psi}$ (a) for case 1 and (b) case 2. The broken line denotes the marginal pressure gradient to the ballooning modes.

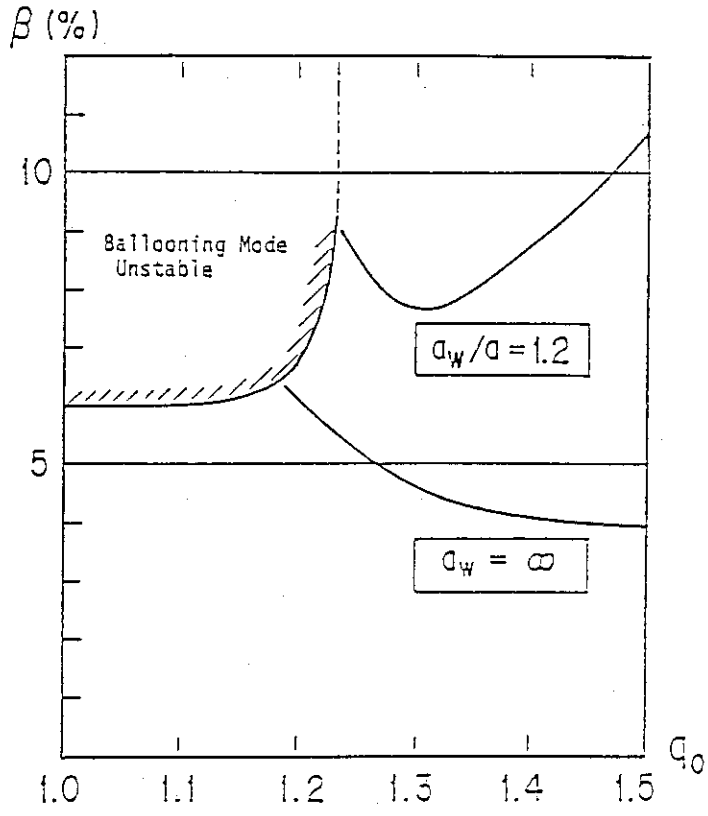

Fig. 2.14 Beta limit of n=1 external kink modes vs. q_0 for κ=1.6, δ=0.3, A=3 and $q_s \sim 3.1$. In the hatched region the ballooning modes are unstable.

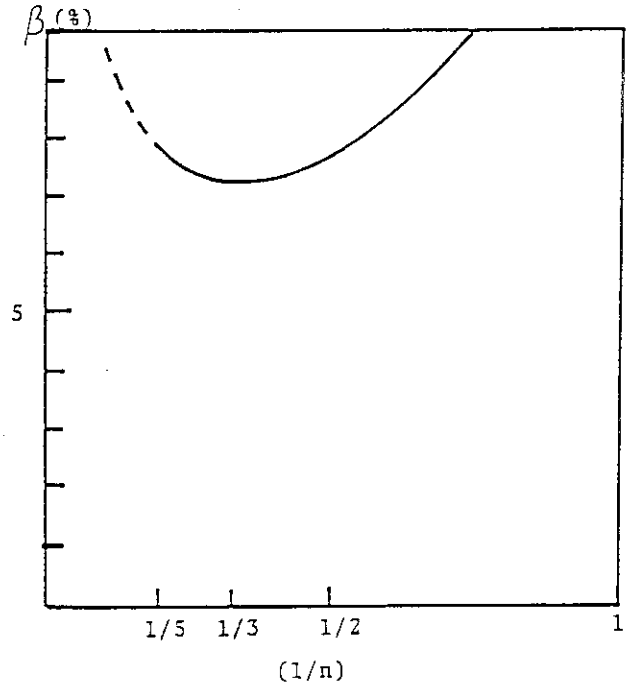

Fig. 2.15 Beta limit of internal modes vs. n for q_0=1.3, q_s=3.1 and S_w=0.05.

3. Current drive and heating

The current drive and heating has been studied as a critical issue through INTOR workshop Pase Two A[1-4]. In the period of Part 2 Workshop of Phase Two A, the heating was mainly studied, although some evaluations were made on the current drive, e.g., a transformer recharging operation scenario by a lower hybrid wave. Based on those studies, the present INTOR concept was confirmed to rely upon a fully inductive operation scenario and ICRF heating as a reference option.

One of major objectives in Part 3 Workshop of Phase Two A is the evaluation of feasibility of innovative ideas, which would improve the tokamak concept. The current drive and heating was selected as a potential candidate and several innovative methods were discussed in the specialists' meeting on tokamak concept innovations[5]. Based upon those backgrounds, the current drive has been considerably emphasized in Part 3, and the specialists' meeting on the non-inductive current drive was held to understand the present status of experimental and theoretical developments[6].

The potential improvements of the tokamak reactor concept, provided by adopting the non-inductive current drive, are discussed. The non-inductive current drive operation basically allows the longer pulse operation, ultimately a steady-state. The following advantages will be expected from the use of the non-inductive current drive. The longer pulse operation will allow the more relevant reactor condition. Physically the long pulse length over the current diffusion time demonstrates the reactor relevant plasma performance, and technically it provides the more favourable condition for engineering testing. The active control of the current profile control may improve plasma performances like β-optimization, control of disruptions and probably confinement enhancement. The inclusion of the non-inductive current drive intrinsically brings the the plasma burn in a sub-ignition state, and it may expand the operation flexibility for burn control and make the machine lifetime longer because of less fatigue. Those consequences from the application of the non-inductive current drive will increase the availability and reliability of the INTOR device. Economically, the non-inductive current drive could be implemented at low supplementary cost, if the common usage of the power for heating and current drive is

made.

The specialists' meeting on the non-inductive current drive concluded that there had been considerable progress in research on the non-inductive current drive in tokamaks[6]. The progress includes all functions for which the non-inductive current drive can be used, i.e., steady-state current drive, current rampup and transformer recharging, control of the current profile and MHD behaviour, as well as current initiation. The LH wave is the most developed technique for the current drive. The NB also shows its capability, although the data base is still limited. Such progress seems sufficient for tentative extrapolation to reactor conditions.

The critical issue group for the current drive and heating in Part 3 Workshop has chosen four main methods for the current drive for INTOR, mainly because of their feasibility in the time scale of INTOR project. They are three RF waves in the frequency ranges of LH(Lower Hybrid), HFFW(High Frequency Fast Wave) and LFFW(Low Frequency Fast Wave), and NB(Neutral Beam). Their various performances like the current drive efficiency, currnt profile controllability and transformer recharging characteristics have been investigated for INTOR.

The goal of the present critical issue study is, using the latest theoretical methods, to compute current driver power for all four options under the same set of circumstances. First, all drivers are required to generate steady state current in a reactor typical of low power operation of INTOR. In this mode, shown in Table 3.1, the density is roughly half the reference INTOR value so the power and neutron load are roughly one quarter of the reference values. The second aim of the study is to learn what degree of current density profile control may be achieved with four options. Flexibility in this aspect of current drive is valuable, as such a tequnique might be employed to improve the plasma operating conditions (e.g., to eliminate sawteeth, reduce disruption frequency, or operate at higher beta). The third goal is compute current drive requirements with a reversed electro motive force at very low density, shown in Table 3.1. This stuation is typical of non-inductive, slow current rampup or of a hybrid burn cycle in which the transformer is periodically recharged.

Table 3.1 Geometry and plasma for evaluating current drive performance

Parameter	Symbol	Units	Value
Major radius	R_0	m	4.9
Aspect ratio	A		4.2
Elongation	κ		1.6
Triangularity	δ		0.5
Toroidal field	B_0	T	5.5
Axis safety factor	q_0		~1.0
Boundary safety factor	q_a		~2.0
Density profile	$n_e(\psi)$		parabolic
Temperature profile	$T_e(\psi)$		parabolic
Current density profile	j		centrally peaked
[Steady state]			
Average density	$\bar{n}_e$	$10^{20}m^{-3}$	0.7
Average temperature	$\bar{T}_e$	keV	20
Electric field	E	V/m	0
Toroidal current	I_0	MA	8.0
[Reversed electric field]			
Average density	$\bar{n}_e$	$10^{20}m^{-3}$	0.04
Average temperature	$\bar{T}_e$	keV	2
Electric field	E	V/m	-0.01
Toroidal current	I	MA	8.0(net)

3.1 Neutral beam current drive [12]

The current drive using a neutral beam is an attractive candidate for a next generation tokamak reactor. Recent experiments on neutral beam current drive in JET and TFTR, where driven currents of about half mega ampere have been successfully observed, indicate that the neutral beam (NB) has large potential in driving a current, although the lower hybrid wave is most successful in producing plasma currents to date. The performance of neutral beam current drive (NBCD) for the next generation tokamak reactor like INTOR has been clarified here, The feasibility of the NBCD using a sub-MeV deuterium beam is mainly discussed, because of significant ambiguity in near-term development of more than 1MeV beam.

The parameter dependence of the current drive efficiency has been derived for the INTOR-like device, such as dependences on temperature, density, effective ionic charge, beam energy, neutral density, temperature and density profiles, and location of beam path. The figure of merit (FOM) for the global current drive efficiency, $\gamma = I_p[MA]\bar{n}_e[10^{20}m^{-3}]R[m]/P_b[MW]$, depends upon temperature and density,

$$\gamma = 0.062\bar{T}_e^{0.58}\bar{n}_e^{-0.092}\{1-\exp(-7.5\bar{n}_e(L/L_0))\},$$

where $10 \leqq \bar{T}_e[keV] \leqq 30$, $0.1 \leqq \bar{n}_e[10^{20}m^{-3}] \leqq 1.0$, $L/L_0 = [(R_0+a)^2-(R_{tang})^2]^{1/2}/4.28$. The factor L/L_0 in the above equation, which is the ratio of beam paths, is added in order to give some generality to this formula for small change in the plasma size. This treatment will give a good approximation of γ for reactor parameters close to the parameters in Table 3.1. Note that this formula is valid for the 500keV deuterium beam only.

The temperature dependence for current drive efficiency I_p/P_b with a constant beta value of thermal pressure kept at 5.9% has been derived, and

$$I_p/P_b = 6.65\times10^{-4}(\bar{T}_e[keV])^{1.58},$$

is consistent with the formula prescribed previously, because $\beta \propto \bar{n}_e\bar{T}_e$ is retained constant in the present calculation.

Z_{eff}-dependence and neoclassical effect have been investigated. When the present neoclassical model is valid, the Z_{eff}-dependence of I_p/P_b and Q value are very weak in the range of $1.5 \leqq Z_{eff} \leqq 3.0$. On the other hand, without the trapped electron correction, the efficiency and Q value are significantly reduced, especially in the range of low Z_{eff}, and the operation with high Z_{eff} will be required to obtain an acceptable drive

efficiency.

The Alfvèn wave might be generated and absorb the fast ion energy, and the beam ions would be rapidly slowed down to the Alfvèn velocity. The effects of Alfvèn wave instability and beam energy on the current drive efficiency are studied. The beam energy corresponding to the Alfvèn velocity, E_a, is about 500keV when $\bar{T}_e$=20keV, $\bar{n}_e=0.93\times10^{20}m^{-3}$, $\bar{n}_i=0.87\times10^{20}m^{-3}$ and Z_{eff}=2.0. The current drive efficiency for a beam of more than 500keV is greatly reduced by the Alfvèn wave instability, while no degradation when $E_b\lesssim$500keV. As the beam of more than 500keV is indispensable to drive currents with a reasonable beam power in future large tokamaks, the Alfvèn wave instability is a critical issue.

The beam driven current can be reduced by charge exchange loss of fast ions during the slowing down process. The efficiency reduction is investigated under the assumption of a neutral atom distribution in a plasma as $n(r)=n_{0edge}10^{2(s-1)}$, where $s=r_\psi/a$. When the ratio of n_{0edge}/n_e exceeds about 10^{-5}, the deterioration of the drive efficiency becomes appreciable. The effect of the charge exchange is limited to the plasma edge, a peaked profile of the objective current profile is unlikely to receive the effect of charge exchange.

The current drive efficiency may depend on the plasma density and temperature profiles;

$T(r)=T_0[1-(r/a)^2]^{\alpha_T}$, $n(r)=n_0[1-(r/a)^2]^{\alpha_n}$.

The profile dependence of the NBCD efficiency is investigated in ranges of $0.5\lesssim\alpha_T\lesssim1.5$ and $0.3\lesssim\alpha_n\lesssim1.2$. The fusion output also depends on the temperature and density profiles. Then the Q values also change. The peaked temperature profiles always reduce both γ and Q. On the other hand, the α_n-dependence of γ is weak, but not simple. One of the reasons for this complicated α_n-dependence is that the power deposition characteristics are very sensitive to the density profile, while the sensitivity to the temperature profile is weak.

The FOM of the global current drive efficiency and the shinethrough fraction are dependent upon the beam path characterized by R_{tang}. The increase in R_{tang} enhances the FOM, while the shinethrough is enhanced. In the case of $R_{tang}>R_0$, the current profile becomes intrinsically hollow.

The current profile, driven by beam injection, depends significantly on the location of the beam line in a plasma. Using these characteristics, current profile tailoring is possible. The beam line is split into 16 beams. Each beam has a cross-section of 0.4m in width and 0.2m in height. Individual beam center lines are parallel to the horizontal plane, but are vertically shifted with Z_h from the tokamak equatorial plane. Each vertically shifted beam drives the current in a toroidal shell. Therefore, driven current tailoring is possible by adjusting each beam power.

The beam current drive analysis code, used in this study, has a routine to automatically control each beam power in order to obtain a required current profile. Driven current plofiles on the equatorial plane for various objective profiles are shown in Fig. 3.1 with the beam power distribution on the vertical plane. The current profile controllability of the NB is very flexible. Various profiles from parabolic to very flat ones have been generated, as well as the hollow profile. The deviation between the driven profile and the objective profile is less than 2 %, except for the central small bumps and the edge region. Since the central bumps are removable with a finer control of the central beams (Z_h<0.5m), they are not essential deficiency. It is also shown that the FOM of the global current drive efficiency, γ, is almost independent of the current profiles.

As the current profile flattens and hollows, the beam powers injected near the plasma edge increases gradually. This increases the shinethrough fraction, as shown in the figure. The inclination of the beam line orientation from the horizontal plane improves the profile controllability, even when the beam height is restricted within a moderate value, e.g. $Z_h \leqq 1.1$m. These angled beams increase the profile control ability, but also reduce somewhat the FOM of the drive efficiency, and the shinethrough is still an essential limitation.

The same beam system is used for the transformer recharging except that outer beams are switched off in order to avoid the large shinethrough. Beam energy is 500 keV and the plasma density range is $0.8<\bar{n}_e[10^{19}m^{-3}]<1.4$. This density is rather high compared with that for RF waves.

The steady state power balance is taken into account for the transformer recharging scenario. The current drive analysis code is coupled with a 0-D power balance code, which is based on a two flow transport model and includes various impurity radiation data. 1% Xe impurity is assumed. The Z_{eff} value depends on the temperature, because the Xe ion charge state changes with changing $\bar{T}_e$. The impurity radiation rate also changes with $\bar{T}_e$.

To sustain I_D+I_{OH}=8MA, the power from 47MW to 60MW is required for $0.8 \leqq \bar{n}_e[10^{19}m^{-3}] \leqq 1.4$. As the current drive power in the burning phase is 74MW, the same beam system used for a burning phase can be applied for transformer recharging. The shinethrough can be reduced by raising the density, while the beam power increases. The operational parameters in the transformer recharge phase are summarized in Table 3.2. The FOM of the current drive efficiency increases with $\bar{n}_e$, but I/P is retained almost constant.

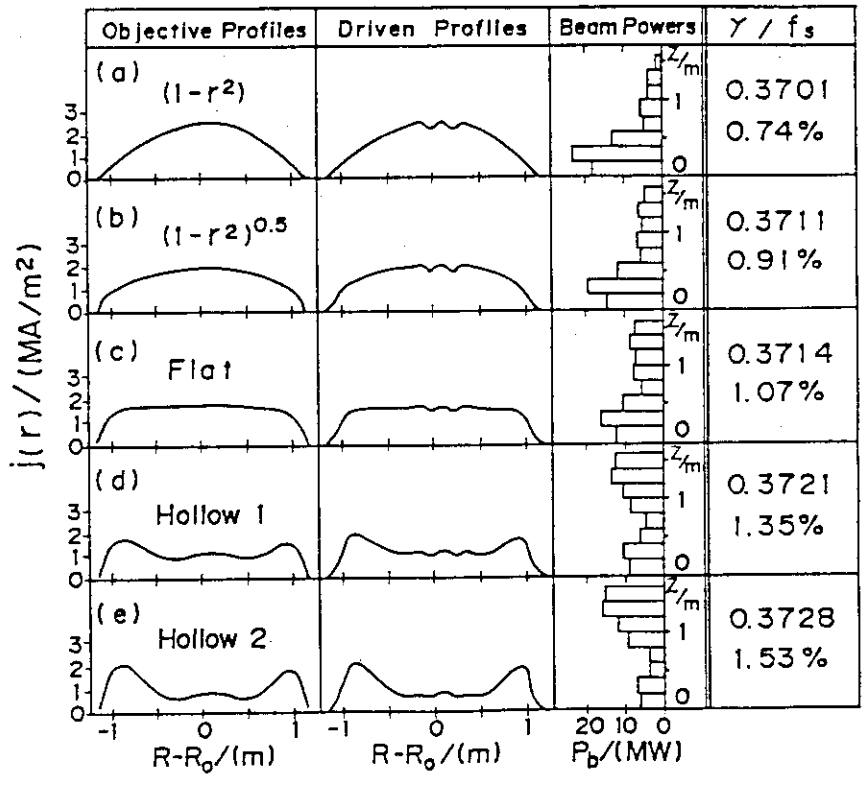

Fig. 3.1 Driven current profiles for various given objective profiles, and required beam power distributions in vertical plane and the figure of merit of the global current drive efficiency, γ, the shinethrough fraction, f_s.

The beam pressure generated by the circulating ions is significant in contrast with RF current drive methods where the current carrying electron pressure is usually small. The beta value due to the fast alpha pressure, β_α, increases with $\bar{n}_e$ and $\bar{T}_e$ as well as the beta value due to the thermal pressure, β_{th}. On the other hand, the beta value due to beam pressure, β_b, has been found to be retained almost constant. The formulae for various contributions to β have been obtained for INTOR size tokamak and shown in Table 3.3, which also includes the current drive efficiency.

Table 3.2 Recharging parameters

$\bar{n}_e$ [10^{19} m^{-3}]	$\bar{T}_e$ [keV]	$\bar{T}_i$ [keV]	P_b [MW]	f_s [%]	γ	I/P [A/W]	I_D [MA]	$-I_{OH}$ [MA]
0.8	8.0	9.5	46.5	33	0.093	0.24	11.0	3.0
1.0	11.2	14.0	53.0	25	0.12	0.24	12.5	4.5
1.2	13.6	16.0	59.5	20	0.13	0.23	13.4	5.4
1.4	12.2	13.0	57.0	15	0.15	0.22	12.4	4.4

Table 3.3 Scaling formulae for efficiency and beta value

Current drive efficiency

$$I/P(A/W)=\gamma/\bar{n}_e R_0=\eta(\bar{T}_e)^{\varepsilon}(\bar{n}_e)^{-\zeta}(1-e^{-\lambda\bar{n}})(4.9/R_0)$$

Beam beta

$$\beta_b[\%]=g_b T_D(B_t)^{-2}(2.2/a^2\kappa)$$

Alpha particle beta (Thermonuclear beta)

$$\beta_{\alpha t}[\%]=g_{\alpha t}\bar{n}_e(\bar{T}_e)^{\sigma}(B_t)^{-2}$$

Alpha particle beta (Beam-plasma direct reaction)

$$\beta_{\alpha b}[\%]=g_{\alpha b}(\bar{T}_e)^{\delta}I_D(B_t)^{-2}(2.2/a^2\kappa)$$

Thermal beta

$$\beta_{th}[\%]=g_t\bar{n}_e\bar{T}_e(B_t)^{-2}$$

where $\bar{T}_e$[keV], $\bar{n}_e$[10^{20} m^{-3}] and

η=0.012 ε=0.58 ζ=1.092 σ=1.986 δ=0.985 λ=7.5(L/4.28)

g_b=4.538 $g_{\alpha t}$=0.118 $g_{\alpha t}$=0.0653 g_t=7.28

3.2 Low frequency fast wave [13]

We have studied analytically and numerically the fast wave current-drive in the high density and high temperature plasma regime which simulates the INTOR plasma. In order to get the optimum launching condition, we have investigated the accessibility of the fast wave and then determined the antenna condition such as the spacing between two adjacent antenna and the total antenna number. The antenna spacing is determined so that the m=1 spectrum peak is removed from the accessibility condition to avoid the counter current genertion. The total antenna number is determined so that the spread of the phase velocity of the excited wave is a level of the electron thermal velocity.

After determining the antenna condition, we have examined the phase dependence of the antenna loading impedance, the power absorption and the current-drive efficiency. For a fixed antenna condition, the optimum antenna phase is found and the global efficiency, $\eta_G \simeq 0.075$ A/W, is obtained in the case of $n_{e0}=10^{20}$ m^{-3} and $T_{e0}=30$ keV within the framework of the 1-dimensional velocity space treatment in the Fokker-Planck equation. This value corresponds to about (0.15~0.18) A/W if we take into account the 2-dimensional effect in the velocity space and reaches the value of (0.48~0.58) in the efficiency definition given by $\gamma=\bar{n}_e[10^{20}\ \mathrm{m}^{-3}]I_p[\mathrm{A}]R[\mathrm{m}]/P_{RF}[\mathrm{W}]$.

Around the optimum antenna phase, the center-peaked current-profile with small corrugation is obtained. The corrugation in the current profile is due to the standing wave formation of the excited wave which comes from the weak coupling between wave and plasma. In this case, the wave absorption takes place in the multi-pass process. We also find that the antenna loading resistance is small around the optimum antenna phase. This result indicates that the larger antenna current is needed to sustain the constant plasma current. With an increase of the antenna phase difference from the optimum one, the total loading resistance increases and the corrugation in the induced current profile disappers. It is also found that the maximum point of the induced current sifts to the plasma surfce. This result shows the possibility of the current profile control by the change of the antenna phase.

We have also studied the performance of the fast wave current-driven

tokamak rector by examining the fusion energy multiplication factor, Q. From the numerical calculation for the temperture and density dependences on the driving efficiency, we find the relation, $P_{RF}=C_{RF}R_0I_p n_{e0}(Z_{eff}+2)/T_{e0}$, and the numerical constant C_{RF}, is determined. The above relation is used to estimate the Q value. We find that the Q value is almost proportional to $\kappa a B_0 T_{e0}^{1.73}(\beta/\beta_c)$ and shows the strong dependence on the temperature under the condition of the constant plasma pressure. This result means that the higher temperature and the lower density plasma is more efficient for a tokamak reactor when the plasma current is sustained by the RF wave. In the present calculation, $Q\simeq 4.3\kappa$ is obtained for T_{e0}=30 keV and $n_{e0}=10^{20}$ m^{-3}.

In order to improve the current-drive efficiency, excitation of the wave with the higher phase velocity is expected. In the present calculation, the maximum phase velocity which can contribute to the current-drive is limited by the wall loss. The ratio, $P_e(k_n)/P_w(k_n)$ depends on the distance between the plasma surface, x=a, and the antenna location, x=d, for the fixed wall radius. Therefore, the locations of antenna and the plasma surface are important parameters. Another method is to increase the exciting frequency. That is, the polarization of the parallel electric field, E_z/E_y, depends on the frequency and becomes larger value with an increase of the frequency. However, the cut-off density becomes higher and the accessibility region for the electron power absorption, i.e. $k_{n,max}<|k_n|<k_{n,min}$, becomes narrower becaue of the dependence of $k_{n,min} \propto \omega$ and $k_{n,max} \propto \omega^{1/3}$. The optimization including the frequency dependence is also needed in the further analysis.

3.3 High frequency fast wave [14]

The fast wave current drive in the parameters of the reactor grade tokamak is estimated. Typical run parameters in this case are; major radius r_0=4.9 m, monor radius a=1.15 m, plasma current I_p=8.0 MA, toroidal field B_T=5.5 T, parameter profile: parabolic, temperature $T_e(0)=T_i(0)$=30 keV, density $\bar{n}_e=0.7\times10^{20}$ m^{-3}, frequency f=0.4 GHz, Z_{eff}=1.5, deuterium gas, $n_{//}(0)$=1.5, $\Delta n_{//}$=1.0.

The frequency dependence of the current drive efficiencies η_e, η_T and the single path absorption rate η_{abs} is investigated, where $\eta_e=I_{RF}/P_e$, $\eta_T=I_{RF}/(P_e+P_i)$ and P_e, P_i, P_{in} are the absorption power to electrons, ions, the input power. At the low frequency regime the ion damping cannot be ignored so that the total drive efficiency η_T is low. When the frequency f is larger than 0.3 GHz, this frequency corresponds to $f/f_{ci}>7$, the ion damping becomes small. Efficiencies η_e and η_T increases with the frequency f while the single path absorption rate $\eta_{abs}=(P_e+P_i)/P_{in}$ becomes small. This is caused by the change of $n_{//}$ with the wave propagation. At higher frequency $n_{//}$ tends to decrease and the wave phase velocity increases so that the collisional dissipation becomes small.

The current drive efficiency η_e and P_e/P_{in} are derived as a function of the central electron temperature $T_e(0)$ with $n_{//}$=1~2 and f=0.4 GHz. The efficiency η_e increases almost linearly with $T_e(0)$. At $T_e(0)$=40 keV, the 60% of the input power is absorbed by electrons and η_e=0.08 A/W can be expected. This value corresponds to the usually normalized current drive efficiency $\gamma=\bar{n}_e[10^{20}\ m^{-3}]R[m]I_{RF}[A]/P_{RF}[W]\sim0.3$. Fast wave may drive the RF current with enough efficiency, and the estimated efficiency is comparable to that of the lower hybrid wave.

The density dependence of the efficiency η_T, $P_{abs}=P_e+P_i$ and $\bar{n}_e I_{RF}/P_{abs}$ are calculated with f=0.4 GHz, $T_e(0)$=30 keV. The efficiency η_T is roughly proportional to $1/\bar{n}_e$ and so $\bar{n}_e I_{RF}/P_{abs}$ is almost constant.

The efficiency η_T and the single path absorption rate η_{abs} are studied as a function of the width of wave phase velocity normalized the mean phase velocity with $n_{//}(0)$=1.5, f=0.4 GHz, $T_e(0)$=30 keV and

$\bar{n}_e$=0.7x10^{20} m^{-3}. The sharp spectrum leads to relatively a good current drive efficiency. The low phase velocity component in the wave spectrum damps and drives the current in the relatively low temperature region where the collisional dissipation is large.

The mean phase velocity dependence of the η_e and η_{ab} is evaluated for the wide spectrum case ($\Delta n_{//}$=1.0) and for the narrow case ($\Delta n_{//}$=0.2). The efficiency η_T increases with the phase velocity while the single absorption rate decreases. When $<v_{ph}>/v_{Te}>3.0$ the electron absorption power is so small that the ion damping cannot be neglible. Therefore the total current drive efficiency is decreases in such region. There is no large difference on η_T and η_{abs} in the low phase velocity while the efficiency η_T of the wide spectrum is smaller than that of the narrow one.

The RF current profiles for various $n_{//}(0)$ are testd where $\Delta n_{//}$=1.0 and the input power is adjusted so that the RF current becomes 8 MA. The RF current profile tends to be broad when the launched spectrum has a large $n_{//}(0)$. In the case of the fast wave current drive the center-peaked current profile can be expected even in the reactor grade high electron temperature like $T_e(0)$=30 keV. The parallel wave electric field of the fast wave is smaller than that of the slow wave such as the lower hybrid wave so that the electron damping rate of fast wave is small. This leads that the fast wave current drive does not tend to form the surface current. It suggests that the fast wave current drive has the capability to control the plasma current profile even in the reactor grade high temperature plasma.

3.4 Lower hybrid slow wave

3.4.1 Lower hybrid current drive for INTOR steady state operation [22]

Potentiality of lower hybrid current drive for INTOR steady state operation in high density and high temperature ($\bar{n}_e \sim 0.75 \times 10^{19}$ m^{-3}, $\bar{T}_e \sim 10$-20 keV) plasmas has been studied. The calculational model consists of three coupled numerical codes:

1) code based on the Brambilla theory for wave spectra and coupling;
2) toroidal ray tracing code for wave propagation;
3) 1-D Fokker-Planck code for power absorption.

The model estimates the absorption power and RF currents along the single ray path for given density and temperature profiles. Wave frequency was chosen as f=4 GHz based on the present data bases for the density limit for LHCD.

Calculated current profiles are generally not centrally peaked, and localized near plasma surface ($r \sim 0.8$-1.1 m) due to the strong Landau damping and the limitation of the wave accessibility.

Effects of wave spectra for the current profile and current drive efficiency have been studied systematically by assuming the wave spectra to be Gaussian profile with the different central value $n_{//0}$ and the half spectrum width $\Delta n_{//}$. For the peaked spectrum with small $n_{//0}$ case ($n_{//0} \sim 1.5$, $\Delta n_{//} \sim 0.5$), the wave penetration was slightly improved, but the RF current profile is still localized near a plasma surface.

We have also investigated the effect of the wave launched angle. Wave penetration can be effectively improved for $\theta_{inj}=90°$ (top launch) with compared to the case $\theta_{inj}=0°$ (horizontal launch) at least for $\bar{T}_e=5$ keV.

3.4.2 Lower hybrid current drive models and their verification with experiments [23]

Two models for the evaluation of lower hybrid current drive efficiency were developed; a 1-D Fokker-Planck numerical model and an extended Fisch-Karney model. These models were compared with experiments

on the ASDEX tokamak. In the comparison with experiments unknown spectrum broadening effect in the plasma is taken into account by adjusting the waveguide spectrum such that the the driven current without DC electric field must agree with the experimental value. Results are summarized as follows:

(1) The steady state (without toroidal DC electric field) current drive efficiencies estimated by both models agreed with the experimental data within a 30 % error.

(2) As for the dependence of efficiency on the DC electric field, the 1-D Fokker-Planck model failed to predict the correct dependence, whereas the dependence predicted by the extended Fisch-Karney model agreed well with the experimental values, and was within the scattering of data as shown in Fig. 3.2.

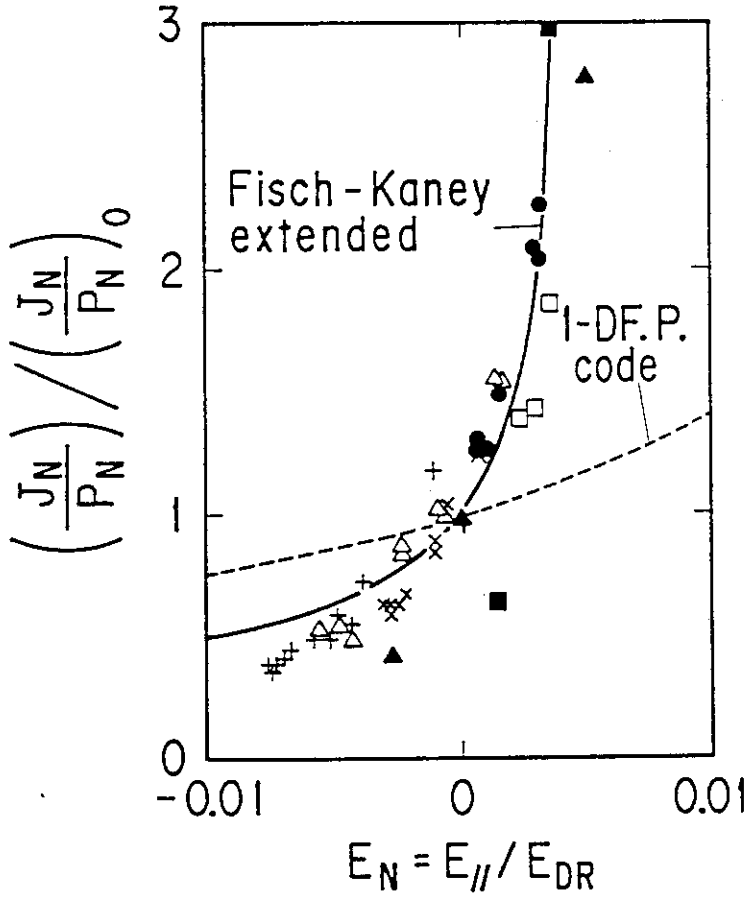

Fig. 3.2 Comparison of experimental and theoretical current drive efficiencies. The normarized efficiencies (J_N/P_N) are plotted as a function of DC electric field E_N.

4. Electromagnetics

The purpose of this section is to provide a summary of Japanese contributions to the Group D (Electromagnetics) during IAEA INTOR Workshop, Phase Two A, Part 3. Parametric studies are carried out for both INTOR like reactor and JAERI FER. An overview of the key results is presented for critical issues and innovations in this section.

4.1 Critical Issues

Poloidal field coils

Benchmark calculation was carried out for static plasma equilibrium. The agreement of the benchmark calculations was very good among the four delegation (EC, Japan, USA, USSR).

The relative merits of single null (SND) and double null (DND) poloidal divertors are discussed from not only physical viewpoints but also engineering ones. Though the DND is somewhat superior to the SND from physical and some engineering aspects, the SND is preferable to the DND from the viewpoint of remote maintenance aspect.

The results of general parametric survey on the next generation tokamak plasma equilibrium are also presented in this item (Poloidal field coils).

Operation scenario analysis

A possible burn time is compared between inductive and quasi steady state operation scenarios for the next generation tokamak reactors as functions of plasma elongation and triangularity. A possible burn time can be largely increased by adopting quasi steady state operation scenario when plasma elongation and triangularity are small as shown in Fig. 4.1. On the other hand, the difference of a possible burn time between two scenario is expected to be small when plasma elongation and triangularity are large.

The requirements for the poloidal field (PF) coil system are compared between two remote maintenance schemes, that is (1) radial access and (2) oblique access. In high elongation plasmas such as $\kappa \gtrsim 1.8$, the requirements for the PF coil system are significantly smaller in the case of oblique access than in the case of radial access. However, the

difference of relative cost is as small as ~3 % at $\kappa = 1.8$. On the other hand, the requirements are almost same between two cases when plasma elongation is medium as $\kappa = 1.6 \sim 1.7$.

Closed loop plasma control

The critical position of the conducting wall is calculated as a function of plasma elongation by using a deformable plasma model. The result is summarized in Fig. 4.2. Since the calculation is rather preliminary one, we need further analysis.

The simulation code is being developed for the feedback control of plasma current, position and shape (PCPS). The scheme of our PCPS control system is shown in Fig. 4.3. We use the plasma model with concentrated constants for practical simulation time. The expression of plasma equilibrium is formulated by using Fourier expansion of the flux function and the plasma boundary, and the usual expansion in the inverse aspect ratio.

In a vertically asymmetric system, the vertical and radial plasma movements are mutually coupled. The asymmetric equilibrium field provides a significant effect on this mutual coupling. The scheme of plasma position control is a little sophisticated in such an asymmetric system. When plasmas receive large radial disturbance such as large MHD activities, plasmas will largely move in the vertical direction as well as radial direction due to the vertical asymmetry as shown in Fig. 4.4, and would interact with the first wall and/or divertor plates, which would lead to disruptions.

AC losses in cryogenic structures (SC coil cans and shear panels) caused by plasma vertical position control are calculated as a function of an active control coil location, that is (1) outside TF coils (outer active coil case) and (2) between TF coils and shield (inner active coil case). Figure 4.5 shows the time behavior of the total AC losses in the half sector of cryogenic structures for one pulse oscillation. The total AC losses in the inner active coil case is approximately 1/10 of those in the outer active coil case.

The effect of ferromagnetic steel on plasma position control is evaluated by using a simple cylinder model. The control characteristics in ferromagnetic structures is nearly same as in usual non-magnetic conductive structures as shown in Fig. 4.6 and ferromagnetic steel is

allowable as firstwall/blanket material in viewpoint of plasma position control since toroidal field will be large enough compared with the saturation induction of ferromagnetic steel.

The review of experimental results on plasma vertical position control and some considerations on electromagnetic plasma diagnostics are also presented in this item (Closed loop plasma control).

Plasma disruptions

The induced loop voltages on PF coils at plasma disruptions are calculated for the INTOR class tokamak reactor as a function of plasma current quench time, τ_d. The toroidal one turn resistance of the vacuum vessel is set to be 0.2 mOhm in these calculations. The induced loop voltages range from ~60 V to ~750 V and the voltage shielding effect is estimated as ~0.2 to ~0.6 as shown in Fig. 4.7 when τ_d is 20 msec. These results are on the safety side since the voltages on PF coils are largely reduced when PF coils are electrically closed.

Analyses of coil quench at plasma disruptions are carried out for the JAERI FER. Although the power supplies have the function to regulate the coil currents, it is not enough to cancel the induced voltage since the maximum voltage of the power supply is at most 10 V/turn in the FER design. So there would be a possibility that the increases in the coil current and the AC losses trigger the quench of the superconductor. One turn toroidal resistance of the FER vacuum vessel is ~30 μOhm. The results show that the criteria of $\dot{B} \lesssim 10$ T/s at PF coils and temperature margin of $\Delta T \gtrsim 2$ K are recommended in the FER design. The FER design satisfies these recommended criteria, so no coil quench phenomena will be expected at plasma disruptions in the FER.

The SiC shunt resistors have been used for JFT-2M vacuum vessel to prevent arcing across insulated gaps and protect the PF coil/PF coil power supply at disruptions. The JFT-2M vacuum vessel is electrically insulated at two positions in the toroidal direction. The SiC shunt resistors are installed at these insulated flanges as shown in Fig. 4.8. Induced currents flow from one side of the flange (left side for example) to another side of the flange through the shunt resistors, bolts and the tapered washers. The SiC shunt resistors worked well and there has been no trace of arcing at the flanges of the JFT-2M vacuum vessel.

4.2 Innovations

High current density and high field for toroidal field coils

For the INTOR TF coils, the generalized graph for selecting the winding pack current density in cable-in-conduit type conductors (CICC) with typical $(NbTi)_3Sn$ superconductor has been produced on the basis of the analyses of quench protection and superconductor stability. The estimations have taken into account the temperature rise of 0.5 degree of internal helium caused by the nuclear heating 1 mW/cc and the decrease in temperature margin due to the critical current degradation from the coil manufacturing process. The INTOR TF conductor can be designed using CICC with 40 A/mm^2 of the winding pack current density at 12 T (one of the guidelines defined in the INTOR specialists' meeting on innovations). However, a conductor with 25 A/mm^2 at 16 T, which corresponds to another guideline by the specialists' meeting, is critical and the minimum winding radius must be larger than 2.2 m (Fig. 4.9).

Use of Nb_3Sn for poloidal field coils

A parametric study for the INTOR OH coil design has been carried out in the range of maximum magnetic field of 8 T to 16 T at temperatures of 3.5 K and 4.5 K, using CICCs with typical $(NbTi)_3Sn$ superconductor. Allowable current densities have been determined based on both superconductor design and stress analysis of the conduit. The allowable stress of the conduit material (SS304LN) has been specified to be 530 MPa, two thirds of the yield strength. According to the results shown in Fig. 4.10, the following design guidelines for the OH coils are proposed: 25 A/mm^2 at 10 T, 4.5 K, or 20 A/mm^2 at 12 T, 4.5 K.

Forced flow subcooled He II superconducting coils

The possibility of forced flow subcooled He II superconducting coils has been discussed from the view point of superconducting materials, conductor design and cooling system, comparing those with forced flow supercritical He I cooling. The critical current density of the NbTiTa conductor at 1.8 K is larger than that of the $(NbTi)_3Sn$ conductor at 4.2 K only at fields less than 12 T. Fig. 4.11 shows the allowable set of operating current density and magnetic field for each cooling method.

The safe operating region for NbTiTa conductor with He II cooling at 1.8 K is lower than that for $(NbTi)_3Sn$ conductor with He I cooling at 4.5 K above 10 T. A He II cooling system has several demerits: high initial and operating costs, complexity and unreliability of the system. The following criteria are proposed as the appropriate cooling schemes:

(1) $B \leq 20$ T : forced flow supercritical He I cooling

(2) 20 T $< B$: forced flow subcooled He II cooling

The overall current density limit for the INTOR TF coil

The limit of the overall current density for the INTOR TF coil design has been estimated by using simplified analyses focused on the stress in the TF coil inner legs. Allotting the overall current density in the TF coil inner leg to the two areas, i.e., the winding pack area and the structural material area, two kinds of figures have been plotted as shown in Figs. 4.12 and 4.13. The following criteria for the TF coil design have been proposed, taking into account the safety margin due to inhomogeneity of coil stress:

(1) $J_{total} < 12$ A/mm^2 at 12 T

(2) $J_{total} < 7.5$ A/mm^2 at 16 T

Allowable stresses for structural materials of the magnet system

The allowable stresses for structural materials in the FER magnet system have been defined based on alloy composition, thermomechanical treatment, loading condition (static, cyclic), stress definition and maximum assumed flaw size. Table 4.1 shows the minimum structural material properties of case and conduit at cryogenic temperature. The criterion for allowable static stress is given by

$$S_m = \mathrm{Min}\ (2\sigma_y/3,\ \sigma_u/2).$$

The loading conditions and allowable stress intensity are classified as shown in Tables 4.2 and 4.3. Walker's equation for fatigue life evaluation is recommended, where the stress intensity factor K is given by $K = 1.1\sigma\sqrt{\pi a}$. The safety factor for fatigue life cycles is recommended as follows: $N \leq N_f/4$. Fig. 4.14 shows the allowable initial flaw size of the TF coil case using Walker's equation when $\sigma_{max} = 400$ MPa.

Non-metallic structural materials

Applications of advanced FRPs to the main structural components such

as bucking cylinders, shear panels and coil cases have been discussed in comparison with traditional stainless steel use with emphasis on the sizing and cost reduction, including further research and development needs. FRPs have some benefits for the reduction of activation levels and eddy current losses. However, they are applicable only for components where large rigidity is not required, because of too low modulus. For fusion reactor application, the following problems must be solved in addition to increase of the Young's modulus:

(1) reduction of Young's modulus and strength due to irradiation
(2) increase of shear strength
(3) accumulation of technical data of CFRP, SFRP, ALFRP and so on.
(4) anisotropic property
(5) connecting method

Table 4.1 Minimum structural material properties.

	Case material	Conduit material[a]
Yield stress (MPa)	1200	1100
Ultimate stress (MPa)	1600	1500
Elongation (%)	10	10
Toughness, K_{IC} (MPa$\sqrt{m}$)	200	200[b]

(a) CSUS-JK1 with both cold work and heat treatment

(b) The plane stress fracture toughness (K_{IC}) for a thin conduit reaches a higher level than K_{IC} = 200 MPa $\sqrt{m}$

Table 4.2 Loading conditions.

(i) TF coil case and conduit.

① In-plane force due to toroidal field

② Out-of-plane force due to poloidal field

③ Quench pressure.

(ii) PF coil conduit

① Radial and vertical force due to poloidal field

② Bending moment due to toroidal field ripple

③ Quench pressure.

Table 4.3 Stress category and allowable limits of stress intensity.

Stress Category	Allowable Limits of Stress Intensities
Primary Membrane (General) Stress Intensity	Sm
Primary Membrane (Local) Stress Intensity	1.5 Sm
Primary Membrane (Local) and Bending Stress Intensity	1.5 Sm
Primary + Secondary Stress Intensity	3 Sm

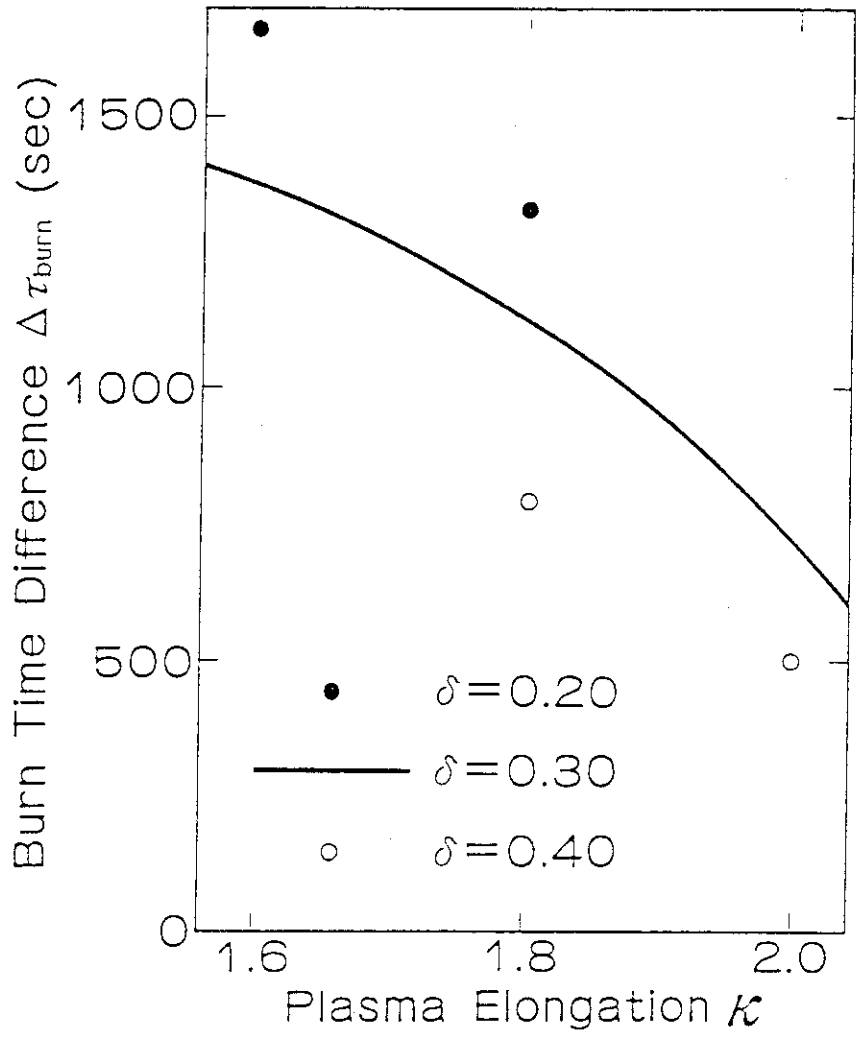

Fig. 4.1 Difference of possible burn time between quasi steady state operation and inductive operation as functions of plasma elongation and triangularity.

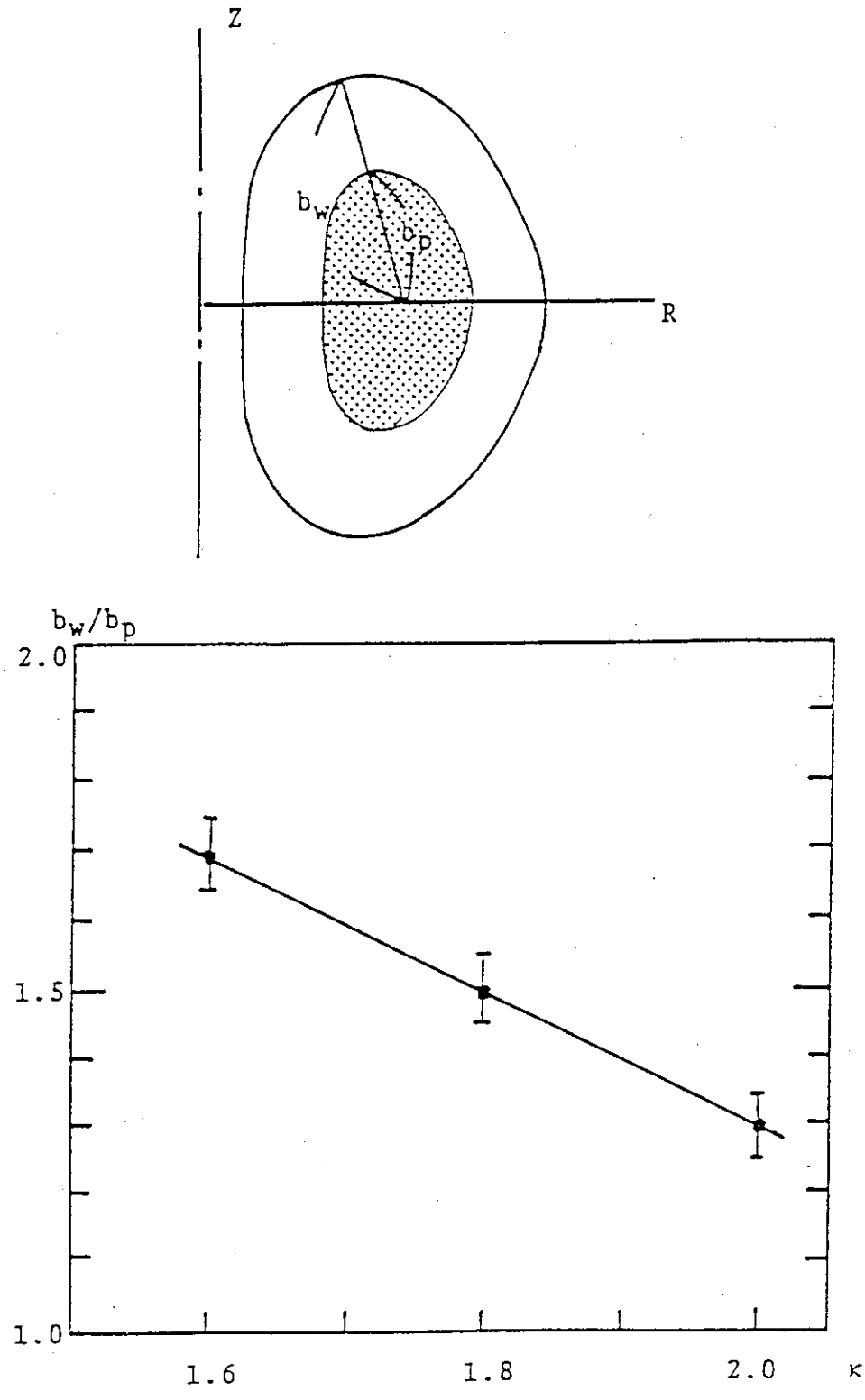

Fig. 4.2 Critical b_w/b_p vs. κ. Effect of δ is small. Plasma surface and conducting wall. The radii, b_w and b_p, denote ones for the top of the dee from the magnetic axis.

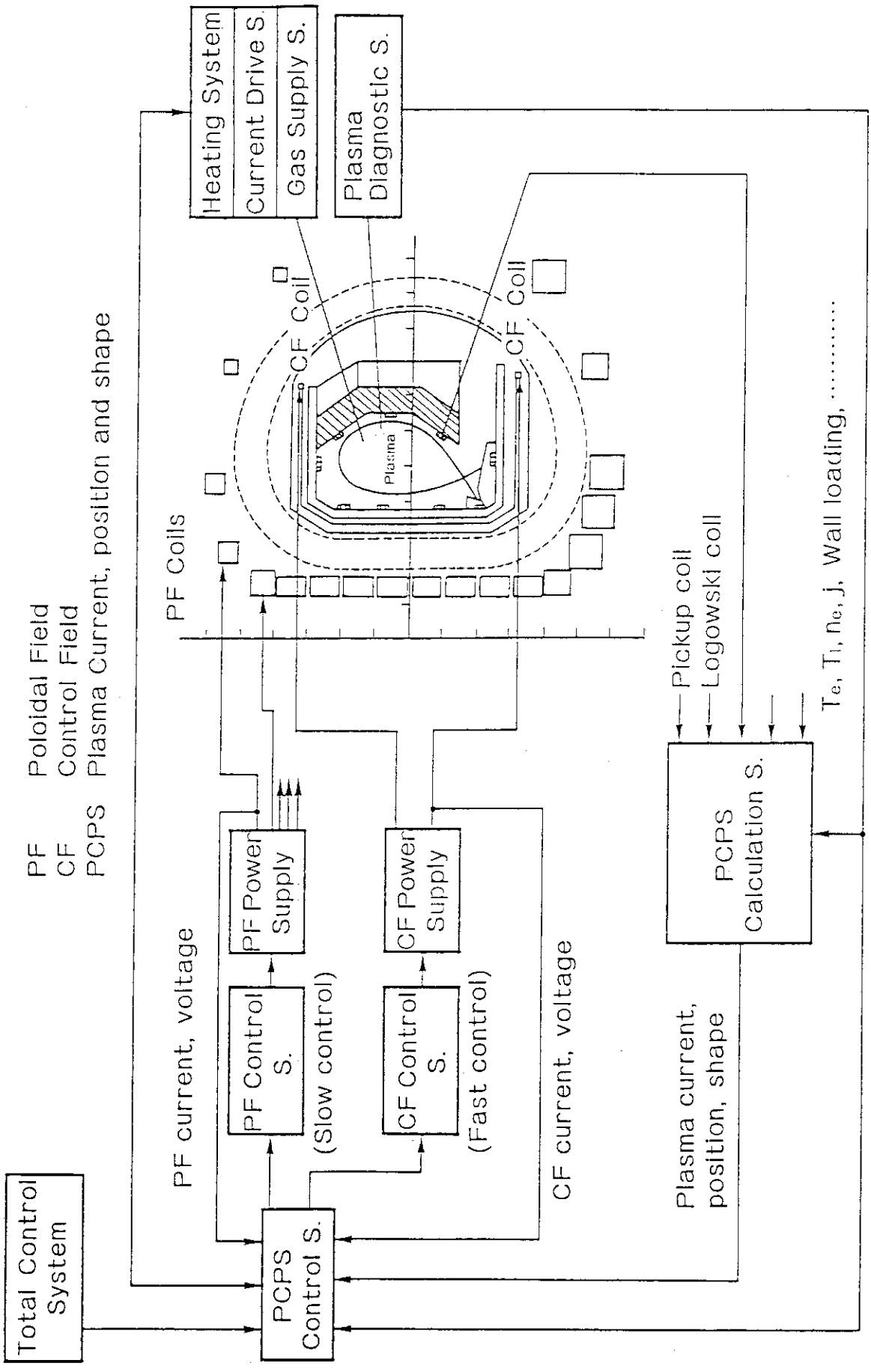

Fig. 4.3 Plasma current, position and shape control system.

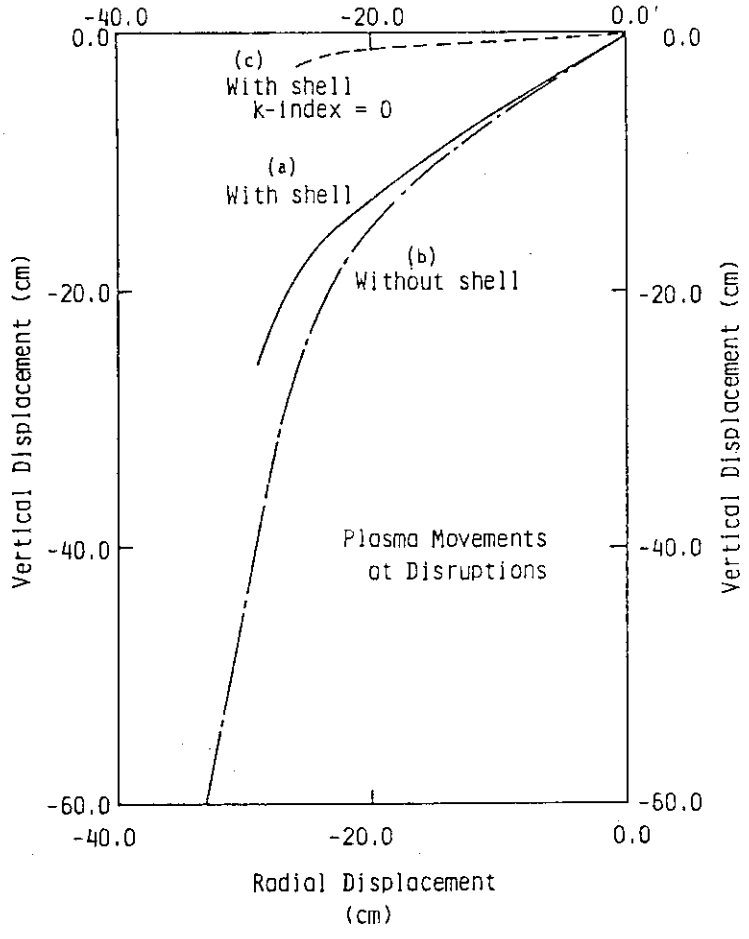

Fig. 4.4 Plasma movements at plasma disruption in 50 msec after disruptions. The β_p is reduced by 40 % within 5 msec.

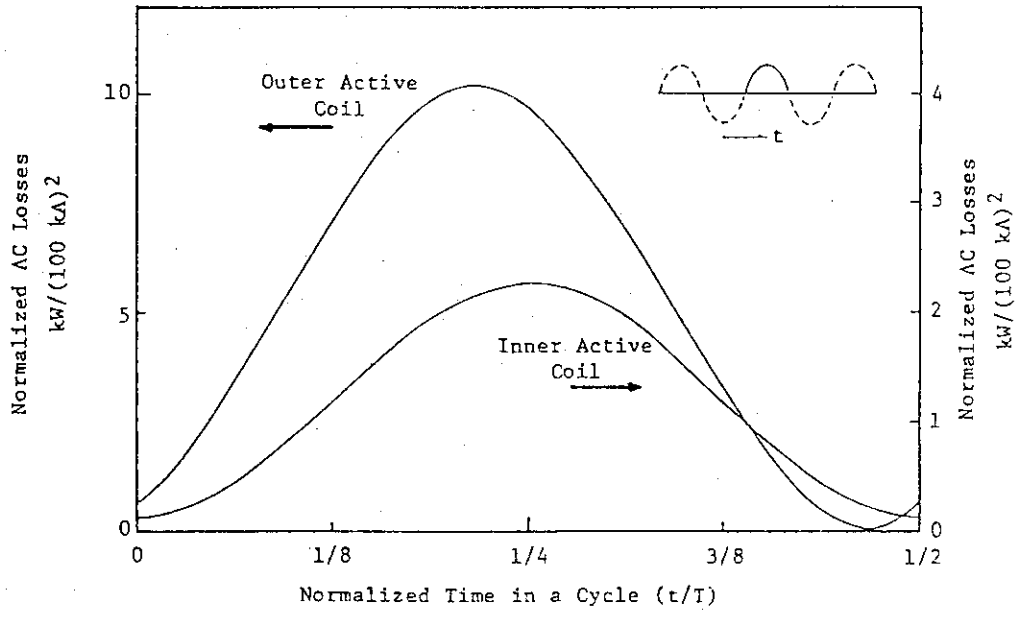

Fig. 4.5 Time behavior of total AC losses in half sector. Peak active coil currents are ~100 kA.

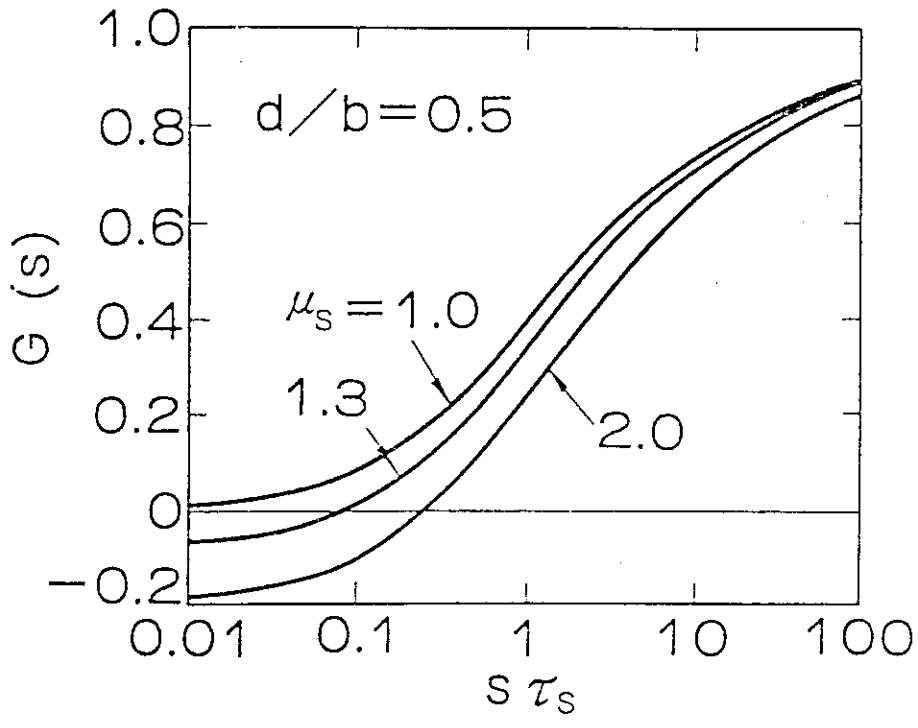

Fig. 4.6(a) Stabilizing function of ferromagnetic structures.

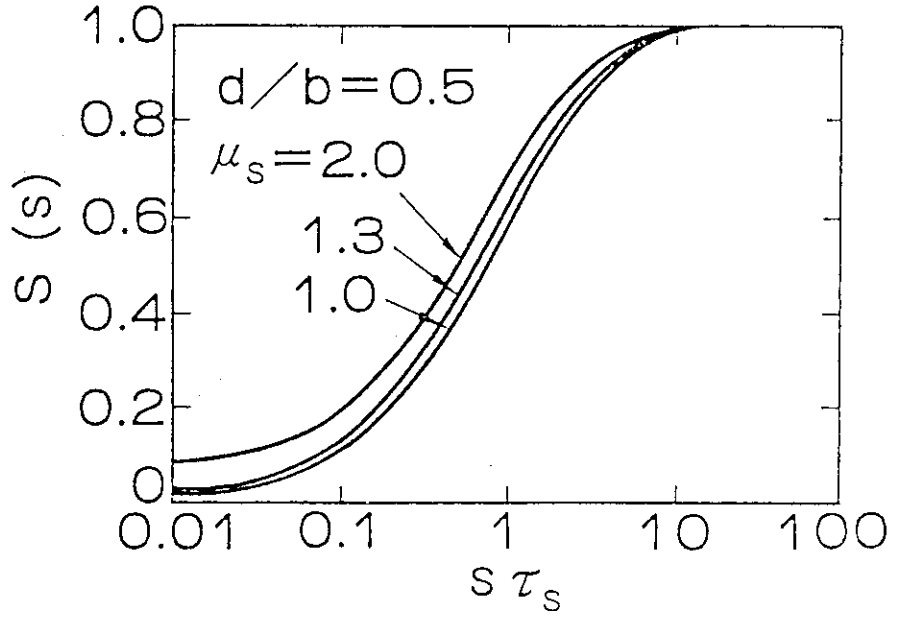

Fig. 4.6(b) Shielding function of ferromagnetic structures.

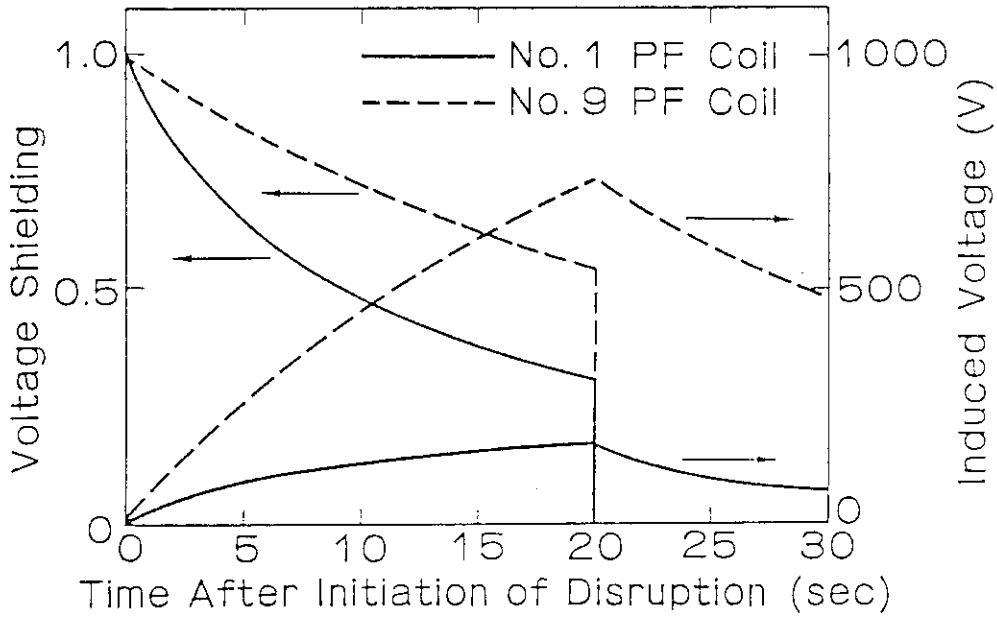

Fig. 4.7 Time behavior of induced loop voltages and voltage shielding effects on PF coils.

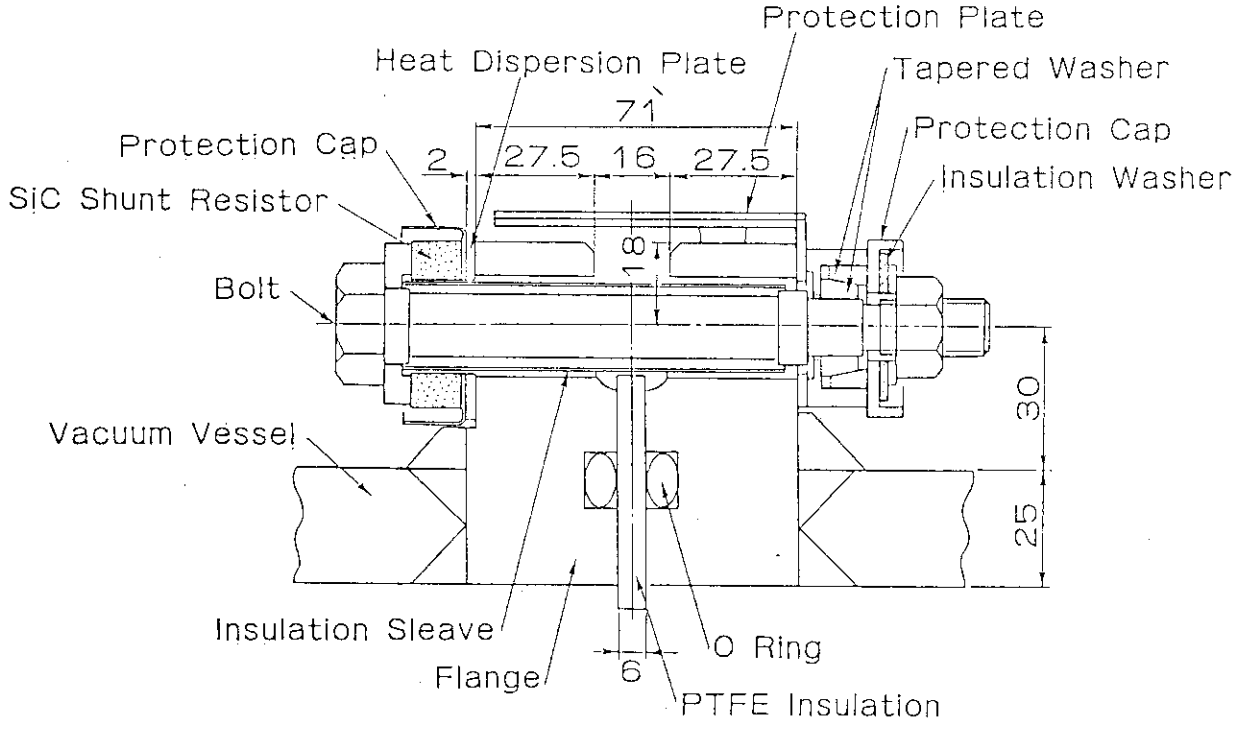

Fig. 4.8 Cross-sectional view of SiC shunt resistor.

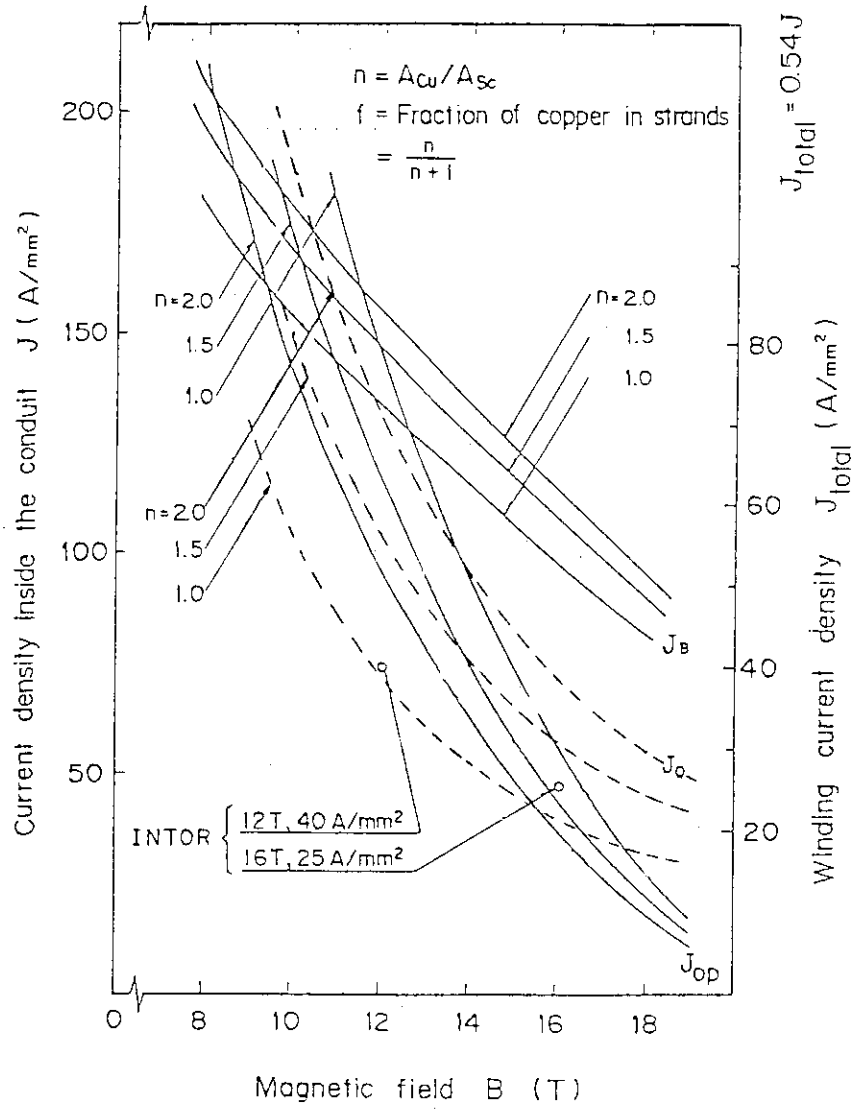

Fig. 4.9 Current density versus magnetic field.

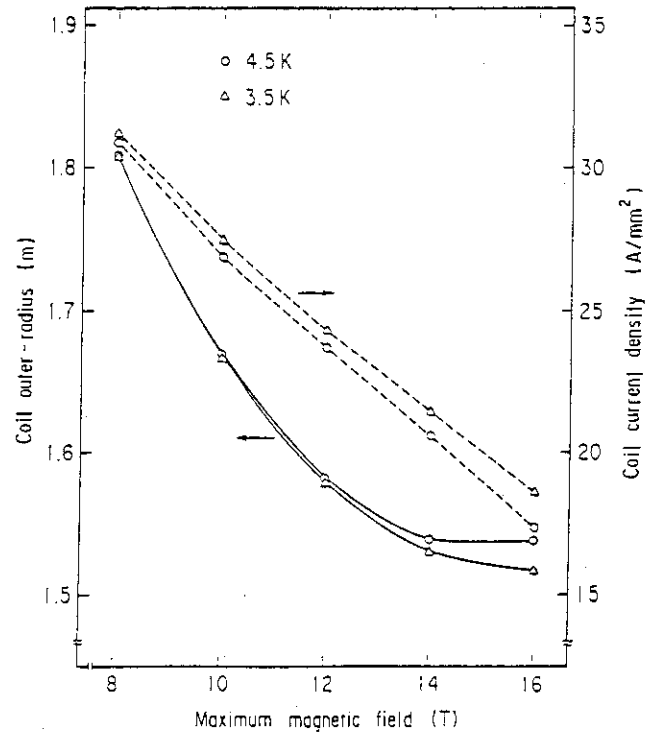

Fig. 4.10 Coil outer-radius and current density.

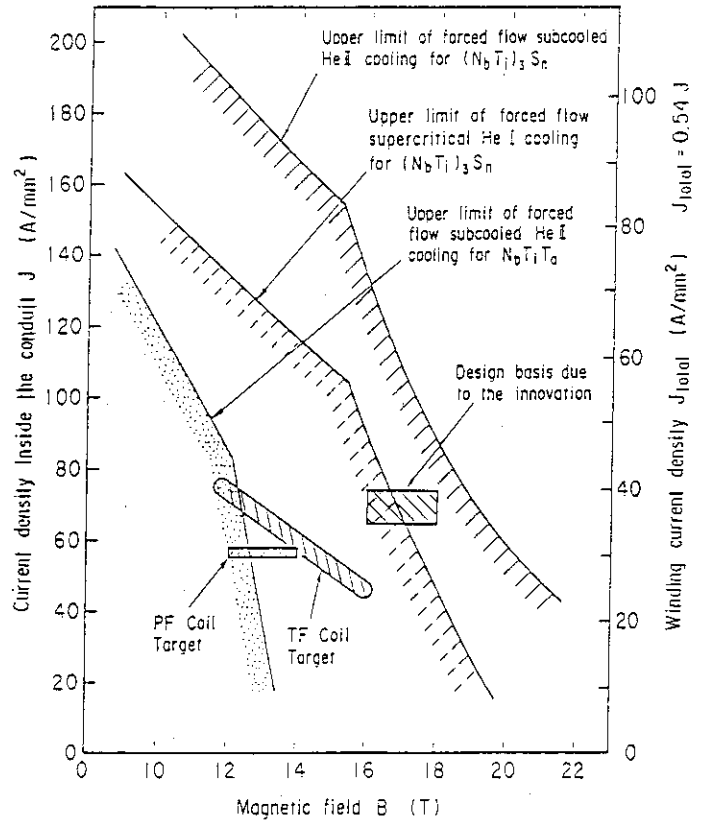

Fig. 4.11 Allowable set of operating current density and magnetic field in the use of each cooling method.

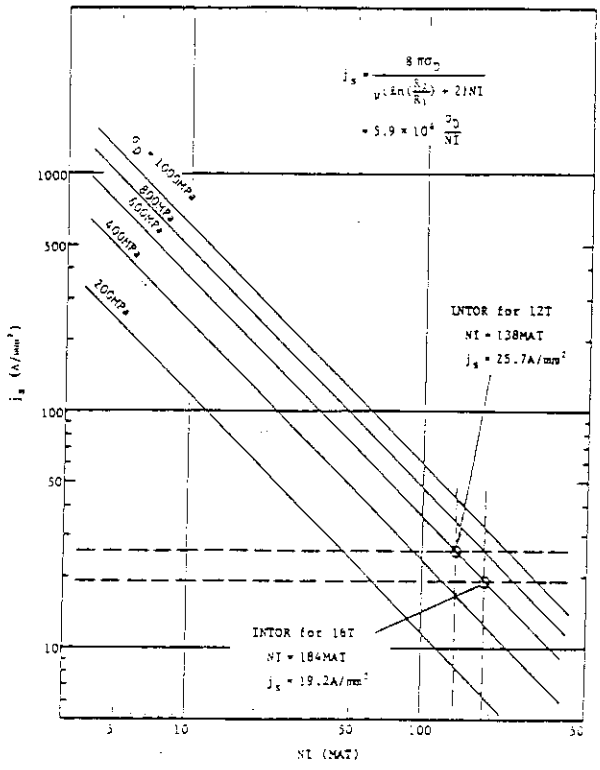

Fig. 4.12 Current density over the structural material in gross cross section of TF coil.

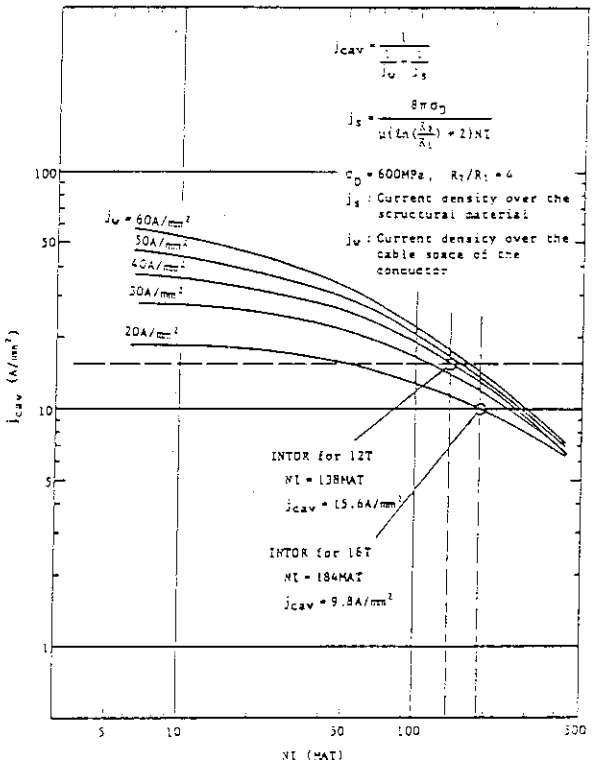

Fig. 4.13 Current density limit in gross cross section of TF coil.

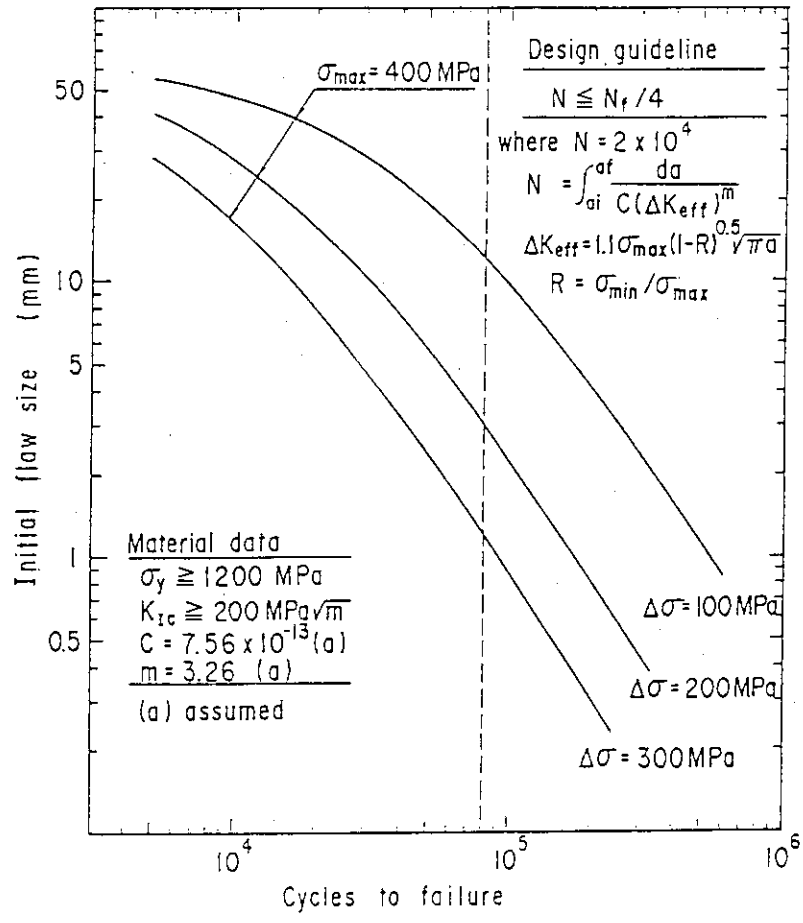

Fig. 4.14 Allowable initial flaw size of the TF coil case based on the fatigue crack growth.

5. Configuration and Maintenance

Based on the planning discussion of Phase IIA Part 3 tasks and outcome of the Specialist Meeting on Tokamak Concept Innovations held on March 1986, the following six tasks are discussed. [16]

(1) Comparative study of vertical and horizontal configurations
(2) Shape memory alloys
(3) Ferromagnetic inserts for ripple reduction
(4) PF coil redundancy
(5) Rapid replacement of divertor and first wall
(6) Containment of tritium and activated dust.

The Summary of each task is presented in the following sections.

5.1 Comparative study of vertical (VA) and horizontal (HA) access configuration

Newly proposed horizontal access reactor concept (reduced size TF coil concept), and vertical access reactor concept were designed. The comparison between the INTOR reference design, the newly proposed horizontal design and the vertical access design were performed from the view point of reactor structure, PF coil optimization, (parameter K=1.5-2.0), reactor interfaces, maintenance procedures, maintenance equipment and availability. Two concepts are shown in Fig. 5.1 and Fig. 5.2.

The judgement of selection is done with the criteria such as, cost, maintainability, reliability, availability, feasibility.

The following are the results and conclusions.

(1) Cost
- . PF coil stored energy and ampere turn of HA are same as that of VA for plasma elongation K=1.6 which is the INTOR reference.
- . PF coil stored energy and ampere turn of HA is higher than VA for K=1.8. However, according to the scoping study, the difference for the reactor systems cost is less than about 3%.

(2) Maintainability
- . Wide space is available for HA maintenance procedures.
- . Retraction movement is simple (one straight line motion on horizontal surface) for HA.
- . Retraction movement is complicated for VA.

(3) Reliability

. Purely vertical hoisting system is existing in BWR refueling system. However, it is very difficult to apply it to obligue retraction of heavy components.

. Feasibility of complex maintenance equipment for VA is a concern because it is a crane mounted system.

. Newly proposed maintenance equipment for HA is the simplest and is based on existing technologies.

. Accurate positioning (0.5mm for heavy structure up to 2000 ton) is demonstrated for HA maintenance system.

(4) Availability

. Availability may be higher for HA for unscheduled maintenance.

. Simultaneous access for 12 for 10 ports is possible for HA.

. Only one port access is allowed for VA because of the use of the crane.

(5) Feasibility

. Blanket structure and support are more rigid for HA. VA has too many segmented components.

. No problems with bellows for both HA and VA.

. Active control coil space is available for HA, but not for VA in reasonable locations.

. Mock-up testing for both VA (1/10 model) and HA (1/4 model) were performed. Feasibility oif HA was demonstrated. However, feasibility of VA was considered quite difficult.

In Conclusion, horizontal access is the best solution from the view point of feasibility, reliability and maintainability. If we consider the trade off between cost and plasma elongation there is no advantage for vertical access regarding cost for the INTOR reference (K=1.6).

For K=1.8, there is 3% cost advantage for VA, however, judging from the difference of cost, feasibility, reliability and maintainability between HA and VA, we conclude that HA is the most appropriate concept.

5.2 Shape Memory Alloy (SMA)

The simplification of maintenance procedure in reactor core structure is one of the important item for operating a D-T fusion reactor like INTOR. Applications of attractive features of SMA to fusion reactors are investigated as a candidate to reduce maintenance time and to simplify maintenance procedures.

The shape memory effect is derived from an austenitic martensitinic transformation of shape memory alloys based on the intermetallic compound like NiTi.

If a shape-memory alloy in the austenitic state is fabricated to its final desired shape and then transformed to martensite, no shape change occurs usually. The martensite can then be deformed easily to a new shape. Upon reheating above the transformation temperature, the shape memory alloy will return to its original shape. This alloy is called as one-way shape memory alloy. If the alloy returns to a deformed shape by transformation to martensite, this alloy is called as two-way (or reversible) shape memory alloy.

Coupling made by such a shape memory alloy requires a minimum of joint preparation and are much simpler and faster than alternatives, such as welding and connecting.

Four types of SMA components which are cooling pipe connectors, C-shaped mechanical quick connectors, metal packing for vacuum seals and SMA jack system are designed. And maintenance scheme and time with these applications are studied. Further, their prototypes are fabricated and successfuly tested. Two exemples are shown in Fig. 5.3 and 5.4.

The following are conclusions:

(1) Shape memory alloys, especially Ni-Ti alloy, are applicable to some components and/or devices of fusion reactors.
(2) Maintenance time is much more reduced than alternatives.
(3) Maintenance equipment is simplified compared with the conventional method.
(4) There is no database on fusion meutron (14 MeV) irrdiation. However neutron irradiation effect is not an obstacle for application of SMA to fusion reactors of SMA is used outside the blanket/shield structure.

Judging from the above results, it is concluded that the application of shape memory alloys is feasible and should be incorporated into reactor structure.

5.3 Ferromagnetic Inserts for Ripple Reduction

The magnetic field in tokamaks is rippled, i.e. its amplitude oscillates slightly along the major circumference of the torus due to the discrte nature of a tokamak magnetic system consisting of N separate TF coils. The existence of toroidal field (TF) ripple leads to enhanced particle and energy losses from the plasma. This TF ripple can be reduced to an acceptable levle, by using a relatively large number of TF coils, or, by using larger TF coils with the outer legs of the coils being far from the plasma region.

However, increasing the number of TF coils decreases the accessibility to the torus sectors of a tokamak reactor between the legs of TF coil. On the other hand, using larger TF coils increases the size of the over all reactor system and as a result increases the cost of the reactor.

Instead of these approaches, some kinds of TF ripple reduction method were proposed up to now. Among them, ferromagnetic iron insert in the neutron shield of the reactor is considered to be one of the most effective and simplest way to reduce TF ripple. In the present study, we apply this method to the INTOR design and analyze the effect of the ferromagnetic insert on ripple reduction.

The effects of the ferromagnetic insert on TF ripple were studied in the design of INTOR with only 10 rather than 12 TF coils. Three dimensional analysis for the magnetic field was carried out using MAGNA/IME-30 computer code. The results obtained are summarized as follows:

(1) Contour maps of the TF ripple with and without the ferromagnetic insert were obtained over the poloidal cross section. With the ferromagnetic iron insert, TF ripple was found to be reduced considerably almost over the plasma cross section, especially, in the outer region near the mid-plane.

(2) Sensitivity analysis with respect to i) the location, ii) the thickness, iii) cross sectional shape and iv) vertical shape of ferromagnetic insert was carried out.

(3) TF ripple value δ_{ripple} ~1.8% (at the mid-phase, Z=0m, R=5.95m) without the ferromagnetic insert can be reduced to the value δ_{ripple} ~1.25%, placing the ferromagnetic insert at the reference location.

δ_{ripple} ~ 1.25%, placing the ferromagnetic insert at the reference location.

(4) Further ripple reduction can be possible, if the ferromagnetic insert is placed more closer to the plasma surface. For example, δ_{ripple} can be reduced to less than 1% for $d_{pc} \leq 1.6$m, where d_{pc} is defined as the distance between the ferromagnetic insert and the plasma surface.

Based on these results, we have shown that TF ripple can be reduced within an acceptable level, even in the design of INTOR with only 10 TF coils, placing the ferromagnetic insert at realistic location and with reasonable dimensions.

5.4 PF Coils Redundany

In the reference INTOR design, the lower PF ring coils placed between the TF coils and the reactor base should be disassembled after the disassembly of the practically whole reactor structures. The option considered here is to install the multiple number of the lower PF ring coils. The main features of this concept are as follows.

(1) A pair of coils is installed at each location and each coil has independent coil structure. Therefore, subcomponents such as current leads and cooling pipes are also equipped for each coil. In the case where a pair of coil is installed in common coil case structures, the damage in oen coil at an accident has a danger to extend to the other coil.

(2) The coil supporting structures are common for a pair of coil at the same location.

The problems ar ethe followings.

1) It is difficult to optimize the coil arrangement for all coils.

2) The independent coils having its own coil case is inferior in space factor in limited installation space.

The conclusions is that the superconducting PF coils should be sufficiently reliable during reactor lifetime and that the PF coils should not be replaced. However, in the case of severe accident, there is a possibility of replacement of the PF coil by PF coil of different size.

5.5 Replacement of Divertor/First Wall for reduced down time

It is widely recognized that the rapid replacement of reactor core structure such as divertor and first wall is one of the important item for effective operation of a D-T fusion reactor.

Replacement of divertor and first wall is considered as one of the most important periodical maintenance tasks in the INTOR phase 2A, Part 2. Divertor and first wall are modular structure with a removable shield and are segmented into 1-2 modules between adjacent TF coils. When a divertor or first wall is damaged, a damaged module is removed and replaced with a new one.

To realize the rapid replacement by considering the above reviews, the following ideas are proposed.

(1) Vacuum should be kept during maintenance procedure to avoid the pre-baking and to reduce the post-baking time.

(2) Only a damaged component such as armor tile on the first walls preferred to be replaced in-situ instead of modular structures. For this purpose, development of an in-vessel inspection system (IVIS) to find out rapidly a damaged component in the vacuum vessel is required.

(3) Use of shape memory alloys (SMA) are considered for vacuum seals, pipe connections and mechanical connections outside the shield structure to perform the quicker replacement of the damaged components. This item is already discussed as one of our tasks.

The divertor module replacement with small cask without breaking vacuum was proposed, as the divertor module is small and light compared with the FW/Blanket module. Concerning the FW/blanket module, replacement with a cask without breaking vacuum may be difficult because it is very large and heavy. Instead, in-situ replacement (for example, first wall armor tile) with articulated boom (manipulator) incorporated cask without breaking vacuum is selected as the best method for first wall replacement. This concept is shown in Fig. 5.5.

The newly proposed concept are studied and compared with the concept of INTOR Phase IIA, Part 2 from various view point. The following results are obtained.

(1) Maintenance tasks become much easier and quicker.

(2) The number of the complicated remote maintenance systems are reduced.

(3) It is more advantageous from the viewpoint of safety of tritium and activated dust because of unnecessity of breaking vacuum seals.

From the above results, it is concluded that the maintenance scheme of in-situ replacement with manipulator system operating in vacuum condition should be incorporated into the reactor design.

5.6 Tritium and Activated Dust Containment

Procedures for tritium and activated dust containment especially for maintenance are presented. Various methods such as carbon coating, use of cask, keeping low temperature at surface, and evacuation of torus by flexible duct for tritium and dust confainment are examined. The reference is proposed by taking account the existing database and feasibility. The main feature of reference is to use the dust confinement cask for blanket/shield and dvertor structure in keeping at low temperature to avoid reemission of tritium. The followings are concepts.

(1) Divertor Module Transfer System

The divertor module transfer system is composed of a transfer container and a divertor transfer machine, comprising a traverse can and a hydraulic telescopic jack. An ice box, which is included by a thermal insulation box at front part of the divertor transfer container, surrounds the divertor place and latent heat of ice used to maintain the divertor plate at low temperature to minimize the tritium released from its surface. The ice box is pushed out with the divertor plate from the thermal insulation box and is dismantled after use in the maintenance room, and the thermal insulation box integrated with the container can be resued without contamination. The container can keep the divertor plate at low temperature for 60 hours. The concept of the container is shown in Fig. 5.6.

(2) Movable Blanket/Shield Transfer System

A movable blanket/shield transfer system is also composed of movable blanket/shield transfer machine nd a movable blanket/shield transfer container. A water chilling instead of an ice box system for removal of the decay heat of the movable blanket/shield is provided with the container since the ehat is relatively large. The movable shield transfer machine comprises roller forks and a travelling system.
The concept of the container is shown in Fig. 5.7.

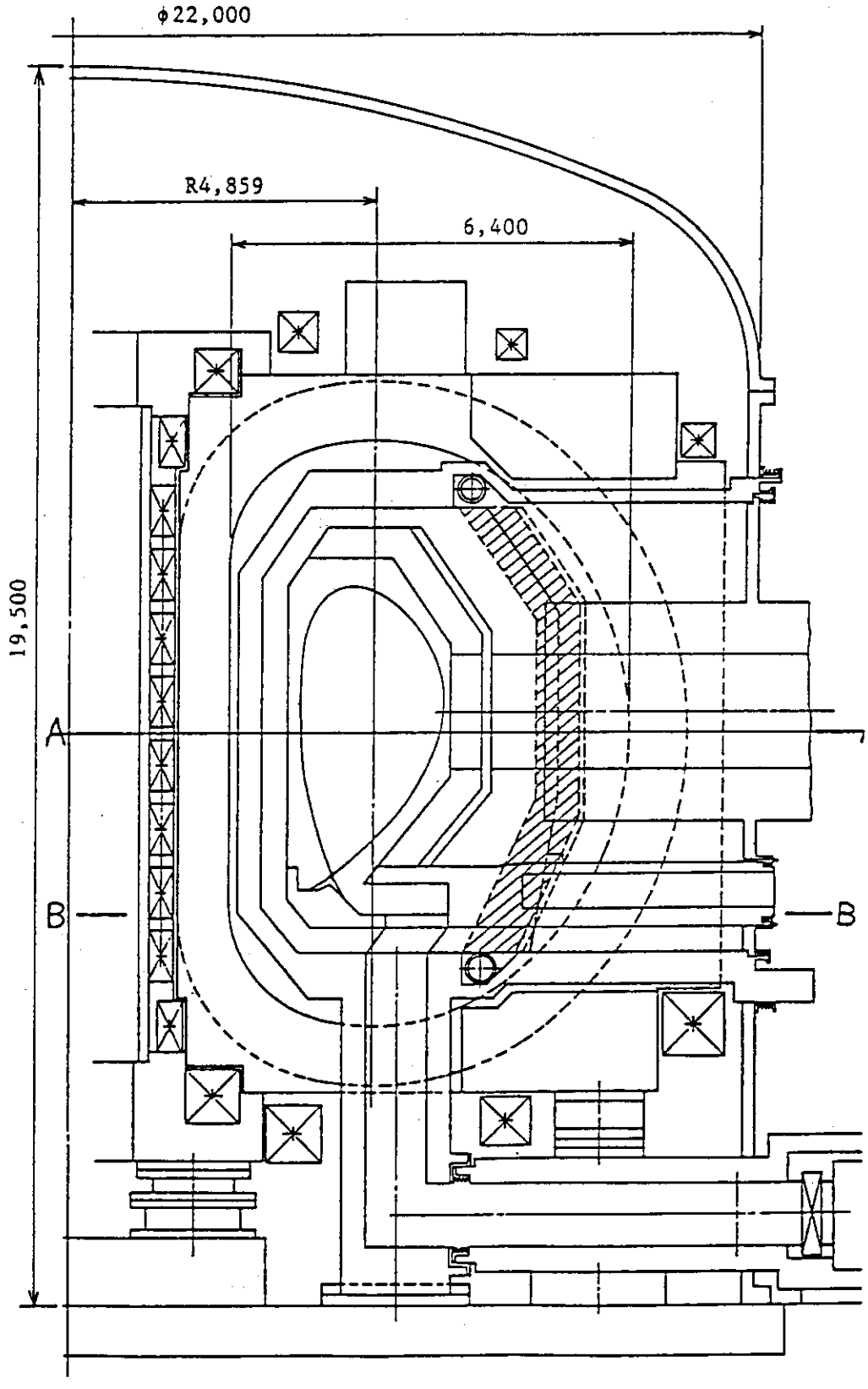

Fig. 5.1 Configuration of horizontal access reactor

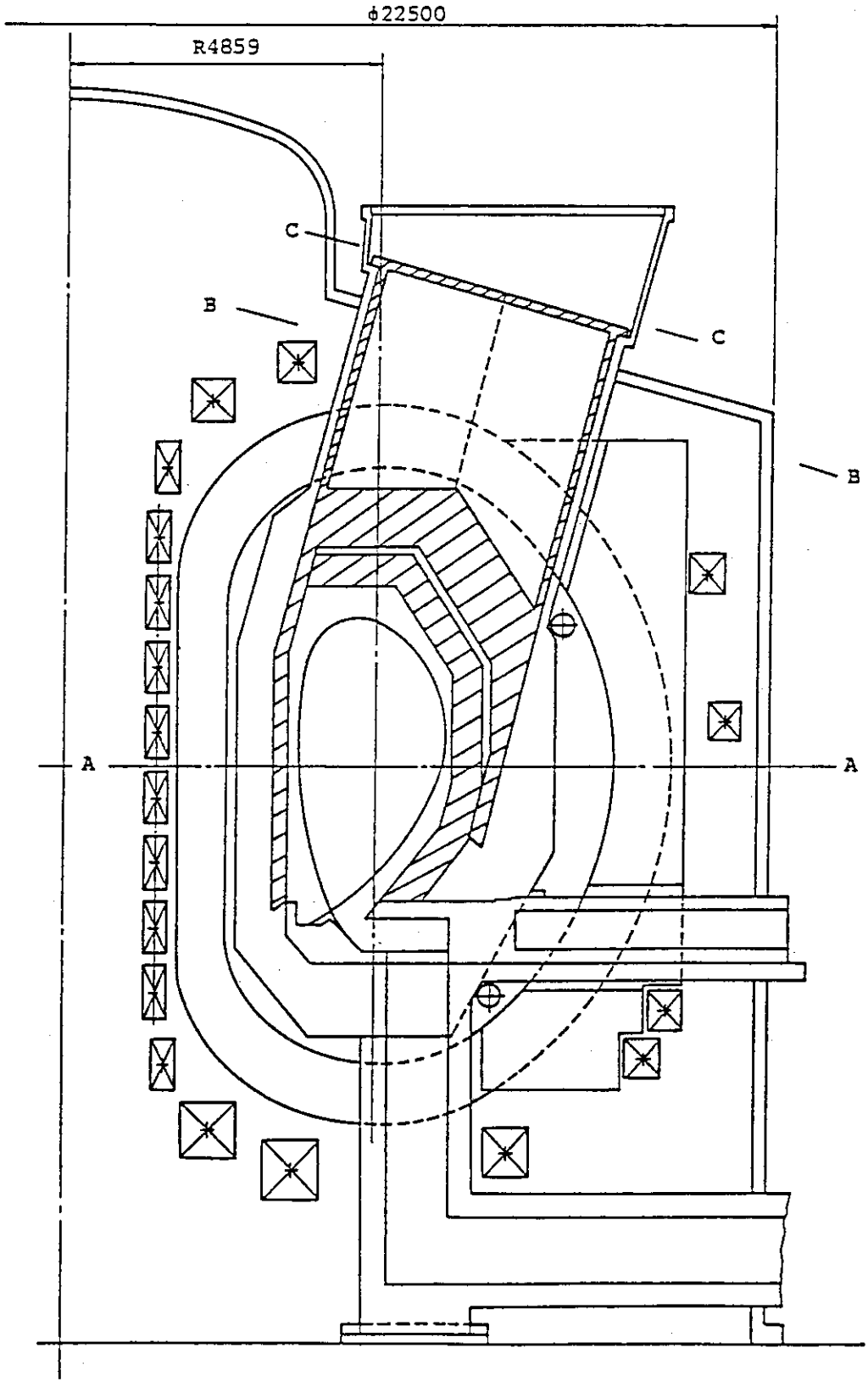

Fig. 5.2 Vertical view of vertical access configuration

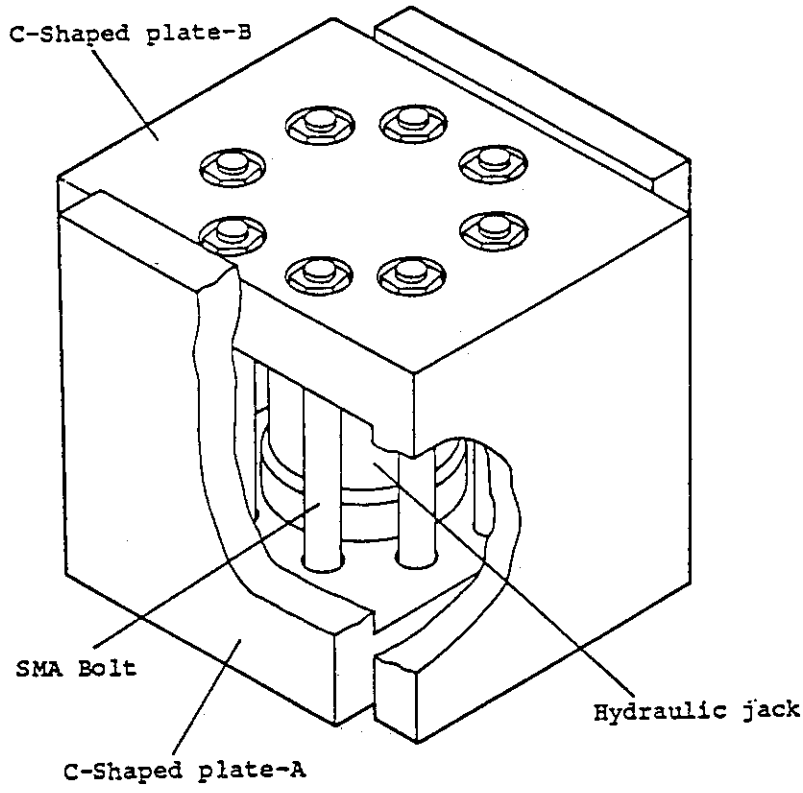

Fig. 5.3 Mechanical quick connector

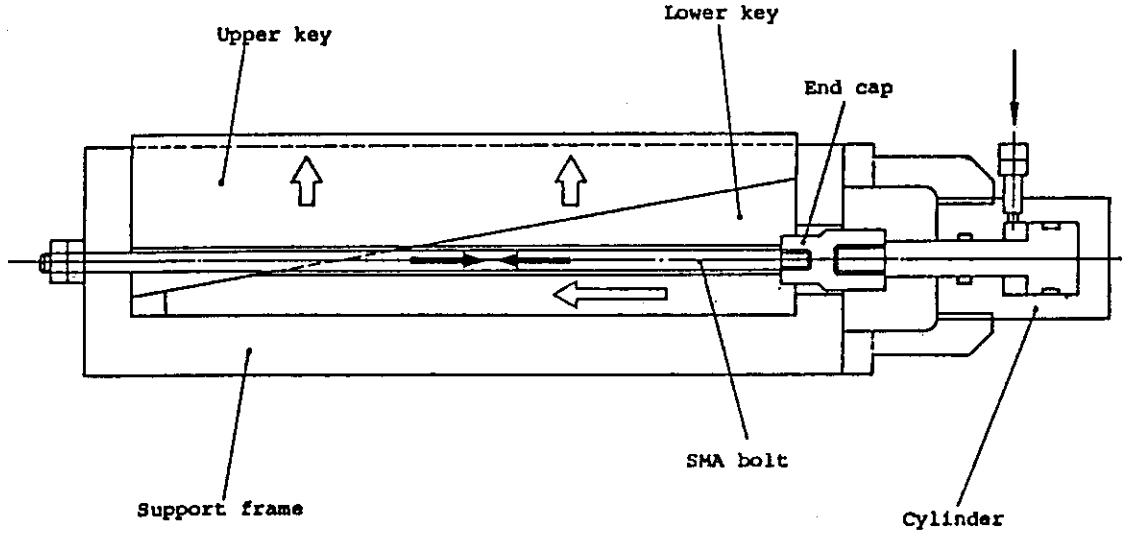

Fig. 5.4 SMA Jack system

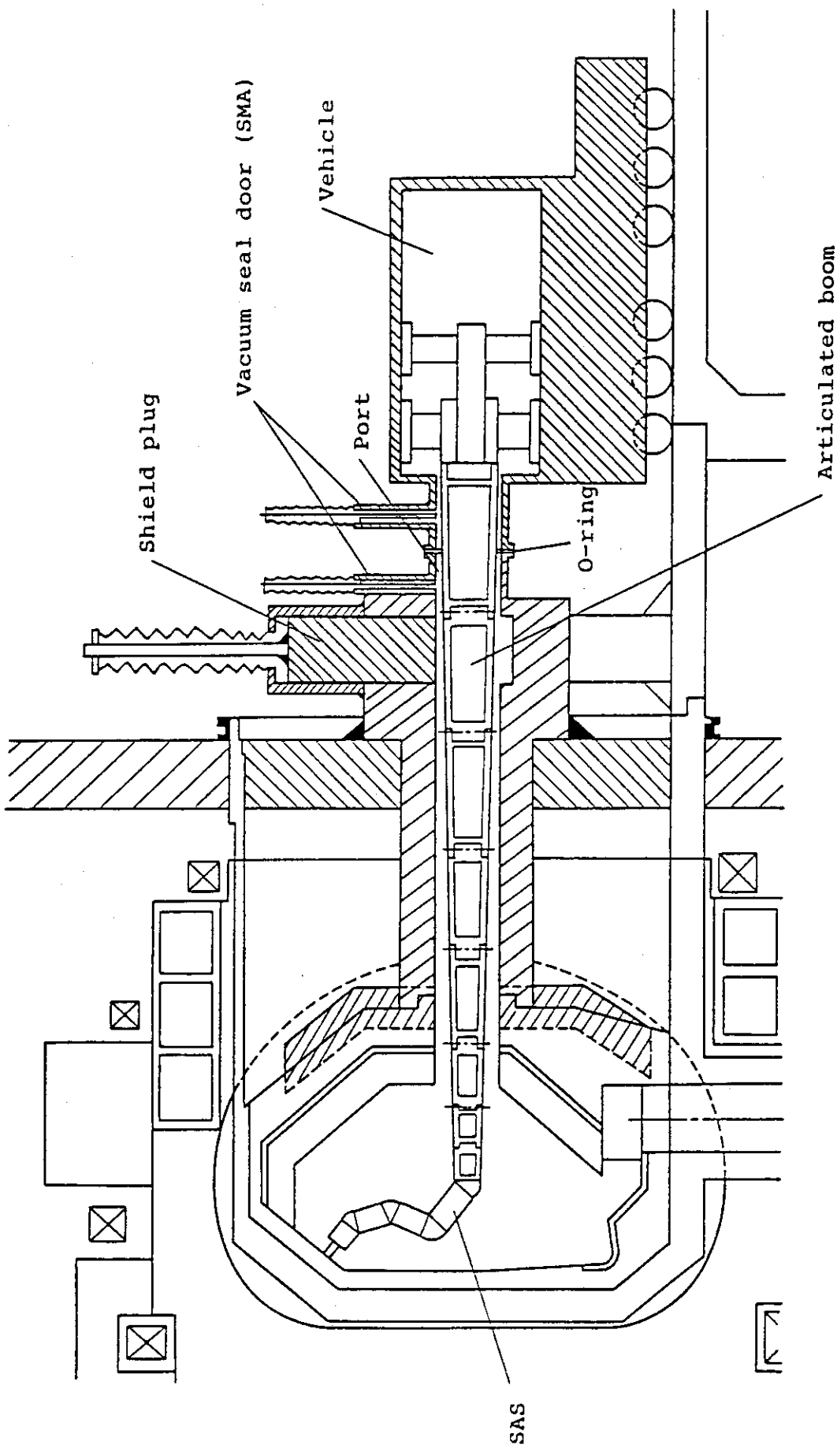

Fig. 5.5 An example of articulated boom

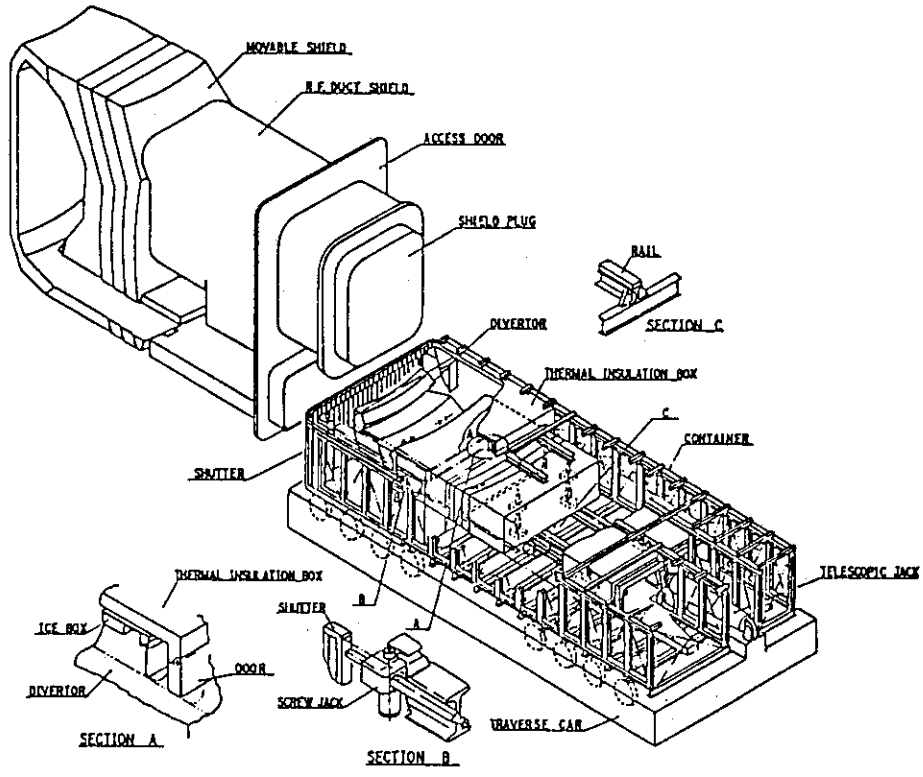

Fig. 5.6 Divertor module transfer system

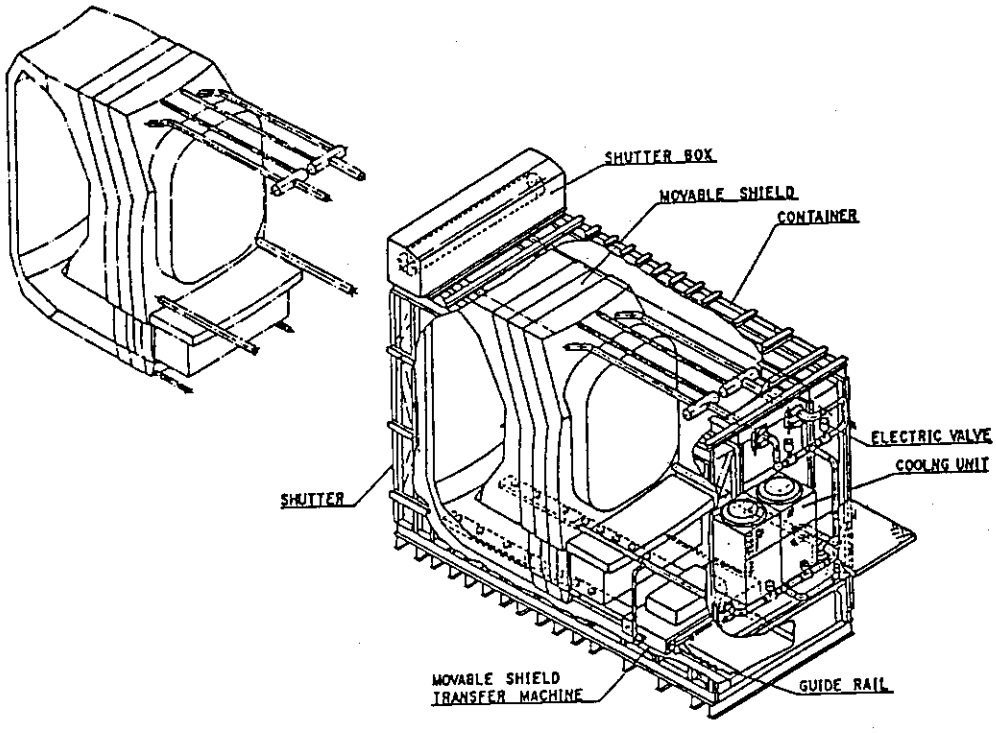

Fig. 5.7 Movable blanket/shield transfer system

6. Blanket and first wall

This chapter includes the summary of Japanese contributions [17] presented at INTOR Workshop Phase 2A, Part 3 relevant to balnket, first wall, and divertor plate designs, blanket engineering tests and new database concerning these areas.

6.1 New database

Presented new database include the following areas:

(i) Ceramic breeder materials data;
(ii) High heat flux materials data;
(iii) High heat flux experiments;
(iv) Fabrication experience.

6.1.1 Ceramic breeder materials data

(1) Mass transfer of Li_2O

Enhanced weight loss in the presence of moisture is one of the critical issues of Li_2O. In order to clarify vaporization/transport characteristics of LiOH(g) in Li_2O pebbles. Ex-reactor experiments were carried out using the sintered spherical Li_2O pebbles with 85% TD. The observed results show that weight loss rate is proportional to the sweep gas flow rate and also to the square root of H_2O vapor pressure. The obtained equilibrium constants for the reaction $Li_2O(s)+H_2O(g) \leftrightarrow 2LiOH(g)$ are in good agreement with JANAF(1971) data.

The redeposition effect of gaseous LiOH formed at high temperature Li_2O zones onto the surface of lower temperature Li_2O zones was also experimentally studied. Figure 6.1 shows the relationship between the temperature of the lower temperature zone and the LiOH(g) deposition efficiency on the lower temperature zone. In the case that the lower bed is maintained at 700℃, 98% of vaporized LiOH at the high temperature zone(1000℃) is effectively captured on the lower zone. This results show that Li_2O pebble of the lower temperature zone at down-stream is effective to decrease the vapor pressure of LiOH.

(2) In-pile tritium recovery tests

The VOM experiments were conducted in the JRR-2 reactor in order to examine the tritium release behavior from Li_2O, $LiAlO_2$, and Li_4SiO_4. The dominant chemical forms in a pure helium sweep gas was mainly HTO and T_2O. Tritium release was enhanced in deutrium bearing sweep gases and the chemical form was changed to predominantly DT and T_2. After theVOM-15H experiment was completed, the retained tritium in the Li_2O was measured to be 0.5 to 0.9 wppm at 760℃ which is much lower than observed in closed capule irradiation tests, TULIP and FUBR-1A.

In the VOM-22H experiment, tritium release rates were simultaneously measured for Li_2O and $LiAlO_2$ spheres loaded into each compartment of the same capsule in order to directly compare their capabilities for tritium recovery.

Sample specifications are follows;

Li_2O : natural ^6Li, 10 μm grain size, 85 %TD, 5mm dia.

$LiAlO_2$: 26% ^6Li, 10 μm grain size, 77 %TD, 4mm dia.

In Fig. 6.2(a) the behavior of tritium release from Li_2O after decreasing temperature to 350, 390 and 470℃ from an initial temperature of 500 or 700℃ are compared. The tritium release rate for Li_2O recovered rapidly at 470℃, but even at 700℃, the tritium release rate of $LiAlO_2$ recovered very slowly, as shown in Fig.6.2(b).

In the VOM-23H experiment, which is one of BEATRIX series, the tritium release rates of Li_4SiO_4 spheres and $LiAlO_2$ rods have been simultaneously measured. Sample specifications are follows;

Li_4SiO_4: natural ^6Li, 14 μm grain size, 89.8 %TD, 4 mm dia.

$LiAlO_2$: natural ^6Li, 0.49 μm grain size, 77.4 %TD, 3.9mm dia.x40mm length

Tritium release rates from Li_4SiO_4 and $LiAlO_2$ after decreasing temperature to 500, 600 and 650℃ from an initial temperature of 700 or 750℃ are shown in Fig.6.3(a)(b). Although the behavior of tritium release from Li_4SiO_4 seems to be similar to that of $LiAlO_2$, it must be recognized that the mean grain diameter of Li_4SiO_4 is larger than that of $LiAlO_2$.

From these results the behavior of tritium release from Li_2O seems to be the best of these candidates for similar temperature and grain size.

6.1.2 Mechanical properties of a W-Cu duplex structure

Mechanical properties at the interface of a W-Cu duplex structure with the nickel-based alloy filler were examined. The specimen used for tests consists of 99.9% purity tungsten and oxygen-free high-conductivity copper. The cyclic fatigue data by torsion fatigue tests are plotted for the tungsten-copper brazed specimen and the copper solid specimen in Fig.6.4. The brazed specimens exhibit the cyclic hardening under the fatigue test. Examinations of the crack propagation indicate that the fatigue cracks have been propagated from the interface to tungsten in the high strain range. The cyclic fatigue data indicate that the lifetime of brazed specimen in the low strain range agrees well to that of copper specimen. The lifetime of brazed specimen in the high strain range depends on the strength of the interface bond and tungsten. The shear stress amplitude for the fatigue crack initiation life of 10^4 cycles has been estimated to be 70 MPa.

6.1.3 High heat flux experiments

(1) A simulated plasma disruption experiments using an electron beam

Simulated plasma disruption experimental study has been made on the melt and/or evaporation characteristics of stainless steel, aluminum, and zinc subjected to an extremely high heat flux, up to 100 MW/m^2 for durations of

90-180 ms using an electron beam facility. An existing electron beam facility was improved to provide higher heat fluxes uniformly over a wider area by installing a high speed beam rastering system. An analytical code capable of treating melting and evaporation has also been developed along with the experiments, and both experimental and analytical results were compared. For the stainless steel, the experimental data on the melt layer thickeness become significantly greater than analytical predictions.

(2) A thermal cycling durability test of W-Cu duplex structure

A durability test of the W-Cu duplex structure against thermal cycling was performed. A tungsten disk was bonded to a copper disk by means of brazing or direct casting. The tungsten surface of the test piece was periodically heated by a high temperature argon plasma jet with an average heat flux of 0.7 MW/m^2. Before and after the tests, the test piece was examined with the aid of a scanning electron microscope and the Knoop hardness was measured. Grain boundary microcracks were observed after 200 and 1100 cycles in brazed tungsten samples which contained a small amount of nickel and phosporus. A cast tungsten specimen subjected to 2200 thermal cycles also contained microcracks. However,microcracks were not observed in a brazed tungsten for thermal cycles up to 3700 times. None of the test specimens were broken. It is found that brazing is a valid bonding method and that W-Cu duplex structure, especially of with high purity tungsten, are able to endure a practical number of thermal cycles.

6.1.4 Fabrication experience

Fabrication studies of stainless steel first wall panels by HIP (Hot Isostatic Pressing) and metallic bonding of graphite to stainless steel by diffusion have been carried out. And in order to evaluate the integrity of HIP bonded joints, mechanical tests were carried out for the joint. The obtained results are summarized as follows:

(i) A complex first wall panel with coolant channels can be fabricated by HIP using the grooved-plate technique, and more stable fabrication of the first wall panel can be achieved by the rectangular-tube technique;
(ii) A complex 3-D first wall can be fabricated directly from 3-D joints by HIP;
(iii) The obtained mechanical data show that the mechanical strength of bonded stainless steel first wall specimen have same strength as base metal;
(iv) Diffusion bonding of graphite to stainless steel can be done by using titanium and Invar alloy insert metals;
(v) HIP equipment with larger capacity should be developed for a production use.

6.2 Tritium breeding blanket

According to the INTOR design constraints shown in Table 6.1 [5], a comparison study of blanket concepts and design studies of candidate blankets have been carried out. The most important constraint in the present INTOR is the requirement of tritium self-sufficiency. In order to meet the tritium self-sufficiency goal, the blanket must have potentiality to obtain a net tritium breeding ratio greater than unity with the blanket coverage of 60 %.

6.2.1 Comparison study of blanket concepts

Leading blanket concepts were selected from a comparison study. In this study, the following representative materials are considered:

- breeder ceramics Li_2O, $LiAlO_2$, Li_4SiO_4
  liquid Li, 17Li-83Pb, Li-salt
- neutron multiplier Be
- coolant H_2O, He, self-cooling

Austenitic stainless steel was selected as an only reasonable structural material for INTOR judging from the present databse.

Among ceramic breeders, Li_2O has the best tritium breeding performance and tritium release behavior. And it is a great merit for Li_2O to be able to obtain enough TBR without ^6Li enrichment. Though Li_2O has problems of mass transfer, swelling, compatibility with Be, it will be possible to solve them by the future design and R&D efforts.

Major problems of 17Li-83Pb are corrosion and tritium containment. And preparation of pre-heating system for 17Li-83Pb extraction line.

Liquid Li self-cooilng concept may lead to a simpler blanket concept, however, has great concerns of MHD effect, electromagnetic force, compatibility with structural material and safety for near-term machines.

The aqueous Li-salt self-cooling blanket will bring a simpler blanket structure, however, it has the problems on corrosion of structure materials and much tritium inventory in primary coolant system and additional tritium extraction system.

Consequently, two blanket concepts(Li_2O/Be/H_2O, Li_2O/Be/He) are selected as leading blankets for INTOR.

6.2.2 Design description of cadidate blankets

A tube-in-shell type of BOT (Breeder Outside Tube) is employed as illustrated in Fig.6.5. Bare type of first wall integrated with the blanket vessel is adopted in order to obtain a high tritium breeding performance by reducing the amount of the structural material and coolant in front of the breeding zone. Annealed stainless steel is selected for the structural material considering its fabrication process by HIP. Charging form of Li_2O breeder is designed to be

small spherical pebbles which has the following advantages:

a) Small pebbles (e.g.～1mm diameter) prevent a large temperature diffence in the breeder which causes thermal cracks;
b) Large surface area per unit volume of breeder gives effective condensation of LiOT(g) or LiOH(g) generated in the high temperature zone;
c) Charging method of the breeder into the blanket vessel will be easiser than those of other breeder forms.

Beryllium pebbles in the same form as the breeder are homogeneously mixed with Li_2O. Mixing ratio of Be is designed to be 75 % to obtain the highest TBR and to prevent the reduction of TBR due to Li burnup. Breeder temperature is controlled for tritium recovery by helium gap arround cooling tubes and appropriate tube arrangement acccording to attenuating deposited nuclear heat in the breeder zone considering the effect of pulse operation mode. Tritium produced in the blanket is recovered by helium purge gas stream.

6.2.3 Major design parameters of candidate blankets

Major design parameters are shown in Table 6.2. Estimated local tritium breeding ratio is ～1.6 which gives a net tritium breeding ratio of nearly unity with the coverage of 60 % and without ^6Li enrichment. Burnup of ^6Li during the reactor lifetime of 3 MW.a/m^2 is about 2 % and this will not affect the neutronics performances significantly. This TBR will be possibly improved (9～28%) by placing neutron multiplier(e.g. lead) in the non-breeding inboard region. Estimated tritium inventory of this blanket concept is less than 400 g. The weight loss of Li_2O by mass transfer is estimated about 1 % of the initial charged Li_2O even if the whole breeder temperature is kept to be 1000℃ assuming the water leakage rate of 10 g/h. And as clarified by experimental investigation, this vaporized LiOT in the high temperature region is expected to condense effectively in the lower temperature zone during the transport by helium purge gas. The deposited LiOT will decompose easily to Li_2O and T_2O.

6.3 First wall

Wide discussions on first wall concepts for INTOR have been done. Two types of first wall concepts are evaluated:

(i) Bare stainless steel first wall concept;
(ii) Protected first wall concept.

The choice of low-Z material for first wall protection is a key feature of INTOR first wall concept.

6.3.1 Structural material

It is preferable to use in INTOR non-reactor-relevant concept with low pressure/low temperature water as a coolant, although many kinds of first wall

designs have been studied. Austenitic stainless steel is selected as the only reasonable structural material for the low temperature first wall considering the INTOR operating condition and material database. Solution annealed condition is a preference because high temperature fabrication techniques such as brazing and HIP will anneal structure.

6.3.2 Design concepts

6.3.2.1 Bare stainless steel first wall concept

The first wall concept consists of a bare stainless steel water-cooled panel fabricated by HIP process and EB welding, and integrated with the blanket module. The thickness of the panel facing the plasma is limited by thermal stress and/or fatigue criteria. Primary advantage of the bare steel wall is design simplicity and a well-established database.

6.3.2.2 Protected first wall concepts

Two types of first wall protection are studied.

(1) Mechanically attached protection tile concept

This concept has the following main features:

- With radiation cooled graphite tiles on blackened austenitic steel first wall structures, relatively high nominal peak heat fluxes can be achieved for relatively short burn pulse operation (~100 sec) considering residual tile heating;
- For repair individual tiles may be replaced in-situ without removal of the whole first wall blanket segment.

However, general concerns exist for the integrity of the tile attachment for mechanical solutions and for in-situ maintenance technologies.

(2) Local protection concept by "guard limiters"

Guard limiter is a new protection concept which defends the first wall against the intensive heat loads during plasma disruptions. The concept of guard limiters is shown in Fig.6.6. The guard limiters consist of 12 inboard and 12 upper limiters. Both limiters can be removed with straight motion through the TF coils. The coverage of the inboard limiters is about 20 % because of the narrow space between TF coils. The important features of this concept are:

- The stainless steel substrates slides on the guide in the first wall;
- The graphite (or C/C composites) tiles are bonded on the substrates for the purpose of trustful cooling in normal burning;
- Maintenance without breaking plasma vacuum is possible by using the vacuum flask.

Fine grain graphite and/or carbon fiber composites (C/C) are selected as armor material from a thermo-mechanical viewpoint. The most attractive features are their unique high temperature capability limited by sublimation instead of

melting and superior thermal shock resistance.

However, the following major drawbacks are associated with graphite first wall protection :

a) A limited irradiation lifetime of < 1 MW.a/m^2;
b) The retention and release of hydrogen and impurities which will lead to required baking temperature above 350 ℃ and high impurity levels;
c) Formation of amorphous carbon deposits and concern for higher tritium inventory;
d) The significant erosion due to physical and chemical sputtering.

6.3.2.3 Reference concept

The guard limiter concept is selected as a reference for INTOR because of the following main reasons:

(i) Protection of first wall structure for a wide range of currently rather uncertain disruption scenarios;
(ii) Easy maintenability of damaged protection structures;
(iii) Improved impurity control.

6.3.3 Lifetime analysis

6.3.3.1 Bare stainless steel first wall

(1) Allowable peak heat load for normal burning

Allowable surface heat fluxes of bare stainless steel first wall were evaluated by two dimensional elastic calculation based on the ASME code. It is concluded that the allowed peak nominal heat flux for a fatigue life of 2×10^5 cycles is around 0.4 MW/m^2 for the bare first wall thickness of 3 mm.

(2) Crack propagation analysis for normal burning

To evaluate the integrity of bare first wall with cracks for normal heat load, crack propagation estimates were carried out. The initial cracks were assumed to be semicircle with 0.1, 0.5 and 1 mm in depth. And, the location was also assumed to be on the surface facing plasma and on the surface facing coolant. The peak surface heat flux of 0.4 MW/m^2 was assumed in this study. In case of coolant side cracks, no crack growth is expected for all cases after 2×10^5 cycles. In case of plasma side cracks, initial crack of 1 mm becomes 1.3 mm after 2×10^5 cycles. From this result, it seems that the bare stainless steel first wall with small cracks will keep the integrity for INTOR normal operation.

(3) Elasto-plastic analysis for disruption conditions

Two dimensional elasto-plastic analyses for new disruption conditions have been performed for bare first wall. A pointwise lifetime estimation which means the estimation of allowable disruption numbers for each point in first wall have

been carried out from the strain range at each point using the ASME design fatigue curve. According to this estimation, the unacceptable fatigue damage due to disruptions will be limited in a depth of less than 0.5 mm near the plasma surface. In order to estimate the stability of this crack, two dimensional elasto-plastic fracture mechanism by $\hat{J}$ integral was applied for new disruption conditions. From this evaluation, it is concluded that no unstable crack growth due to disruptions will occure since estimated $\hat{J}max$ is much smaller than the J1c of 316 SS at a room temperature.

6.3.3.2 Protected first wall

(1) Allowable peak heat load for normal burning

The allowable temperature of graphite armor surface can be restricted by the impurity of graphite vapor. Assuming the plasma pressure of 1.3×10^{-3} Pa and impurity limit of graphite 5%, the maximum temperature of graphite surface is limited to ~1750 ℃. It is estimated that the maximum surface heat load for radiatively cooled graphite first wall by darken-treatment of the SS surface is around 0.4 MW/m².

(2) Elasto-plastic analysis for disruption conditions

It is expected that the surface area will be damaged for INTOR disruption conditions. Energy release rate $\hat{J}$ integral was calculated for estimating crack behavior of exceptional disruption condition. Reactor grade fine graphite IG-110 was assumed for the study. The result shows that the $\hat{J}1$ is quite small because of small tensile stresses at the end of cooling process and $\hat{J}II$ seems to be dominant for crack propagation. According to the estimation, $\hat{J}II$ value does not exceed the critical value within a depth of 0.3-0.4 mm. However, crack propagation estimation has many uncertainties and database for fracture toughness are very poor. It will be necessary to verify lifetime predictions with test data for prototypical geometries and operating conditions.

6.4 Blanket engineering tests in FER

Considering the request of tritium self-supply for a future power reactor, it is inevitably important to develop the technology of producing tritium in a fusion reactor itself. Though no driver tritium producing blanket is installed in FER, blanket engineering tests are planned by using blanket test elements and test modules.

To achieve the steps of physics and engineering goals successively, staged operation has been planned for FER as shown in Table 6.3. And, major requirements in order to obtain useful data by engineering tests are summarized in Table 6.4. Lifetime neutron fluence of about 0.3 MW.a/m² is decided judging from

achievable engineering tests, reasonable operation period, present blanket technology and externally obtainable tritium. From the viewpoints of mechanical and shielding performances, FER has a capability to accomodate to the higher fluence operation. Neutron wall loading of about 1 MW/m^2 is an appropriate value from the viewpoints of probable extrapolations to DEMO and the present technology of plasma facing components.

Major basic engineering tests on blanket performances such as neutronics, thermal-hydraulics, tritium recovery etc. can be performed by test elements and modules. Tests for irradiation effects of structural materials and reliability by long-term operation are considered impracticable in FER. Though demonstration of electricity generation is not planned in FER, staged operation by installing a large sector-size test component will enable to conduct this testing.

Tests in complementary facilities should be naturally required to obtain basic data.

Table 6.1 Main design constraints for the INTOR blanket and first wall

Item		INTOR
Lifetime neutron fluence	MW.a/m²	3 (max.)
Availability	%	25
Mean neutron wall load	MW/m²	1.3
Net tritium breeding ratio		~1.0
Blanket coverage		0.6 - 0.8
Nominal Condition		
Burn time	s	> 200
Cycle time	s	> 270
Total number of pulses(Inductive scenario)		2 x 10^5
Peak surface heat flux		
without ripple	MW/m²	0.18
with 1.2 % ripple	MW/m²	0.4 - 0.9
Total erosion of steel	mm	0.3
Permited coolant leakage	g/s	$10^{-5}(H_2O)/10^{-4}$(He)
Disruption Condition		
Normal case		
total number		400
deposited energy		
-uniform on first wall[1)]	MJ	30
-local on first wall[2)]	MJ	30
peak energy flux	MJ/m²	1.1
deposition time	ms	20
Exceptional case		
total number		40
deposited energy		
-uniform on first wall[1)]	MJ	145
-local on first wall[3)]	MJ	145
peak energy flux	MJ/m²	2.9
deposition time	ms	2 - 5
Hotspots by run-away electrons		possible
Other aspects		
Start up		
min. bake out temperature	℃	150
low-Z limiter		yes
run-away electrons		possible
Structure material		austenitic stainless steel
Passive plasma stabilization		to be checked

1) radiation
2) on 30 m² at the center of the inboard wall
3) to 30 % of the first wall with an additional peaking of 2

Table 6.2 Main design parameters of tritium breeding blankets

	$Li_2O/Be/H_2O/AS$*	$Li_2O/Be/He/AS$*	
		(A)	(B)
Blanket Thickness	500 mm (including first wall)		
First Wall	integrated with blanket		
Thickness	15.5 mm (2.5/5/8 mm)	18.0 mm (2/7/9 mm)	
Material	type 316 stainless steel (316SS)	titanium modified austenitic stainless steel (PCA)	
Coolant	H_2O	He	
Pressure	1.5 MPa	4.0 MPa	
Temperature (In/Out)	60/100 °C	100/300 °C	
Flow Direction	toroidal	toroidal	
Channel Area	5 mm^w x 5 mm^d	7 mm^w x 7 mm^d	
Pitch	7.5 mm	9.5 mm	
Maximum Velocity	2.7 m/s	78 m/s	
Pressure Losses	~ 90 kPa	~ 160 kPa	
Wall Maximum Temperature	< 200 °C	< 400 °C	
Breeder Region			
Material	homogeneously mixed Li_2O and Be pebbles of 1 mm in diameter		
Packing Fraction	70% in bulk and 30% at near wall		
Mixing Ratio	25 v/o of Li_2O and 75 v/o of Be		
Li_2O Density	85 %T.D.		
^6Li Enrichment	natural		
Tritium Breeding			
Local TBR	1.54	1.65	
TBR with HTB concept			
Breeder Temperature			
Operation	450 - 750 °C		100 - 650 °C
Allowable Range	400 -1000 °C		<1000 °C
Minimum Temperature Control Method	helium gas gap around coolant tubes		none
Coolant Tube	316SS	PCA	
Size (ID/OD)	8/10 mm	20/24 mm	
Coolant	H_2O	He	
Pressure	1.5 MPa	4.0 MPa	
Temperature (In/Out)	60/100 °C	100/300 °C	
Flow Direction	poloidal	poloidal	
Maximum Velocity	4.7 m/s	72 m/s	
Pressure Losses	~ 300 kPa	~ 100 kPa	
Tritium Recovery	continuously with purge gas stream		discontinuously during reactor shutdown
Purge Gas	He (0.1 MPa)		He (0.1 MPa)
Flow Rate	200 Nm^3/hr		2400 Nm^3/hr (recovery time)
Heat-up			up to 450 °C with Primary Cooling System
Recovery Time			about 1 day

* AS: austenitic stainless steel

Table 6.3 Engineering test shedule of FER

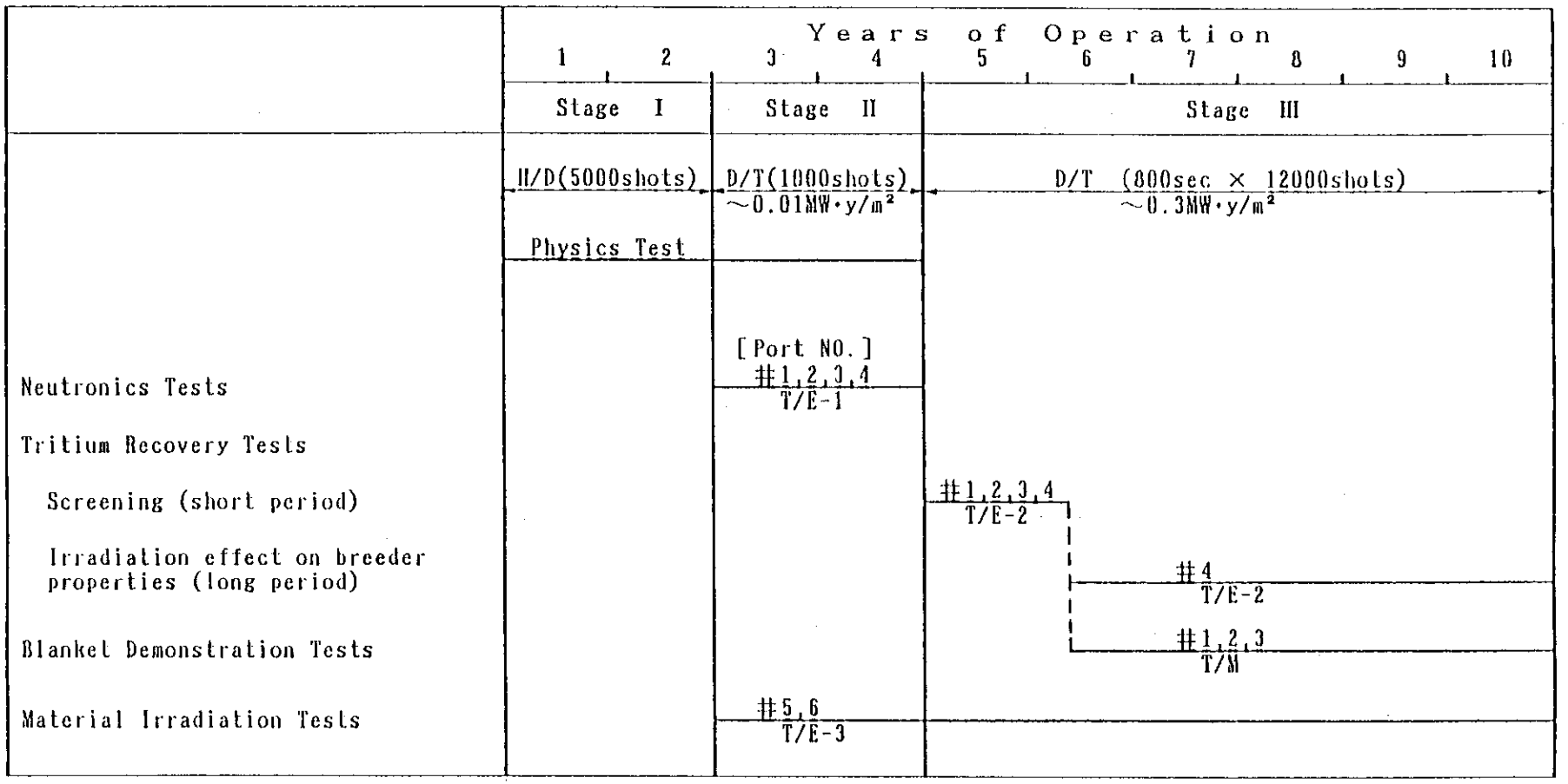

Number of Test Port : 6

Test Element-1 : 2/port

Test Element-2 : 4/port

Test Element-3 : 4/port

Test Module : 1/port

Test Sector : TBD

Table 6.4 Test requirements for FER

	Fluence	Operation Mode	Test Part Configuration
1) Neutronics Tests			
① Tritium breeding	a few pulses		T/E－1
② Nuclear heating rate	a few pulses		T/E－1
2) Tritium recovery tests			
① Saturation of tritium inventory	0.01～0.02MW·y/m²	$\Sigma t_{burn} \geq$ 4～5day	T/E－2, T/M
② Quasi-steady state of breeder temperature		continuous pulsed operation for front region of blanket $\Sigma t_{burn} \geq$ 1000s rear region of blanket $\Sigma t_{burn} \geq$ 10000s	T/E－2, T/M
③ Holding of breeder temperature		$t_{dwell} \leq$ 400s (for t_{burn} = 800s) $t_{dwell} \leq$ 300s (for $T_{min} \geq$ 400°C)	T/E－2, T/M
④ Continuous testing time for data confirmation		several days	T/E－2, T/M
⑤ Irradiation effect on breeder	≧ 0.2MW·y/m²		T/E－2
3) Material Irradiation Tests			T/E－3
① Insulator	～ 0.2MW·y/m²		
② Armor	～ 0.2MW·y/m²		
③ Structural material	≧ 3MW·y/m²		
4) Sector Blanket Test (TBD)			T/S
① Confirmation of breeding performance			
② Electricity generation			
③ Poroidal/toroidal temperature distribution			
④ Coolant flow distribution			
⑤ Integrity for vessel internal pressure, thermal stress, and electromagnetic force			

T/E－1 : Test Element-1 (～1m^w ×0.5m^h ×0.5m^t)
T/E－2 : Test Element-2 (～0.4m^w ×0.5m^h ×0.15m^t)
T/E－3 : Test Element-3 (～0.4m^w ×0.5m^h ×0.15m^t ,small articles in the Element)
T/M : Test Module (～1m^w ×1.7m^h ×0.5m^t)
T/S : Test Sector (～3m^w ×4.5m^h ×0.5m^t)

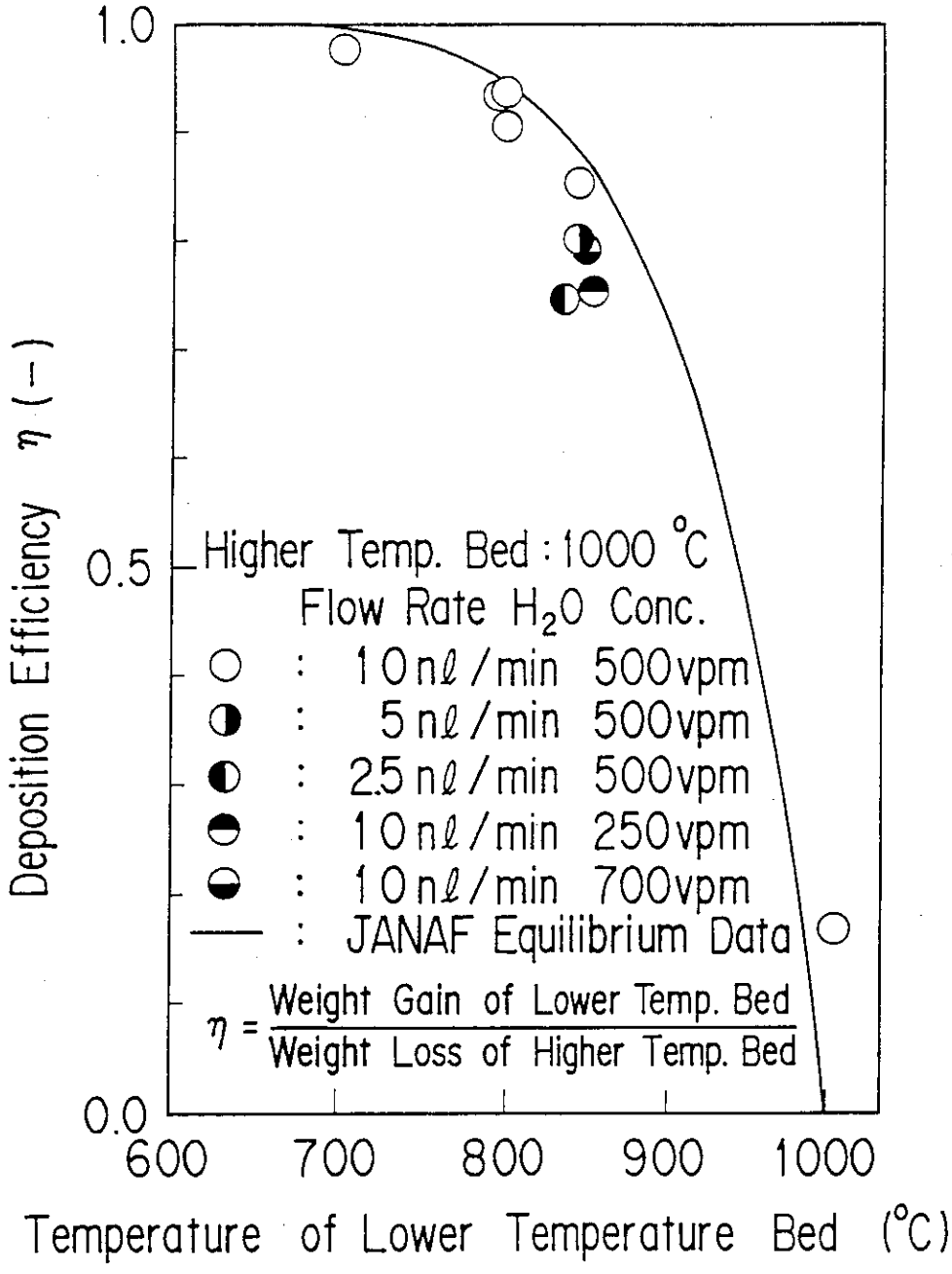

Fig. 6.1 Deposition efficiency of LiOH transfered at high temperature Li_2O (1000°C) as a function of lower temperature

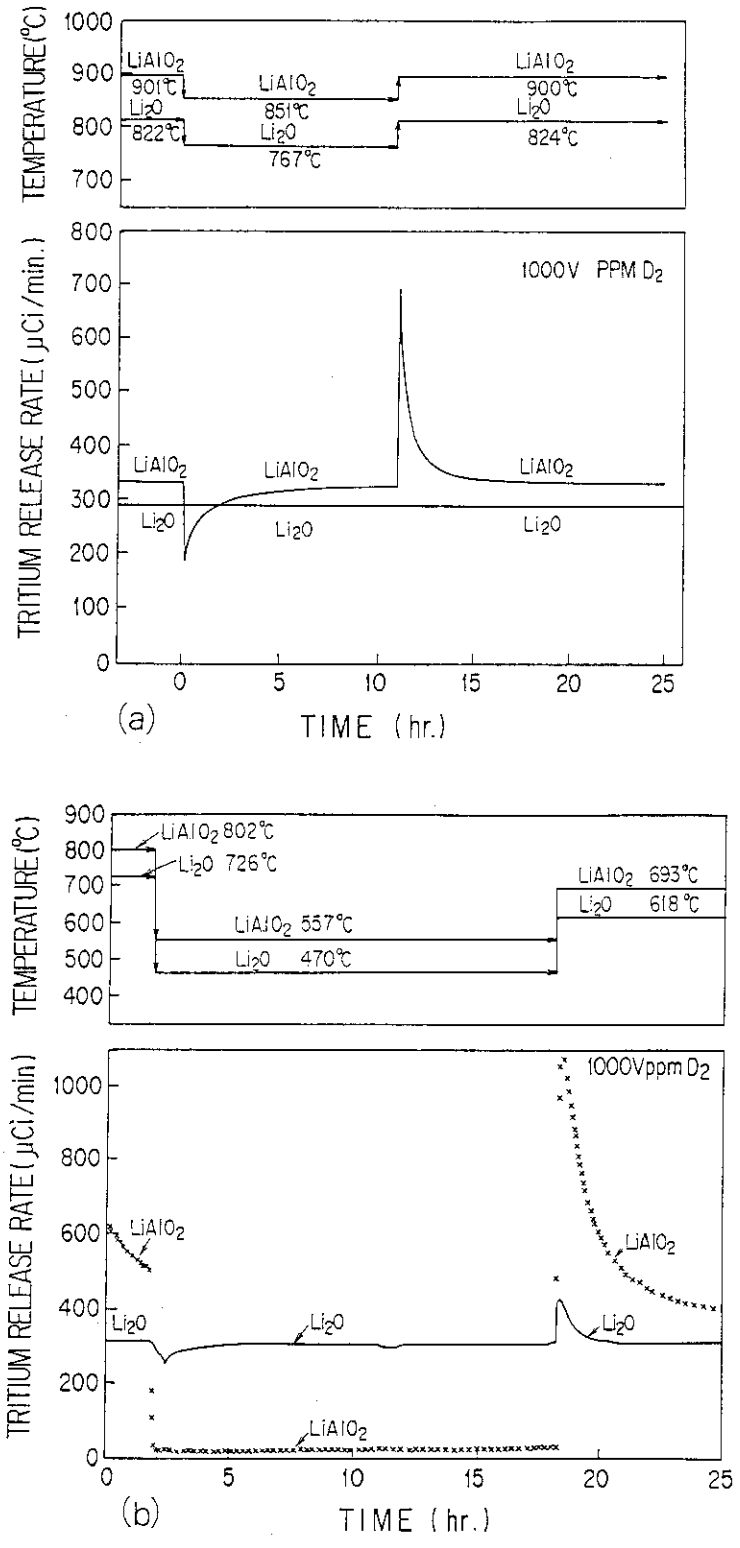

Fig. 6.2 A comparison of the effect of an incremental temperature decrease and then increase on the measured tritium release from both Li_2O and $LiAlO_2$ spheres at high temperatures(a) and at low temperatures(b) (VOM experiments)

Li_2O : natural ^6Li, 10 μm grain size, 85% T.D., 5 mm dia.

$LiAlO_2$: 26% ^6Li, 10 μm grain size, 77% T.D., 4 mm dia.

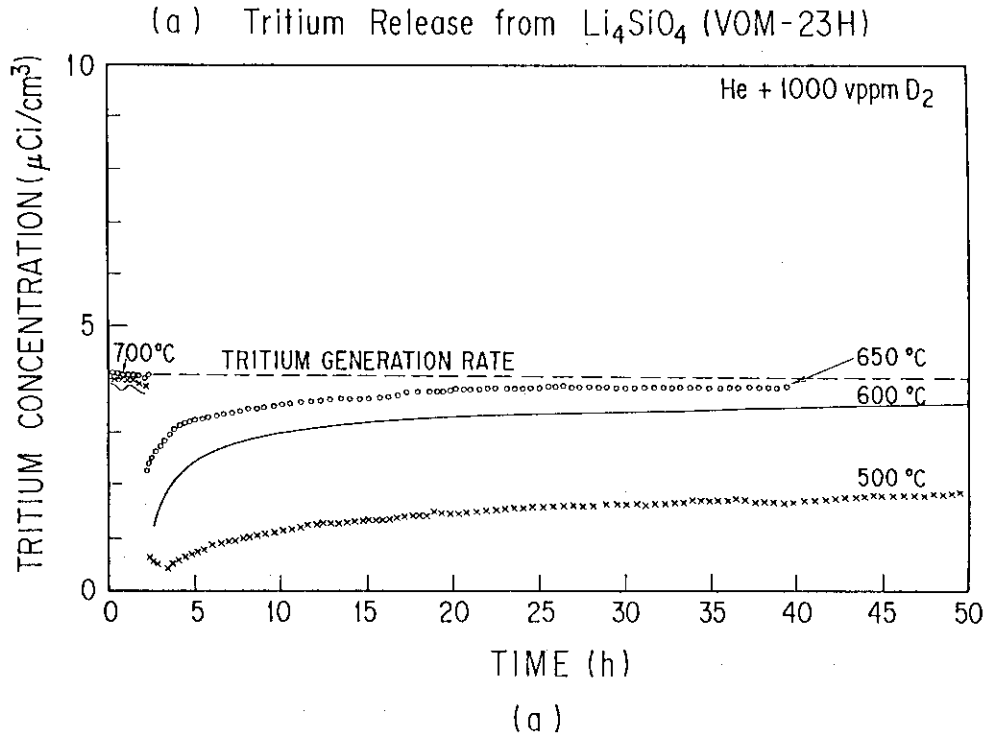

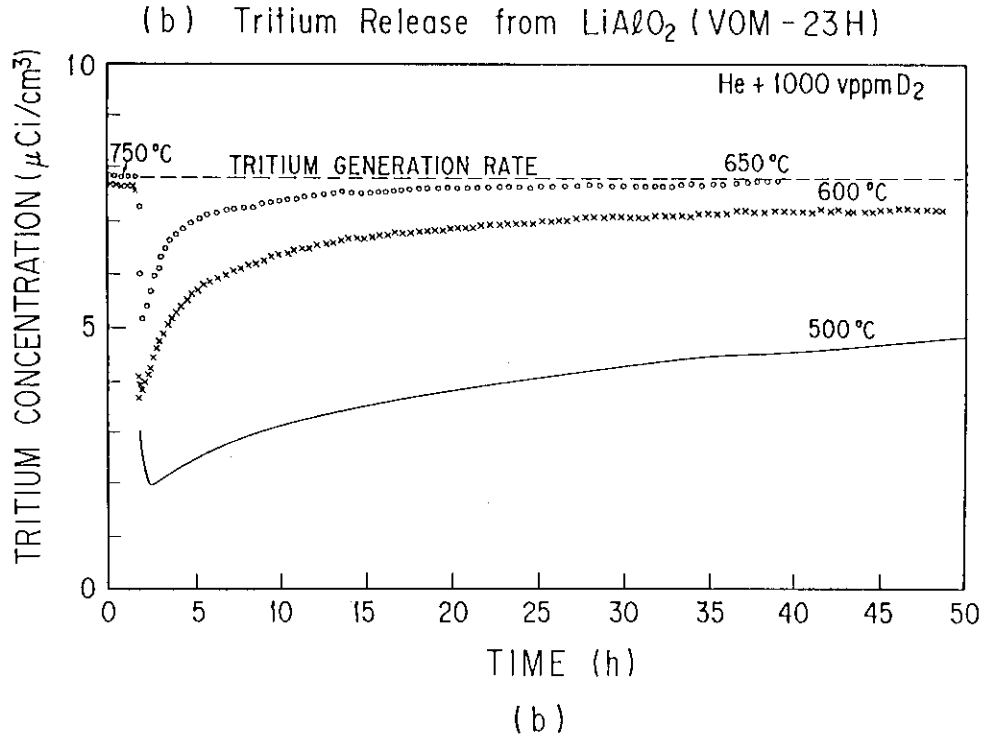

Fig. 6.3 Tritium release from Li_4SiO_4 and $LiAlO_2$ spheres (VOM experiments)
(a) Li_4SiO_4 : natural ^6Li, mean grain dia. 14 μm, 89.8% T.D., 4 mm dia.
(b) $LiAlO_2$: natural ^6Li, mean grain dia. 0.49 μm, 77.4% T.D, 3.9 mm dia.x40 mm length

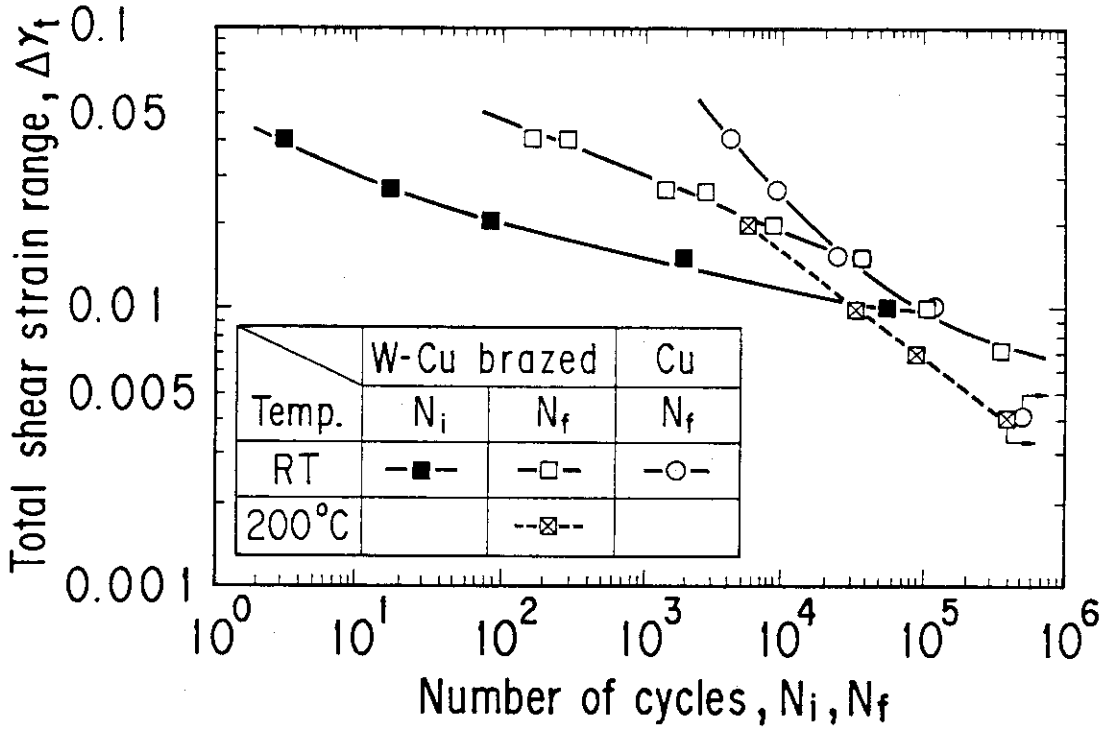

Fig. 6.4 Total shear strain range ($\Delta\gamma_t$) as a function of cycles to 1 mm crack initiation (N_i) and cycles to failure (N_f) for W-Cu brazed specimen and Copper

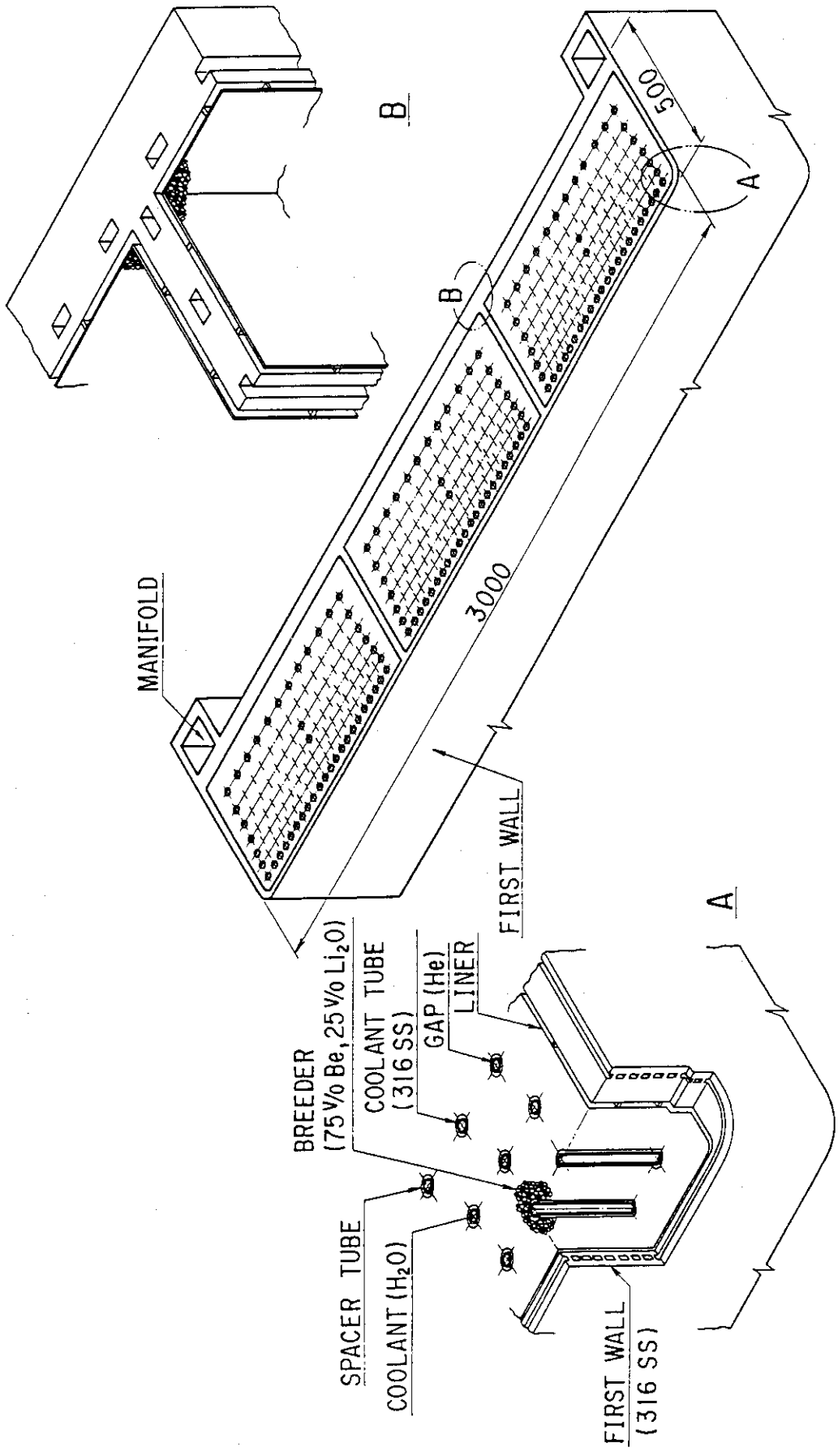

Fig. 6.5 Tritium breeding blanket ($Li_2O/Be/H_2O/AS$)

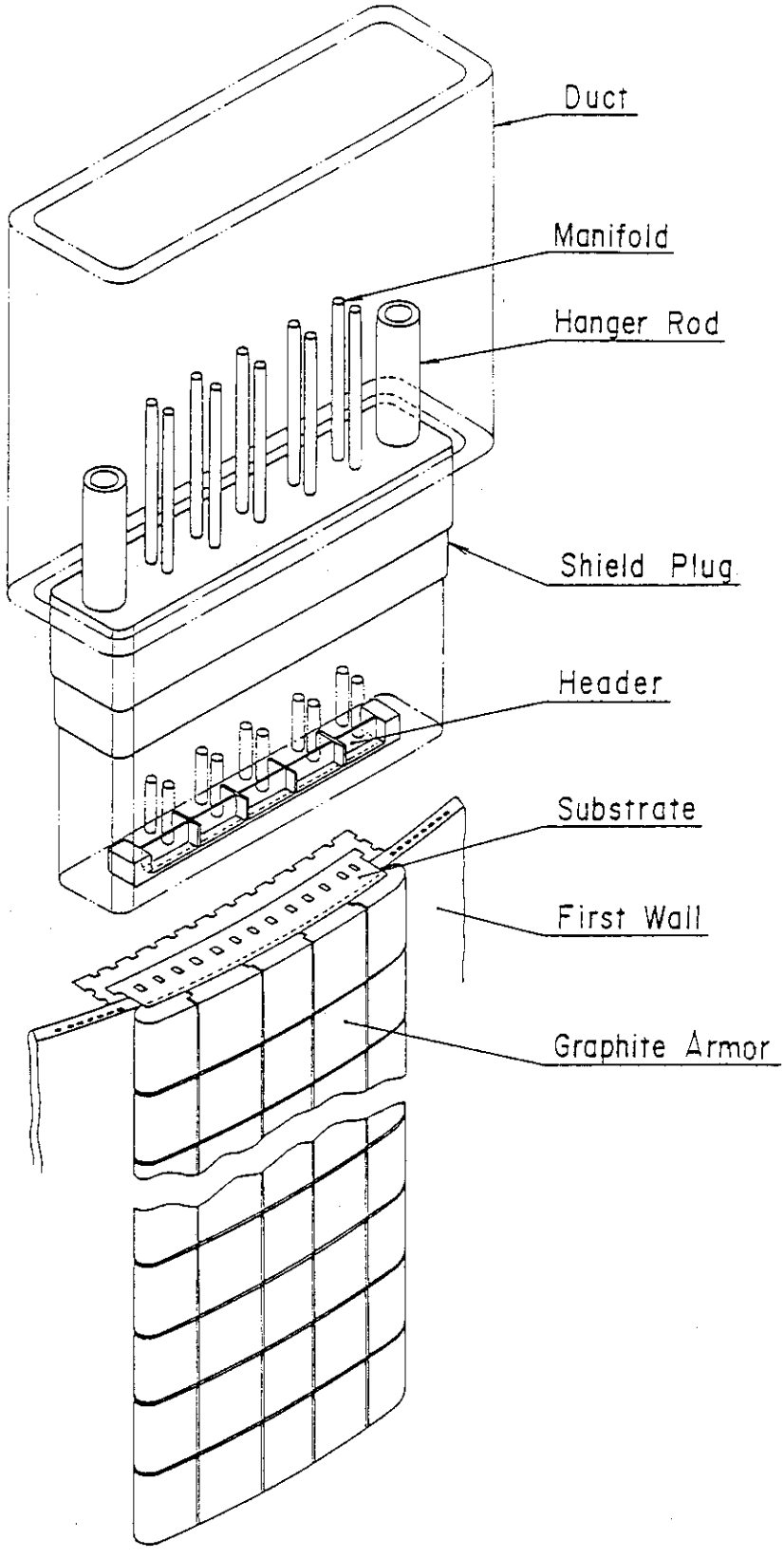

Fig. 6.6 Guard limiter concept

7. FER design philosophy

7.1 Technical and Programmatic Objectives for FER [8]

Japan Nuclear Fusion Council organized the Subcommittee on the Basic Issues of Fusion Development, August 1985. The Subcommittee studied basic principles for the nuclear fusion research and development programms in Japan after the break-even plasmas condition is achieved by JT-60. Based on the interim report worked out by the Subcommittee, it is decided that the following new subcommittees are to be set up to specify basic principles and finalize probable contents of the next step programme.

(1) Subcommittee on the Next Step Device, and

(2) Subcommittee on Fusion Reactor Technologies.

The subcommittee on the Next Step Device has studied the following points and worked out a report of it.

(1) To define options for the design concept and design specification for the next step device.

(2) To identify urgent research themes necessary for determining design specifications and specific research programme.

(3) To define feasibilities of the phased operation and probable options relating to the construction of the next step device.

(4) Appropriate cost of the next step device.

The report worked out by the Subcommittee on the Next Step Device includs issues related to technical and programmatic objectives, which touches on the followings,

(1) Reactor Relevance

(2) Overall Cost

(3) Timing and Schedule

(4) Physics/Technology/Testing Objectives

(5) Neutron Wall Loading, Fluence, Tritium Supply, and Breeding Requirement

(6) Duty Factor and Availability

(7) Supporting R&D Resources

(8) Reliability

(9) Flexibility

(10) Safety/Environment

[Reactor Relevance]

Objectives of the next step device are to accomplish missions.

(1) As reactor core technologies mission, to achieve self-ignition including burn control and long pulse burning for about 800s.

(2) As reactor technologies mission, to develop and test tritium fuel cycle, superconducting coil, remote maintenance, and breeding test module blanket.

Thus this facility aims at integration of reactor core and reactor technologies for burning plasma for the first time in the world. The development of this facility will meet most of requirements of reactor core and reactor technologies needed for demonstration reactor except part of reactor engineering tests requiring high neutron fluence.

[Overall Cost]

For getting higher efficiency of developmental investment in future, it is essential that technical risks should be coordinated and born to the maximum extent by the ordering side viewing from generic standpoint. In addition, continuous efforts should be exerted for design and research and development including;

(1) Incorporation of up-to-date databases in such an unexplored filed.

(2) Optimization of specific facility specifications in accordance with progress in research and development and results from them.

By making these major efforts, the construction cost of the next step device could be extremely reduced from early trial calculations and now it is estimated to be about ¥400 billion.

[Timing and Schedule]

The next step device is scheduled to start construction in early 1990s based on the results of JT-60 and to start operation in around the year of 2000. The next step device program for construction is divided

in several phases including basic design, detailed design, and manufacturing and construction. Conditions for whether to proceed to the next phase should be defined and the progress of the program should be managed by conducting check and review.

As far as the operation stage is concerned, in order to minimize development costs and technical risks the phased operation option stated below is to be adopted and the phase-to-phase check and review have to be sufficiently performed by experts from research institutes involved.

(1) Facility function confirmation phase (1～2years, about 5000shots), in which facility functions are confirmed whether it works sufficiently as expected by using hydrogen and deuterium plasma.
(2) Burning experiment phase (1～2years, about 1000shots), during which self-ignition is achieved by deuterium and tritium plasma and physics of burning plasma is also expected to be clarified.
(3) Full-rating operation phase (5～7years, about 12000shots), where long pulse burning for about 800sec is achieved in this phase and thereby high duty factor operation is intended.

[Physics/Technology/Testing Objectives]

Objectives of the next step device are to accomplish missions.

(1) As reactor core technologies mission, to achieve self ignition including burn control and long pulse burning for about 800s.
(2) As reactor technologies mission, to develop and test tritium fuel cycle, superconducting coil, remote maintenance, and breeding test module blanket.

Technical objectives therefore are as follows;

(1) The main physics technical objectives is to demonstrate control technologies for self-ignited ($Q \gtrsim 20$), long-burning (～800s) plasmas, such as plasma heating and current drive, impurity and particle control, plasma position and shape control, plasma power balance control.

(2) The major technology technical objectives are to demonstrate reactor technology indispensable for achieving reactorrelevant core plasmas, such as fuel cycle, safety, repair technology, superconducting coil, diagnostics and control, power sources, heating and current drive devices, and first wall.

(3) The main testings that can be implemented in the next device are fuel cycle, power generation engineering, material test, and neutronics test.

[Neutron Wall Loading, Fluence, Tritium Supply, and Breeding Requirement]

Considering present developmental status of the first wall materials, it is believed that wall loading of about $1MW/M^2$ should be used as appropriate value viewing from probable extrapolation into commercial reactor.

It has been determined as appropriate that fluence should be kept in the range of about $0.3MW/m^2$ that enables major reactor engineering tests judging from reasonable operation frequency and tritium consumption, although high fluence is not impossible to attain in the next step device. In other words, in the next step device, it is operated about 12000 times with burning time for about 800s and thereby fluence of $0.3MW/m^2$ is attained.

Tritium consumption required for this operation mode is estimated about 1.5kg per year. Among reactor engineering test, only irradiation test of structural materials is considered impracticable with this fluence of $0.3MWY/m^2$. For this items, it is decided that research and development should be carried out separately from development of the next step device.

Regarding blanket, when taking into consideration that burning time is about 800s and maximum duty factor is 0.8, it is not always easy to conduct extensive high temperature and high pressure tests of blanket used for power generation. However, compared the usefullness of conducting blanket tests within the facility with increase in associated technical development and cost, it has been determined as appropriate to carry out tritium breeding and recovery tests as well as high temperature and high pressure tests by using modular size blanket.

[Duty Factor and Availability]

To get the necessary data for the design and manufacture of breeding blankets for demonstration reactors, one at least needs to demonstrate the following performance in the next step device;

(1) Possibility of achieving a tritium breeding ratio more than unity.
(2) Continuous recovery of bred tritium.
(3) Heat removal at a temperature corresponding to conditions for an electricity generation.

The last two items are directly related to the duty factor. Taking into consideration that the burning time is around 800s, a duty factor of 0.8 is at least required to conduct extensive high-temperature and high-pressure tests in the next step device for simulating demonstration proto-type blankets.

The fluence of about 0.3MWY/m^2, selected for the next step device as a compromise between engineering test requirements and tritium procurement, is not so demanding. A rather small average availability of about 10% for several years is imposed, because of external tritium procurement. Operation with availability of 100% for several days is, however, planned for blanket engineering tests.

[Supporting R&D Resources]

In the area of reactor core technology, the following items are regarded as important.

(1) Confirmation of energy confinement scalings
(2) Selection of current drive method such as plasma current ramp-up
(3) Characteristics comparison and improvement of heating methods

In the area of reactor technologies, the following trial manufacture and development are regarded as important.

(1) Development of large-size, large current and intensive magnetic field superconducting magnet

(2) Development of tritium handling of kg/day class
(3) Development of blanket
(4) Development of highly efficient current drive and heating device
(5) Development of remote maintenance technology for reactor structures
(6) Development of high temperature flux resistant equipment for the first wall, etc.

[Reliability]

The key fusion reactor components in the next step device are high heat flux components, heating and currnt drive devices, fuel injectors, vacuum pumps, shielding, TF, PF and position control coils and fuel circulation systems, etc.. Generally, their reliability should be tested in a fusion reactor enviroment for fairly long time in order to provide basic data base which enables extrapolation to longer use ($\sim$10 years, or several MWY/m^2) in the following demonstration reactor.

Some of the above components are not easy to be replaced when they fail. Those components, such as TF coils, lower PF coils, a part of coil shielding and probably position control coils, are not likely to be designed replaceable in the next step device for economical reasons. Then high reliability is required for those components, and it may be reasonable that those components are manufactured with high reliability and expected to show their performance during the reactor lifetime to avoid large additional complexity, cost increase and technical risks of the plant, caused by easy replaceable scheme. Principally, those components can be replaced, if they would fail, although it takes longer time.

[Flexibility]

The next step device will need several years for its design and construction. The design drivers and constraints with moderate extrapolations naturally have large uncertainties, and there are also uncertainties even in the present data bases. During the period of design and construction, technologies will be developed evolutionarily and

sometimes revolutionarily. The next step device has to manage those situations at the operation stages, although there are some possibilities to change design during construction. In this context, how flexibly the next step device adjust to unknown situations is very important.

[Safety/Environment]

It is the most important for the next step device to be accepted by the public from the environmental point of view and to assure personnel's safety during normal and maintenance operation. The next step device is expected to be built in Naka site, JAERI. The following design conditions are foreseen;

(1) Distance to the site boundary : ~400m,

(2) Water supply : 17000ton/day is planned,

(3) Capacity of radioactive drain : 4000ton/day is planned,

(4) Design guide value for tritium release rate,

normal operation : 100Ci/day

7.2 Physics "design-driving" features and constraints [18]

The major physics design philosophy is described which is the essential base for the plasma design and has also significant influences on a reactor design concept. The design philosophy can be divided into two classes, design drivers (main physics features diving design concept) and physics design constraints. The design driver is a feature that a designer is free to choose. This choice may be guided by his opinion as to feasibility or drivability, but nevertheless he is free to make a choice. For example, to choose an ignited plasma is a design driver. On the other hand, the design constraint is a physical law and a designer is not free to choose whether or not to follow it. For the above example of ignition as a design driver, the enegy confinement scaling law is a design constraint.

The following twelve physics design drivers have been chosen for the FER plasma design.

DP 1 Fusion performance (Energy multiplication rate, Q)
DP 2 Burn pulse length
DP 3 Operation scenario
DP 4 Impurity and particle control method
DP 5 Plasma configuration
DP 6 Start-up assist
DP 7 Plasma heating methods
DP 8 Frequency of major disruptions
DP 9 Burn temperature control
DP10 Toroidal field ripple
DP11 Maximum impurity level
DP12 Fast α-particle confinement

We describe our choices for the above design drivers.

We have picked up the following sixteen physics design constraints for ths FER plasma design.

CP 1 Plasma confinement
CP 2 β-limit
CP 3 β_{total}/β_{DT}
CP 4 q-limit

CP 5 n-limit

CP 6 Fusion power density

CP 7 Plasma temperature

CP 8 Inductive loop voltage

CP 9 Plasma edge and scrape-off conditions

CP10 Impurity release and erosion rate

CP11 Disruption scenario

CP12 Particle exhaust and fuelling requirements

CP13 Power deposition efficiency and profile

CP14 Current drive efficiency and profiles

CP15 Parameter ranges for heating and current drive

CP16 Plasma heating power flow

The guidelines, which should be followed by a plasma designer, are stated for first eight design constraints for the FER plasma design.

DP 1 Fusion performance (Energy multiplication rate, Q)

[Choice for FER]

$Q \gtrsim (20\text{-}30)$

DP 2 Burn pulse length

[Choice for FER]

Around 800s

DP 3 Operation scenario

[Choice for FER]

Scenario is a pulse operation using a hybrid of inductive and non-inductive current drive. Plasma current is sustained inductively at a stage of burning, and plasma current is ramped up mainly by a non-inductive current drive method.

DP 4 Impurity and particle control method

[Choice for FER]

Poloidal divertor with single null.

DP 5 Plasma configuration

[Choice for FER]

Plasma shape is defined by a magnetic surface having a 95%

flux. Its elongation and triangularity are κ=1.7 and δ=0.2, respectively. The outermost surface dividing a main plasma from scrape-off plasma has a single magnetic-null point.

DP 6 Start-up assist

[Choice for FER]

Electron cyclotron wave of its power 3MW is used at the initiation stage of operation for pre-ionization and pre-heating of plasmas. The ordinary mode with the frequency of fundamental harmonic will be launched from a low toroidal field side.

DP 7 Plasma heating methods

[Choice for FER]

Many options are now being deliberated and a final selection seems too early. Typical options are as follows;

(1) Ion cyclotron wave, especially 2nd harmonic for deuterium, in addition to lower hybrid wave for current drive,

(2) Neutral beam with its energy range 250-500keV, which is used for heating and current drive.

DP 8 Frequency of major disruptions

[Choice for FER]

5% for 1st and 2nd operation phase and 1% for 3rd operation phase.

DP 9 Burn temperature control

[Choice for FER]

Not specified.

DP10 Toroidal field ripple

[Choice for FER]

0.75% at plasma edge.

DP11 Maximum impurity level

[Choice for FER]

Effective ionic charge, Z_{eff}=1.5, at burning stage. At a startup stage impurity level will be increased and Z_{eff} depends on

operation scenario and current drive options.

DP12 Fast α-particle confinement

[Choice for FER]

Power loss due to direct fast α-particle loss should be limited less than 10% of α-heating power.

CP 1 Plasma confinement

[Guideline for FER]

Mirnov-type scaling law for global energy confinement time, $\tau_E^{Global}[s] = 0.155a[m]I_p[MA]\kappa$, is applied to zero-dimensional power balance anlyses with an ignition margin of unity, where κ is plasma elongation.

CP 2 β-limit

[Guideline for FER]

Troyon-type scaling, $\beta[\%] = 3.5I_p[MA]/a[m]B_T[T]$, is used for the limit of averaged toroidal beta value.

CP 3 β_{total}/β_{DT}

[Guideline for FER]

Total beta value consists of contributions from electrons, fuel D/T ions, impurity ions, thermal helium ions, fast α-particles, and fast neutral beam particles. The typical concentration for ions is assumed as follows: 46.5% for deuterium and for tritium, 5% for thermal helium, 1% for hydrogen, 0.5% for carbon and for oxygen. Those percentages result in Z_{eff}=1.5. The fast α-particle contribution is estimated by an enhancement factor, (1.0 + (0.015T[keV] - 0.05)) in a temperature range, 7keV$\lesssim$ T$\lesssim$30keV. The fast neutral beam contribution can be calculated from an orbit following Monte-Carlo code or an analytical solution of Fokker-Planck equation.

CP 4 q-limit

[Guideline for FER]

q =2.6-2.8 is selected for MHD safety factor.

CP 5 n-limit

[Guideline for FER]

The n-limit is not thought to be a strong constraint in FER plasma design. Namely, plasma is designed without the density constraint, and the resultant density is checked by the present database, e.g., $\bar{n}_{e,max}[10^{20}m^{-3}]=1.5B_T[T]/R[m]$ during a burning stage.

CP 6 Fusion power density

[Guideline for FER]

Fusion power is calculated from a formula, $1.5\bar{n}_D\bar{n}_T\langle\sigma v\rangle E_f$, where a numerical factor 1.5 reflects the effect of profiles of density and temperature, which are expected to be rather flat and rather round like parabolic, respectively.

CP 7 Plasma temperature

[Guideline for FER]

$\bar{T}$[keV]/a[m] could be limited to less than 20.

CP 8 Inductive loop voltage

[Giudeline for FER]

Spitzer's formula is used for plasma resistivity.

7.3 Engineering "design-driving" features and constraints[19]

The major engineering design philosophy is descrived which is the essential base for the engineering design and has also significant influences on a reactor design concept. The engineering philosophy can be also divided into two classes, design drivers (main engineering features driving design concept), and engineering design constraints, such as are for physics design. For example, to choose a reactor structure is a design driver. On the other hand, the material strength is a design constraint.

The following twelve engineering drivers have been chosen for the FER engineering design.

DE- 1 Plasma configuration
DE- 2 Tritium breeding
DE- 3 Lifetime fluence
DE- 4 Neutron wall loading
DE- 5 Operation scenario
DE- 6 Inductive or non-inductive current drive
DE- 7 PF coil location
DE- 8 Support of TF coil
DE- 9 Maintenance
DE-10 Vacuum boundary
DE-11 Modularization
DE-12 Shield material

We descrive our choices for the above design drivers.

We have picked up the following sixteen engineering constraints for the FER engineering design.

CE- 1 Plasma initiation
CE- 2 Cryostat
CE- 3 RF and NBI system
CE- 4 TF coil
CE- 5 PF coil
CE- 6 Control system of positional instability
CE- 7 Toroidal field ripple
CE- 8 Thickness of components
CE- 9 Gap distance

CE-10 Auxiliary system requirements

CE-11 Component replaceability

CE-12 First wall

CE-13 Shield

Ce-14 Divertor

CE-15 Tritium system

CE-16 Vacuum system

The guidelines, which should be followed by an engineering designer, are stated on the major design constraints for FER engineering design.

7.3.1 Major engineering "design-driving" features chosen for FER

DE- 1 Plasma configuration

[Choice for FER]

1. Divertor : Single null
2. Elongation : 1.7
3. Triangurarity : 0.2-0.3

These are also our choices from physics.

DE- 2 Tritium breeding

1. TBR=0
2. Tritium breeding and extruction test using low/high temperature test module.

DE- 3 Lifetime fluence

[Choice for FER]

0.3 MWY/m2

DE-2, and DE-3 are the programatic decisiion for FER.

DE- 4 Neutron wall loading

[Choice for FER]

1 MW/m2

DE- 5 Operation scenario

[Choice for FER]

1. 1.2 x 10^4 D-T shots during 5-6 years for Phase 3.
2. 0.8 of duty factor capability.

DE- 6 Inductive or non-inductive current drive

[Choice for FER]

Non-inductive current ramp up.

DE- 7 PF coil location

[Choice for FER]

1. External to TF coil for SC coils.
2. Inside TF coil and outside shield structure for active stabilization coils.

DE- 8 Support of TF coil

[Choice for FER]

Centripetal force of TF coil is supported with a bucking cylinder outside the OH solenoid coils.

DE- 9 Maintenance

[Choice for FER]

1. Component replaceability

   Replaceable ; Divertor module, Outboard shield, Guard limiter.

   Semi-permanent; TF/PF/Active control coils, Cryostat, Inboard shield.

2. Access to torus

   Horizontal

3. Personnel access or remote handling

   Remote handling with personnel access caapability.

4. Containment of tritium and active dust

   Container with cooling equipment.

DE-10 Vacuum boundary

[Choice for FER]

Combined boundary for the plasma and coil chamber.

DE-11 Modularizastion

[Choice for FER]

1. Number of TF coils 12
2. Number of shields 12
3. Number of divertor plates 12

DE-12 Shield materials

[Choice for FER]

Stainless steel of 316 type for the inboard shield.

7.3.2 Major engineering "design-driving" constraints for FER

CE- 1 Plasma initiation

[Guideline for FER]

1. Break-down voltage : 10 V for 1 s
2. Troidal resistance : > 30 micron ohm

CE- 2 Cryostat

[Guideline for FER]

Maximum vacuum pressure: < 1.3 mPa (10^{-5} Torr)

CE- 3 RF and NBI system

[Guideline for FER]

		RF system		NB system
	Heating	Startup	Cur.drive	(with ECRH)
1. Type	ICRF	ECRH	LHRF	0.5MeV NB
2. Bays required	1	1	1	3
3. Overall system efficiency	0.43	0.13	0.2	
4. Power density (MW/m2)	< 10	< 5	< 10	20-40

CE- 4 TF coil

[Guideline for FER]

[1] Conductor design

1. Type of superconductor : $(NbTi)_3Sn$, Forced flow cooling
2. Maximum magnetic field : < 12 T
3. Current density of winding: < 35 A/mm2

[2] Structural design

Allowable stress, Sm : < 600 MPa

CE- 5 PF coil

[Guideline for FER]

1. Type of superconductor : $(NbTi)_3Sn$, Forced flow cooling
2. Maximum magnetic field : < 12 T
3. Current density of winding: < 30 A/mm2
4. Field ramp-up rate : < 10 T/s

CE- 6 Control system of positional instability

[Guideline for FER]

1. Passive conducting material close to plasma	:	Cu
2. Active coil needed inside TF coil	:	Yes
3. Growth time of vertical instability	:	> 50 ms
4. Location of active coils	:	Inside TF coil, and outside shield structure
5. Penetration time of control field	:	< 50 ms

CE- 7 Toroidal field ripple

[Guideline for FER]

1. Field ripple (at plasma edge)	:	0.75 %
2. Alpha loss	:	Max. first wall heat load (<0.4 MW/m2)

CE- 8 Thickness of components

CE- 9 Gap distance

[Guideline for FER]

The design conditions on these items are summarized in two figures, Fig. 7.1 FER radial build, and Fig. 7.2 FER vertical build.

CE-10 Auxiliary system requirement

[Guideline for FER]

Bay occupation

ICRH	20 MW	1
LHRF	20 MW	1
ECRH	3 MW	1
Test module		4
Inspection		2
Diagnotics and I & C		2
Fueling		1
(Total)		(12)

CE-11 Component replaceability

[Guideline for FER]

1. The largest size component: movable shield
   6.5L x 3W x 5H m, 250 tons
2. Maintenance access port size: 3W x 6H m

CE-12 First wall

[Guideline for FER]

1. Structural material	:	Annealed SS 316
2. Surface material	:	Graphite or C/C composite
3. Allowable stress	:	ASME or crack propagation analyses
4. Allowable temperature	:	350 deg. C for SS 316
		1800 deg. C for graphite or C/C composite
5. Peak surface heat flux	:	0.4 MW/m2
6. Baking temperature	:	150 deg. C

CE-13 Shield

[Guideline for FER]

1. Biological shield requirement : 2.5 mrem/h one day after shutdown
2. Coil shield requirement

Dose limit of TF coil Insulator:	$< 3 \times 10^{9}$	rad
Max. neutron fluence	: $< 2 \times 10^{18}$	n/cm2
Cu radiation damage	: $< 4 \times 10^{-4}$	dpa
Max. nuclear heat of TF coil	: < 3	mW/cc
Total nuclear heat in TF coil	: < 35	kW

CE-14 Divertor

[Guideline for FER]

Peak surface heat flux on inclined target plate: < 2 MW/m2

DE-16 Vacuum system

[Guideline for FER]

Number of ports	: 12
Size of ports	: 0.8 x 0.8 m/port
Detonation limit	: < H_2 12 torr

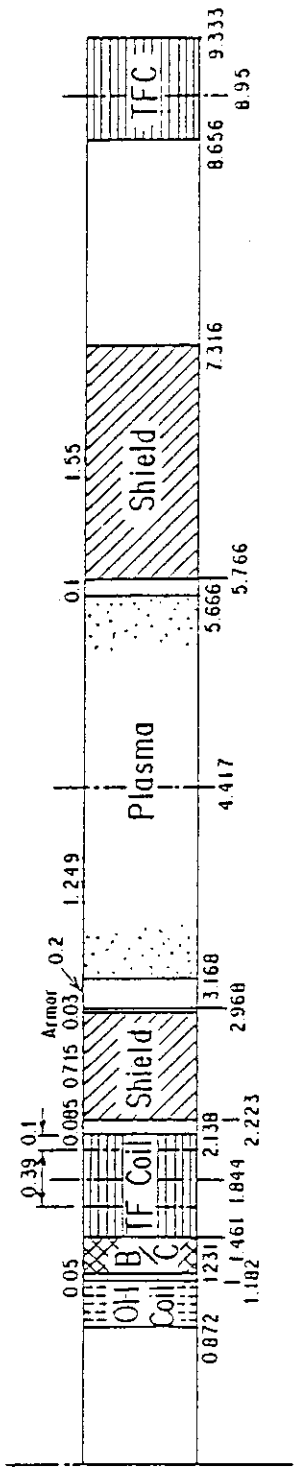

Fig. 7.1 FER radial build

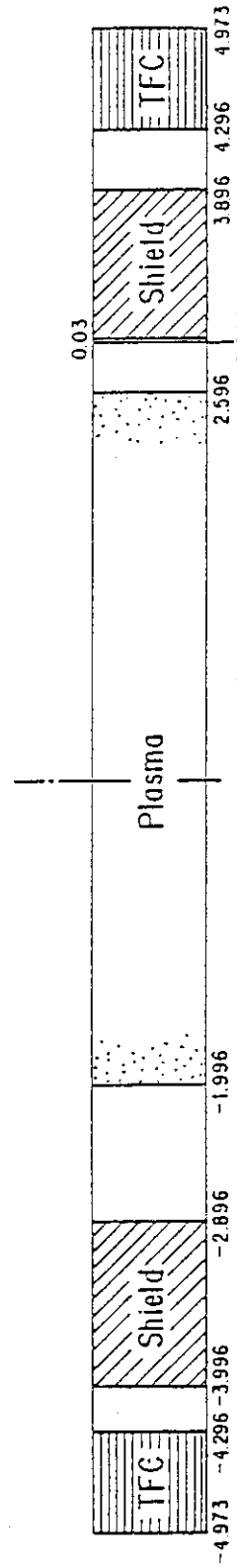

Fig. 7.2 FER vertical build

8. Operational flexibility

8.1 Introduction

In designing the next generation machine like FER and INTOR, which can achieve their missions, with consideration of cost-effectiveness, we must take into account of the uncertainties of the physics assumptions. In principle, these uncertainties should be minimized at the start of construction with the extensive research studies on JT-60, JFT-2M and other devices of the world, at least for the behaviour of hydrogen plasmas. However, there might possibly still exist some uncertainties due mainly to the programatic schedule of FER. In addition, we must consider the possible large uncertainties of the DT burning plasma, which cannot be removed in the existing devices. In this context, the device will become fairly attractive if it has large flexibilities in various ways to ensure the achievement of the missions.

In this report, we will first examine the possible expected uncertainties of the physics assumptions, and then study the feasibility to provide the device with the flexibility to cope with these uncertainties. We will also examine the flexibility for the future possible advanced operation to make the device more attractive.

8.2 Requirements for device flexibility and typical scenarios

There are two categories of requirment for the device flexibility. One is for achieving the primary missions (mainly refered to ignition) of the device, and another one is for the advanced purposes after having achieved the primary missions. The major reason for the first requirement is that the uncertainty of physics data base will still remain, especially concerning the DT burning, even when construction and machine operation starts, since the full DT burning will be done at the first time in FER or INTOR. Expected possible uncertainties are summarized in Table 8.1. In this table, major items of physics assumptions for the design are listed on the left column. In other words, they are research items of FER or INTOR. Possible uncertainties are listed on the medium column. Double circle and star denote the uncertainty with achieving the primary missions, and with the advanced

operatios, respectively. Requirements of flexibilities for each uncertainty are listed on right column.

Major reason for the second requirement is that the device will become more attractive, if it has the potential to achieve more advanced purposes by altering the device with the additional investment, after having achieved the primary missions. Examples of these advanced purposes include high beta and steady state operations in physics area, and high fluence operation in engineering area.

Based on the summary in Table 8.1, we have prepared the following flexibility scenarios to cope with the expected possible uncertainties.

(1) Plasma size enlargement scenario to maximize the plasma size by decreasing or improving the shield and altering the divertor structure.

(2) Plasma shape flexibility scenario for the operations with a variety of plasma shape, e.g., high triangular shape double null configuration, limiter operation.

(3) Heating/Current drive/Control system flexibility scenario to provide flexible machine structure, which enables replacement and/or addition of various heating/current drive/control system, even after DT operation.

(4) Impurity control system flexibility scenario for the modification of divertor structure (e.g., long divertor throat, closed divertor structure), and replacement of wall and divertor plate materials.

(5) Advanced operation scenario to provide the flexibility for future possible advanced operation scenario, such as high beta, high neutron wall loading, high heat flux operation, steady state operation, and high fluence operation.

8.3 Sensitivity studies

Before proceeding to the detailed studies of each scenario, we have made sensitivity studies to examine the effect of size enlargement on ignition margin. The effects of the reduction of inboard (Δa_{in}), outboard (Δa_{out}), upper and lower (Δb) shield are shown in Fig.8.1. In this study, standard FER scaling law (Mirnov type)[18] is assumed and other geometrical parameters are fixed to FER reference reactor (option ACS) parameters[19]. Safety factor q_φ is fixed, so the plasma current is changed according to the alteration of the device geometry. It is seen from this figure that the effect of Δa_{in}

and Δb are remarkable, while no increase of ignition margin is obtained with Δa_{out}. In Fig.8.2, the effect of the increase of ellipticity (κ), triangularity (δ), magnetic field on axis (B_T) and Troyon coefficient (C_β) on the ignition margin I_g are shown.

8.4 Plasma size enlargement scenario

According to the sensitivity studies in the previous section, enlargement of plasma size by reducing the shield thickness of inboard and lower/upper shield and by altering the divertor into thin flat structure is fairly effective to increase the ignition margin. To reduce the shield thickness, stainless steel shield must be replaced by some other material, which has an equivalent shielding capability with thinner thickness, to satisfy the design criteria for toroidal coils. Here, as an example, the inboard shield is reduced by 10 cm and upper shield by 20 cm, by replacing each movable shield with tungsten shield. The divertor plate is also assumed to be replaced with thin flat type plate, which results in lowering the null point by 40 cm. The outboard shield is retracted by 25 cm only to keep the elongation to 1.7. The resultant plasma parameters and ignition margin for typical scaling laws are listed in Tables 8.2 and 8.3, respectively. Ignition margin is increased up to 1.5 based on the reference scaling law (Mirnov type). Figures 8.3 shows the operation space of plasma current I_p and supplied volt-second to the plasma Ψ for this size enlarged plasma. Solid and dotted lines denote the limiting lines due to the maximum field (10 T for solenoid coils and 12 T for divertor coils) of each coil for high beta and low beta plasma, respectively. Coil numbers are labeled by square and their locations are shown in Fig.8.4. Note that the limiting lines of enlarged plasma move from those of reference plasma, particularly, line of No.15 coil (divertor coil) moves upward, since the null point approaches to the coil in this case. In addition, line of No.10 coil (solenoid coil) moves downward due to the cancelling effect by equilibrium field component. Mainly these two effects widen the operation space and compensate the increase of plasma current to some extent, and 200~300 seconds of burn time is still available in this enlarged plasma, if the plasma current can be ramped-up to 11.5 MA. Configuration of the enlarged plasma is shown in Fig.8.5.

Several contrivances must be considered for this alteration of the

reactor core component. One possible method is that the inner and upper shield are combined into L-type structure, which can be removed and replaced with tungsten shield. As for divertor plate, it must be replaced with thinner flat type structure as shown in Fig.8.5. In addition, the outboard shield is retracted with use of the extra shield and spacer.

Application of this size enlargement scenario needs careful examination. Alteration of the reactor core structure, which is highly activated, is quite cumbersome task, and require considerable extra cost for tungsten shield. Thus, careful assessment for the ambiguity of physics data base should be made in, at least, two steps. The first step is at the start of construction. If the confinement scaling law and other physics data base have been sufficiently established in the existing devices by then, the construction will be started based on these data bases to realize the required device size. Even in this case, the capability for the flexibility of size enlargement scenario should be included, since the uncertainty under full DT burning condition should still remain. The second step is at the start of DT burning. During the initial hydrogen discharge phase, confinement scaling laws and other physics assumptions should be examined carefully, and the decision should be made on the plasma size in DT burning phase. If the experiments in hydrogen discharge phase are confirmed to be well described by the physics assumptions used in designing the device and the ambiguity of DT burning plasma is not expected to be so large, then DT operation will be started with the reference plasma size and the size enlargement scenario may be used for the contingency of the possible ambiguity with DT burning. When the expected plasma performance is not attained in hydrogen discharge, though such a situation should not be encountered, in principle, with a careful assessment of the physics data base at the construction start, size enlargement will be provided from the beginning of DT operation. With these procedure or phased operation and construction, difficulty in replacing and handling the highly activated component should be minimized and the cost could be saved if the physics assumptions hold as expected.

8.5 Plasma shape flexibility scenario

In this flexibility scenario, the degree of plasma shaping, such as elongation, triangularity, is increased and different configuration, such as

double null divertor and limiter configuration, will be employed to increase the ignition margin or to operate with a different shaping plasma.

8.6 Heating, Current drive, Control systems flexibility scenario

Major items of this flexibility scenario include the flexible structure for using a variety of heating/current drive/control systems, and the back-up scenario for non-inductive current ramp-up. As for the first item, critical point is to use and replace tangential neutral beam injector and RF systems at any phase of the machine operation. As a matter of course, the decision of the methods for heating and current drive system needs a careful assessment of the data base at the start of construction and DT operation in the same context of the size enlargement scenario. Example of simultaneous installation of tangential NBI and RF systems into the reference ACS reactor is shown in Fig.8.6. Several contrivances in desin phase are necessary for this purpose. They include the removal of triangular post (this is also necessary for the size enlargement scenario), measure for the suppression of neutron streaming into water tank type shield due to the removal of the triangular post, and shape of outer shield modules.

As for the second item, two back-up scenarios are considered. One is reinforcement of LH power by increasing the number of LH port. This scenario is included in the category of the first item. Another is the modification of operation scenario. Figure 8.7 shows this example. In this figure, path (A) shows the reference operation scenario, where plasma current is ramped-up to 8.7 MA non-inductively and subsequently inductive burning starts. Path (B) shows an example of back-up scenario for non-inductive current ramp-up, where plasma current is ramped up to about 4 MA non-inductively, and subsequently ramped-up to 8.7 MA inductively. With this scenario, 100~150 seconds of burn time is still available, where we have assumed Spitzer resistivity and Neo-Alcator confinement scaling during the inductive current ramp-up phase. Path (C) is the full inductive operation, where 16 seconds flat top with 4 MA can be available. Plasma current could be ramped-up to 6 MA inductively, while no flat top is available in this case. This full inductive operation scenario will be useful for the initial cleaning up and aging of the plasma facing component and RF launcher, and so on.

8.7 Advanced operation scenario

Major purposes of this scenario are to provide the test bed for the demonstration of advanced physics, such as high beta, steady state operation and to provide the higher potential for engineering testing by, for example, high fluence operation, though they are not included in the primary missions for FER. Here, we will examine higher fluence operation ($\sim 1 MW \cdot Y/m^2$) as an example.

It is expected that the tritium procurement will be primary obstacle for this higher fluence operation. Then, it will be required to install tritium breeding blanket as much as possible. We assume that breeding blanket of 30 cm thickness with tungsten shield in the inboard region of the improved ACS reference reactor. Resultant device parameters are $a = 1.2\,m$, $R = 4.6\,m$, $B = 5\,T$, $I_p = 7.7\,MA$. Operation of this small plasma must inevitably be driven mode of operation. Figure 8.8 shows the feature of this mode of operation. Solid line shows Q value as a function of temperature, in which upper curve is evaluated with reference FER scaling (Mirnov type) and the lower curve with degraded scaling by a factor of 1.5. Dashed lines denote the required heating power for these operations. If the plasma current is fully driven non-inductively, required current drive power is shown by solid-dashed line, where current drive efficiency $\eta = n_{20}RI/P = 0.3$ was assumed. This value of the efficiency is the best data so far obtained in JT-60. Power balance is achieved at the temperature, where the line crosses with the dashed lines P_{in}. At this temperature, attained Q value is evaluated to be 3~4 both for reference and degraded confinement cases. In the case of full inductive operation, increasing the plasma temperature will be beneficial to a higher fluence with smaller shot number. As shown in Fig.8.9, neutron wall loading P_w decreases with temperature, while the burn time increases more rapidly, and consequently available fluence Φ during one shot of the burn increases.

8.8 Conclusions

Physics uncertainties and correspondingly required device and operational flexibilities in DT burning phase are reviewed. Based on the review, several typical flexibility scenarios have been chosen and studied in detail. They are (1) Plasma size enlargement scenario, (2) Plasma shape

flexibility scenario, (3) Heating/Current drive/Control system flexibility scenario, (4) Impurity control system flexibility scenario and (5) Advanced operation scenario. All of the scenarios have been shown to be practicable and to enhance the device performance considerably. As for the size enlargement scenario, alteration of the reactor core component may require considerable cost, so total cost may exceed that of the larger device, which is designed to have larger ignition margin from the beginning. However, if the reference ACS reactor could ignite, no such alteration is necessary and total cost could surely be saved. Trade-off study for risk and cost-saving is necessary to establish the final flexibility scenarios. Also careful assessment of the physics data base is necessary at the start of construction and DT operation to decide which flexibility scenarios we should include into the device.

Table 8.1 Major uncertainties on physics assumptions and corresponding required flexibilities

Physics assumptions (Research items for FER)	Uncertainties	Required flexibilities
(1) Confinement (·energy confinement, ·beta scaling)	◎ Confinement scaling in DT burning plasma ◎ Beta scaling in DT burning plasma	· Increasing plasma size, current, magnetic field by additional expense or innovations
(2) Heating and Current Drive	◎ Optimum heating methods to DT burning state ◎ Non-inductive current ramp-up to large plasma current ☆ Optimum non-inductive current drive scheme in burning plasma	· Replacement/addition of heating and current drive systems
(3) Plasma Control ① Plasma shape, magnetic field configuration	◎ Optimum shape and field configuration to obtain optimum plasma performance in burning plasma	· Operation capability with a variety of plasma shapes and field configurations
② Burn Control	◎ Optimum burn control scheme	· Replacement/addition of all sorts of control system, especially heating/current drive system
③ Stability Control (disruption, MHD activity, profile control)	◎ Optimum control schemes for each instability in burning plasma	· same as above
④ Impurity Control and Ash Exhaust	◎ Optimum divertor configuration and divertor/wall materials in burning phase	· Alteration of divertor structure and replacement of divertor/wall materials

Table 8.2 Major device and plasma parameters of enlarged plasma

Major radius	R	(m)	4.5
Minor radius	a	(m)	1.43
Field on axis	B	(T)	4.53
Plasma current	I_p	(MA)	11.5
Elongation	κ		1.7
Fusion power	P_f	(MW)	635

Table 8.3 Ignition margin I_g, confinement time τ_E and Q value for various scaling laws of enlarged plasma

Scaling	τ_E	I_g	Q
FER Reference (Mirnov type)	3.30	1.51	∞
ASDEX-H	5.30	2.13	∞
JAERI-Optimized	2.21	1.29	∞
KG-H	2.25	1.11	∞
KG-L	0.64	0.35	2.75
JAERI L-mode	0.30	0.17	1.04

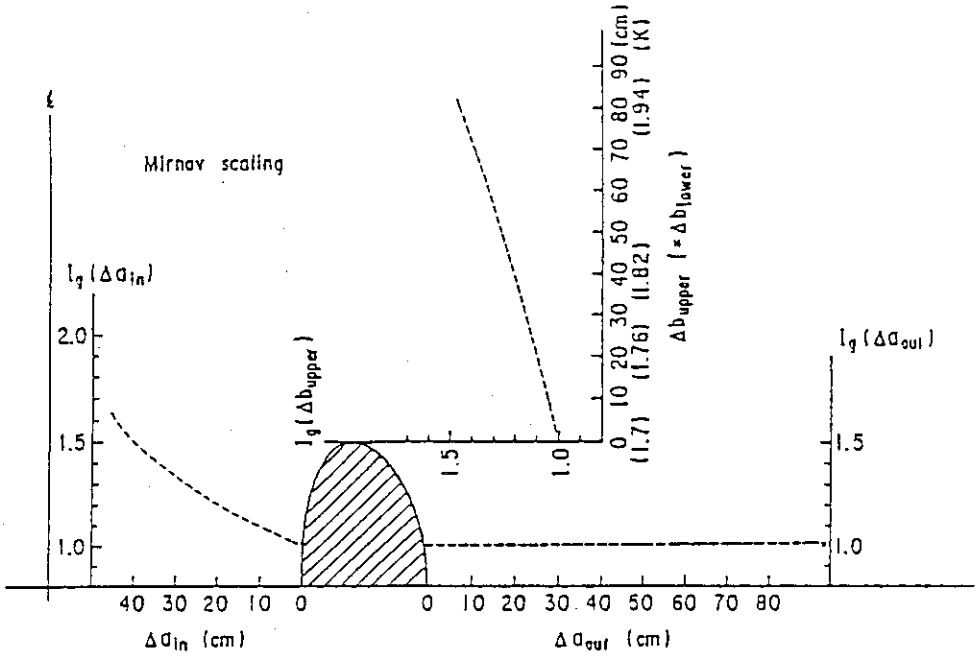

Fig. 8.1 Sensitivity for increase of ignition margin with respect to the reduction or retraction of the inboard (Δa_{in}), outboard (Δa_{out}) and lower/upper (Δb) shield.

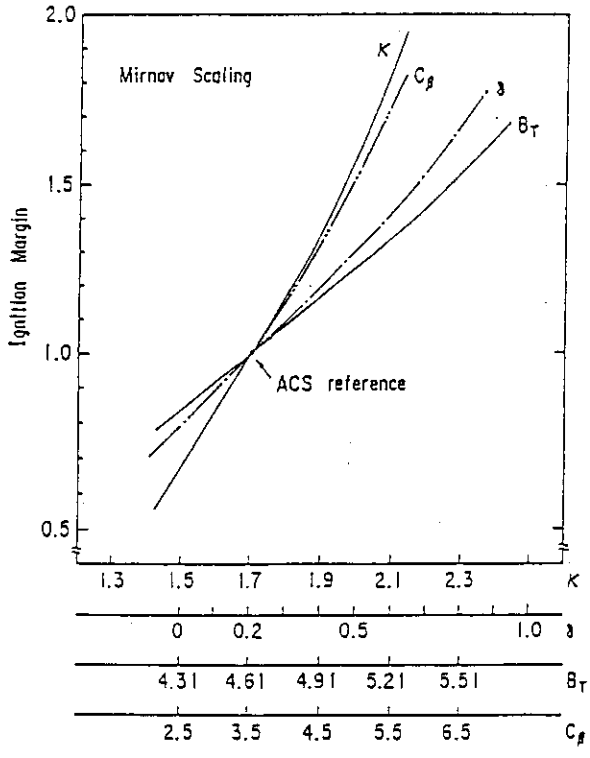

Fig. 8.2 Sensitivity for increase of ignition margin with respect to the increase of elongation (δ), triangularity (κ), field on axis (B_T), Troyon coefficient (C_β).

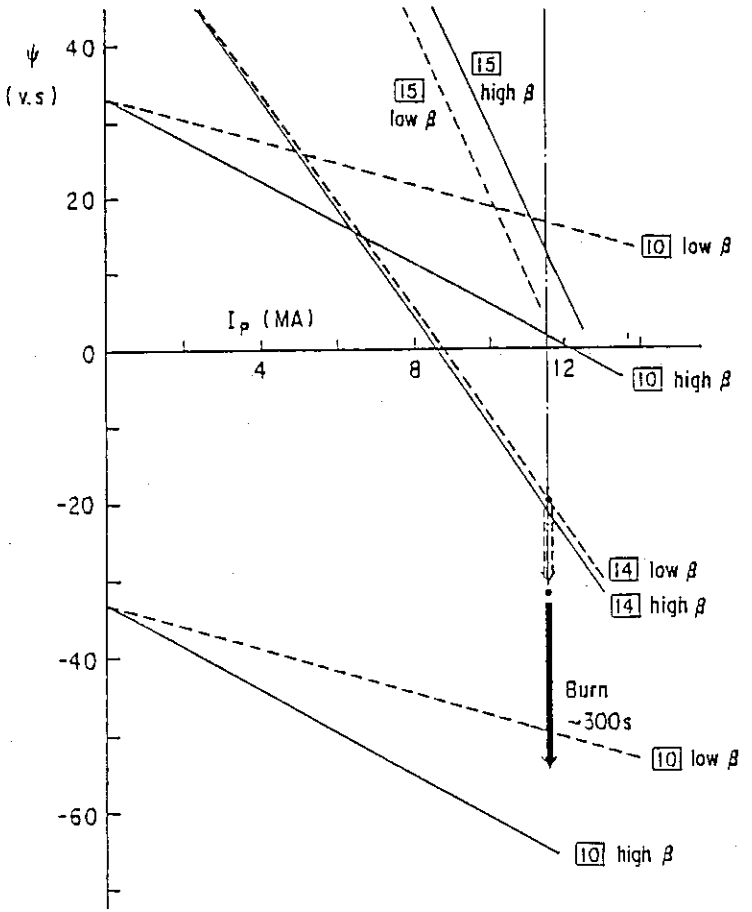

Fig. 8.3 Operation region in plasma current I_p and supplied volt-second ψ space for enlarged plasma. Solid lines denote the limiting lines by maximum field in high beta plasma and dashed lines in low beta plasma, respectively. Lines of #15 coil move upward, since the null point approaches the coil due to the enlargement of plasma size.

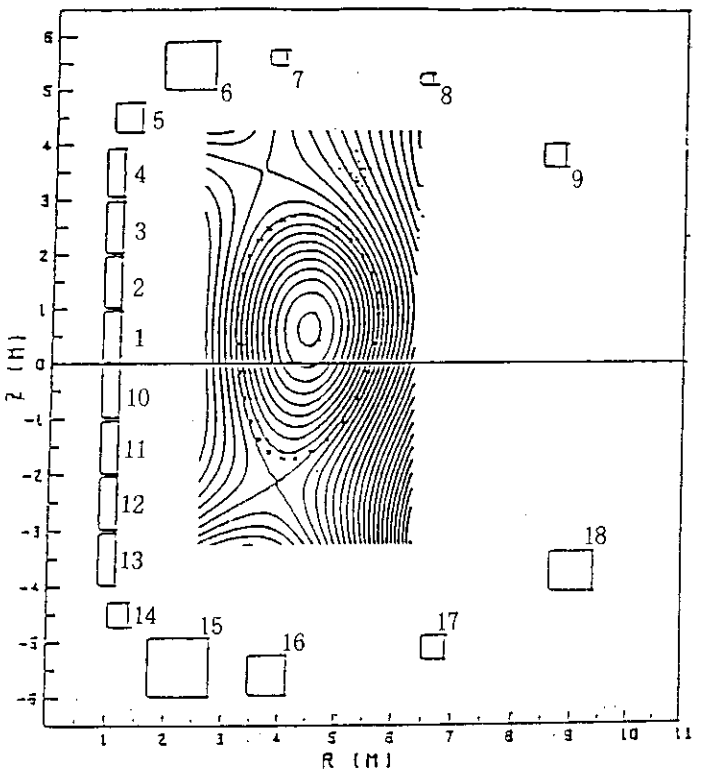

Fig. 8.4 Plasma equilibrium and coil location of ACS reference reactor.

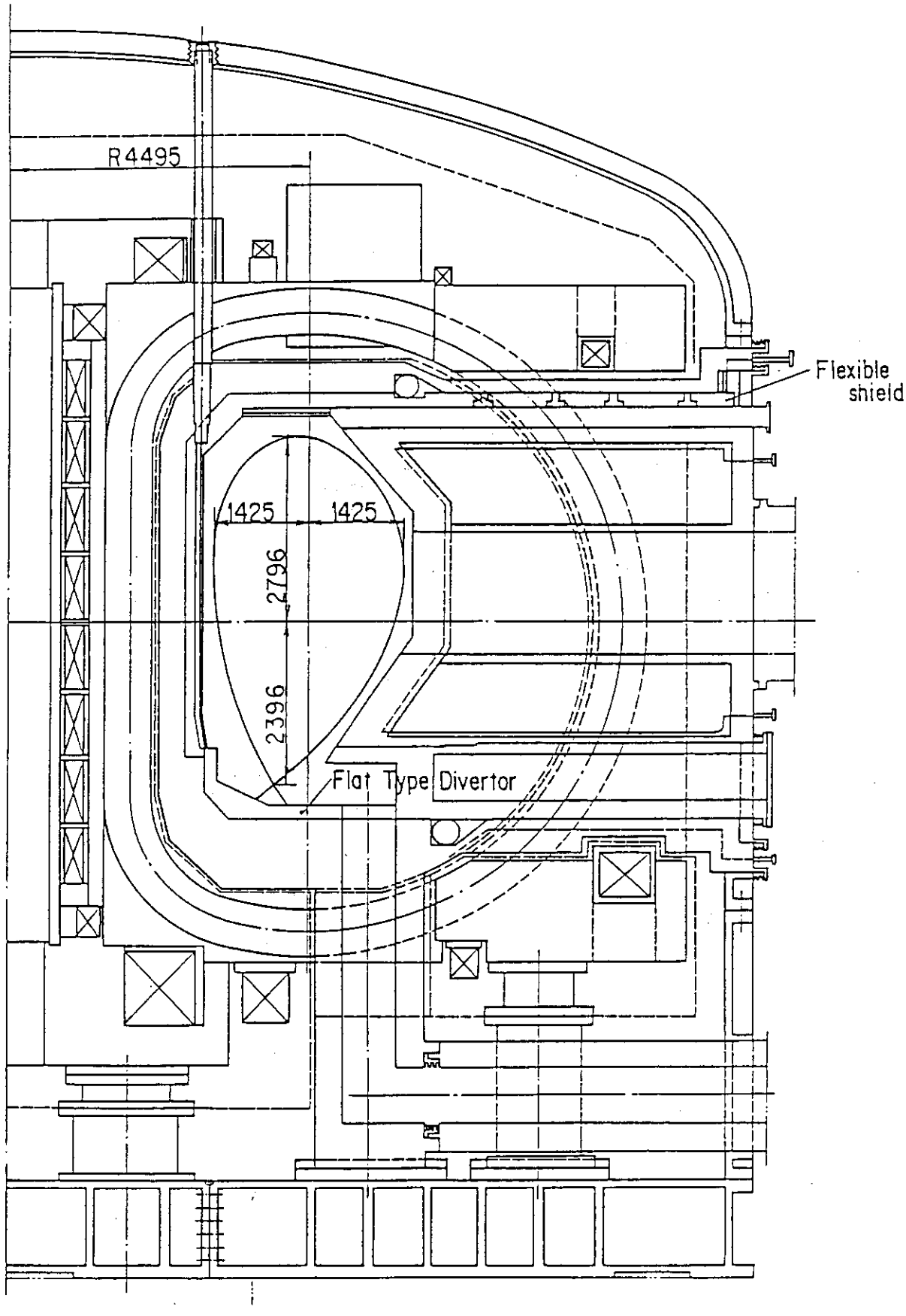

Fig. 8.5 Cross sectional view of enlarged plasma.

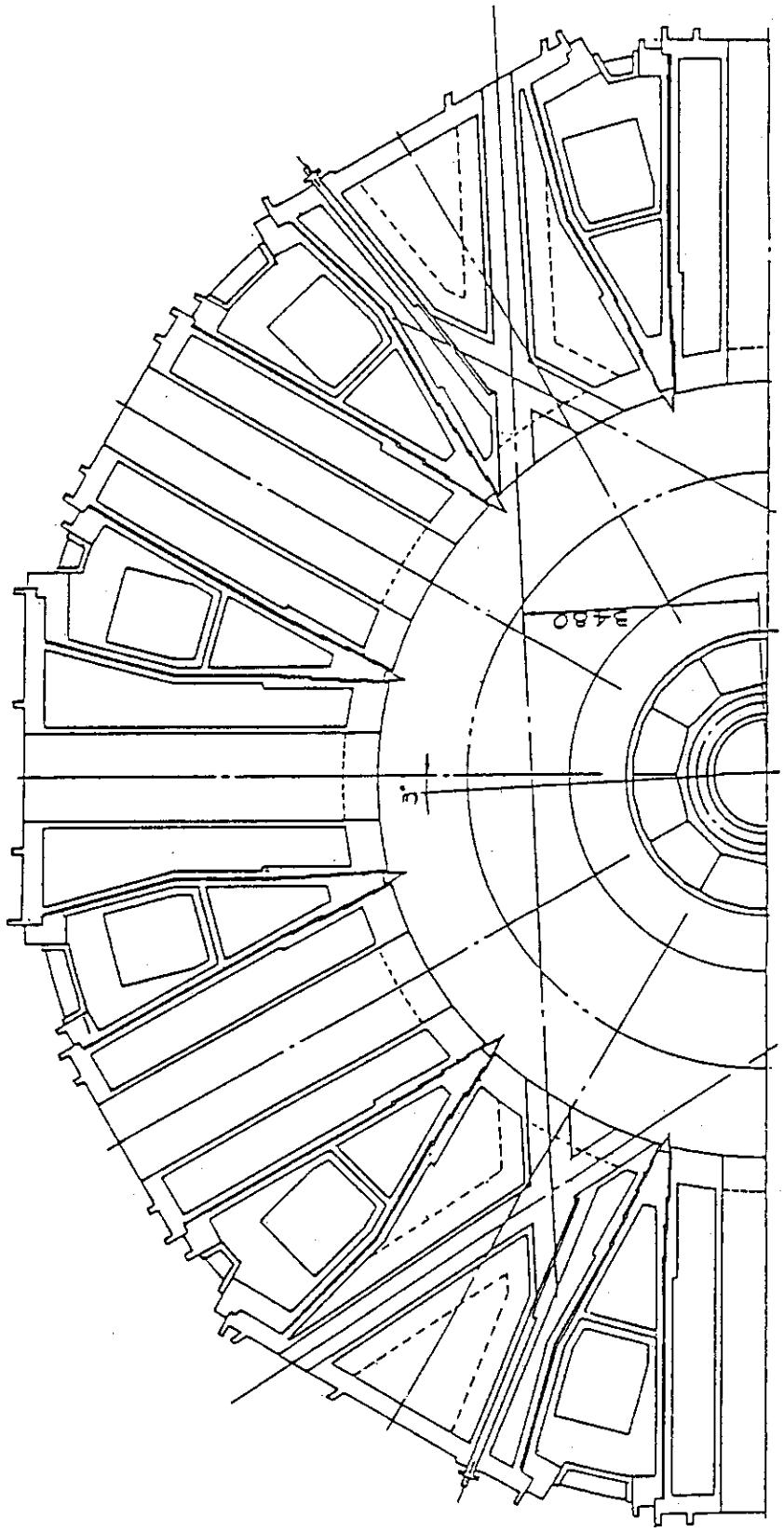

Fig. 8.6 Plane view of ACS reference reactor, where tangential injection NBI and RF systems are installed simultaneously.

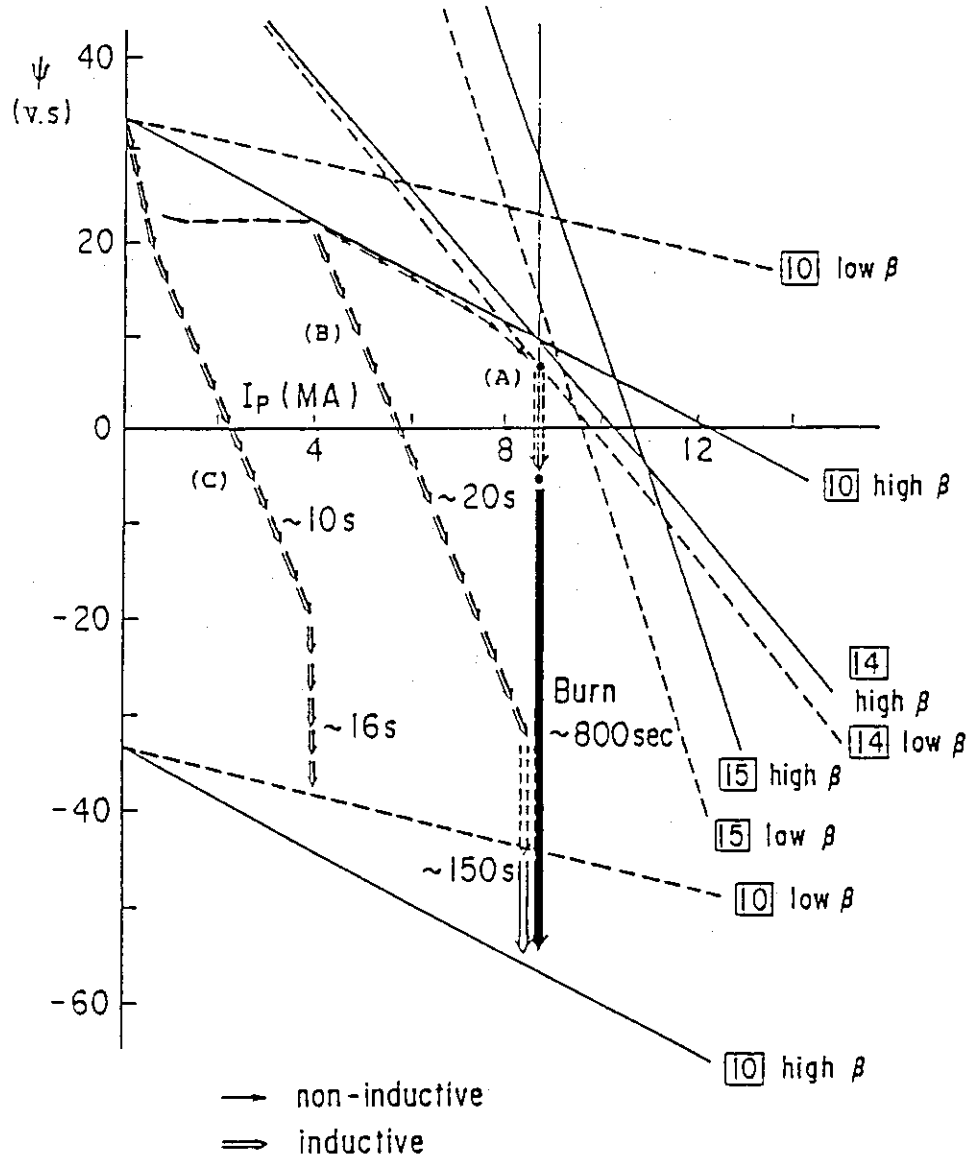

Fig. 8.7 Operation region in plasma current I_p and supplied volt-second ψ space for reference ACS plasma. Solid lines denote the limiting lines by maximum field in high beta plasma and dashed lines in low beta plasma, respectively. Path (A) denotes non-inductive current ramp-up scenario. Path (B) denotes the scenario, where plasma current is ramped-up to 4 MA non-inductively, and subsequently ramped-up inductively. Path (C) denotes the full inductive operation.

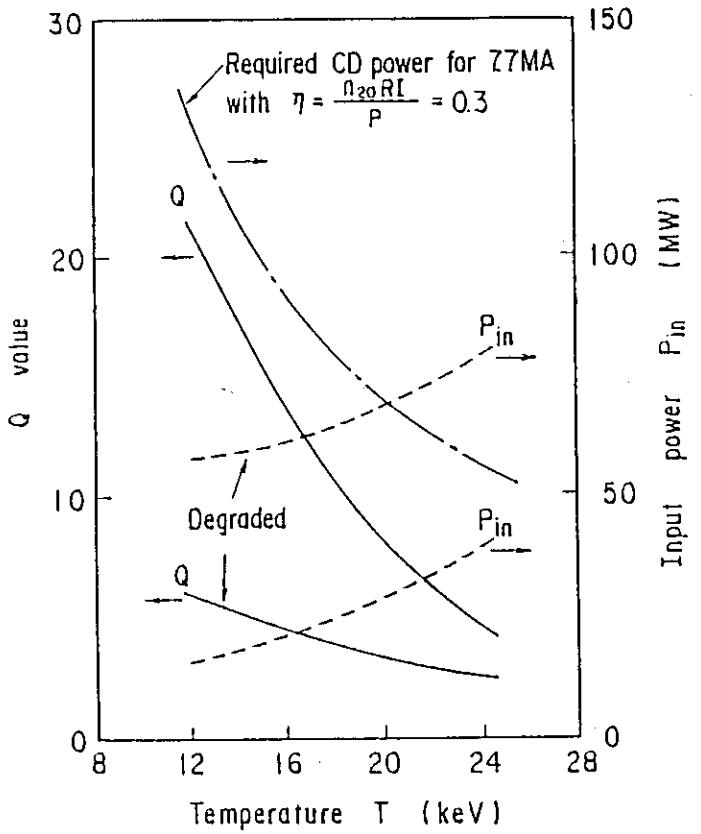

Fig. 8.8 Advanced operation scenario with small plasma size due to installation of breeding blanket. Solid lines denote available Q values for reference Mirnov type scaling (upper line) and degraded confinement by a factor of 1.5 (lower line). Dashed lines are required heating power for the respective Q values. Solid-dashed line shows the required current drive power for current drive efficiency $\eta=n_{20}RI/P=0.3$.

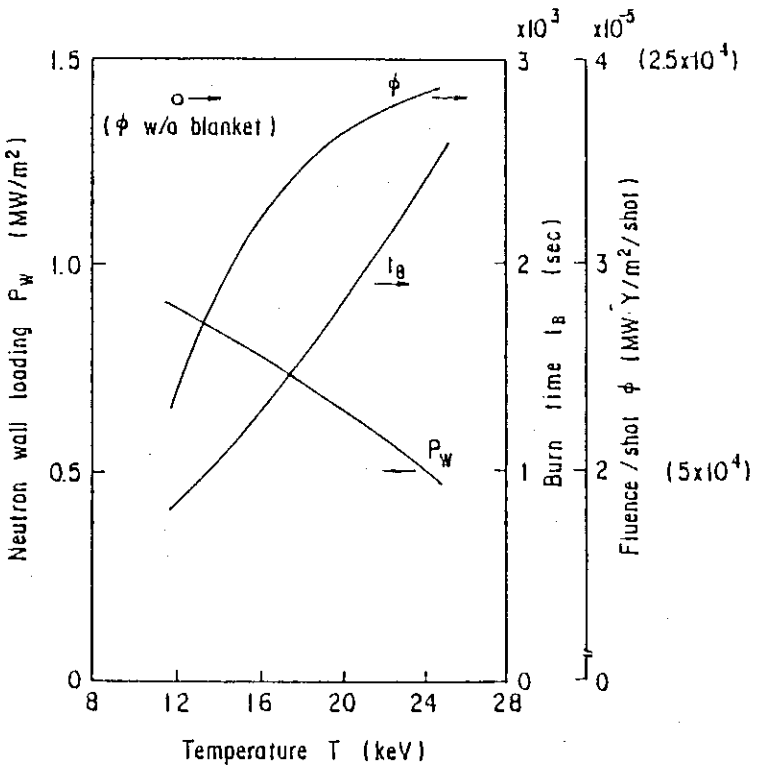

Fig. 8.9 Neutron wall loading P_W, burn time t_B, available fluence during one shot burning ϕ with respect to plasma temperature T in advanced operation scenario.

9. System analysis of INTOR-like design

The critical analysis of INTOR-like designs was implemented as a home task of engineering group at the session XIV in December 1986. The purpose of this analysis is to clarify the reasons why the INTOR-like designs differ from each other. The results of this analysis is expected to give useful data base for discussing ITER design concept.

Some of the necessary input for this analysis was discussed and prepared at the Specialist Meeting on the next generation device in March 1987. However, the information about the design methods employed by other parties, which is essential for this analysis, has not been obtained enough. Nevertheless, we conducted comparative studies between INTOR and FER and between NET and FER.

At the session XIV the analytic procedure was defined as a global comparison of each country's INTOR-like design. Then later at the session XV, sensitivity analysis by changing single design option, for example shield thickness, was added. The later process has been done based on the own national INTOR-like design.

9.1 Representation of INTOR-like Designs

9.1.1 Comparison of physics assumption

Each deligation has its own systems analysis code in order to optimize reactor design. In these calculational code many assumptions have been made to model plasma characteristics and components engineering designs and they differ between countries. One of the most significant difference is in the power balance considertion. FER takes radiation loss into account as energy loss term while INTOR and NET neglect it. For energy confinement various scaling laws are used. However all deligation except TIBER employs H mode type scalings.

Troyon scaling is employed by every deligation for the beta limit with a little different coeffficient. For Z_{eff} the difference is small except those employed by NET design. the ratio of total beta and fuel beta differs from 1.6 in TIBER to 1.2 in INTOR. The difference comes from the choise of Z_{eff} and fast α pressure contribution which largely depends on plasma temperature. For safety factor differes in two aspects, namely defined magnetic surface and plasma model (cylinder or

tours). INTOR and OTR employs cylinder model, FER and TIBER torus model and defined on 95% ψ_p and NET torus model and defined on the separatrix. There is some confusion between plasma specifications and the Physics in INTOR design. For example, the ratio of β and β_{DT} should be 1.19 according to the specifications, but 1.28 (at 10 keV) in the Physics constraints. The elongation of 1.6 described at both specifications and Physics is not the averaged elongation but the elongation at the non-null point side (or upper side) according to a plasma configuration figure. The averaged elongation should be about 1.75 on the surface defined by 95% of ψ_p.

9.1.2 Benchmark calculation of INTOR-like design

Japanese delegation has performed a benchmark study reproducing design parameters of INTOR and Next Step Machines of participating countries by using our own systems code. As mentioned in the previous section, there are lots of differences in the plasma physics assumptions. However we tried to reproduce other country's machine design by chainging algorithm and input of the systems analysis code. Generally, plasma parameters of each delegation are well reproduced implying that the differences of plasma physics assumptions among the parties are well understood.

For the engineering design, electromagnetic quantities are reproduced fairly well. Difference observed is in the evaluation of the stress intensity of the coils. Those difference may come from difference of the conductor design and assumptions made for structural properties, including the load ratio transfered from conductor to coil case.

9.2 Sensitivity Analysis

The analysis is conducted in two ways, that is, global and individual sensitivity analyses. Since some design options are closely related, for example, plasma elongation and selection of single or double null divertor, comparison of sets of certain design options gives us realistic effect on the machine design. We mainly examine those effects between INTOR and FER, and between NET and FER by substituting each physics and engineering constraints and design features.

For individual sensitivity studies

(1) With few exception the changes which increase plasma major radius generally leads to capital cost increase. (See Fig. 9.3)

(2) The changes which leads to the major radius (R_p) change are divided into the following three groups by the intensity of impact on the capital cost ($\frac{dc}{dRp}$).

Strong impact group:

B_t larger than 12 T, ignition margin, Z_{eff}

Medium impact group:

Shield thickness, safety factor, elongation smaller than 1.7, B_t smaller than 10 T, $\Delta\phi$ larger than 50 v.s.

Week or no impact group:

elongation larger than 1.7, $\Delta\phi$ smaller than 50 v.s.

9.3 Relative cost comparison

Relative cost estimations are carried out for five INTOR-like devices. Itemized direct capital cost breakdown relative to FER/ACS is shown in Fig. 9.4. The total construction costs of INTOR, NET, TIBER, and OTR relative to FER are 116%, 127%, 82%, and 160% respectively. Some remarks for the above results are following:

(1) Basically, the relative cost of five INTOP-like devices appears on a smooth correlation with reactor size. Deviation from the smooth function seems to be different choices of design features/drivers.

(2) FER and TIBER have no tritium breeding blanket. This means a direct cost reduction by that amount.

(3) FER and TIBER chose non-inductive current ramp-up. Other three, INTOR, NET, and OTR choose full inductive current ramp-up as reference operation scenario. Latter operation scenario gives a great impact on electric power supply system.

(4) For a large machine such as OTR, the cost of magnet systems, especially TF coils, becomes a dominant element. It is, on the other hand, greatly saved for smaller machine such as TIBER.

On the other hand, in order to have more clear individual effect, sensitivity study of single design option based on its own machine design by each country has been added at the last session.

Japanese sensitivity analysis has been performed using the TRESCODE which was developed at JAERI for effective study of conceptual design of tokamak machine.

The results of the both of global and individual sensitivity studies are summarized as follows:

For the global sensitivity studies

Figures 9.1 and 9.2 shows the global impacts on the radial build and cost of machine.

(1) The preliminary result of cost estimations reveals that the cost of INTOR device is about 16% higher than that of the FER device.

(2) Plasma parameter sets of the both NET and FER machines give almost same ignition margin when the same Mirnov type scaling law and FER power balance equation is used. However, some physics constraints, for example ion composition, safety factor etc., are assumed more conservatively in NET design. If FER physics assumptions and constraints are introduced in NET design, plasma major radius decreases by about 60 cm, and cost ~11%.

(3) Substitution of NET engineering constraints with those of FER, almost gives no effect on the thickness of TF coil and shield/blanket, then plasma major radius. The difference of allowable TF ripple values (FER: ±0.75%, NET: ±1.2%) gives different TF coil bore (~15 cm). However, the cost difference can be expected to be not so large.

(4) Compactness and cost reduction of the devices will be carried out mainly by choices of some design features such as (1) high noncircularity (2) hybrid operation scenario (3) thinner shield thickness associated to lower life time fluence.

(5) There is little impact on the INTOR design by substituting FER Physics.

(6) PFC design constraints in INTOR Engineering is rather conservative than FER.

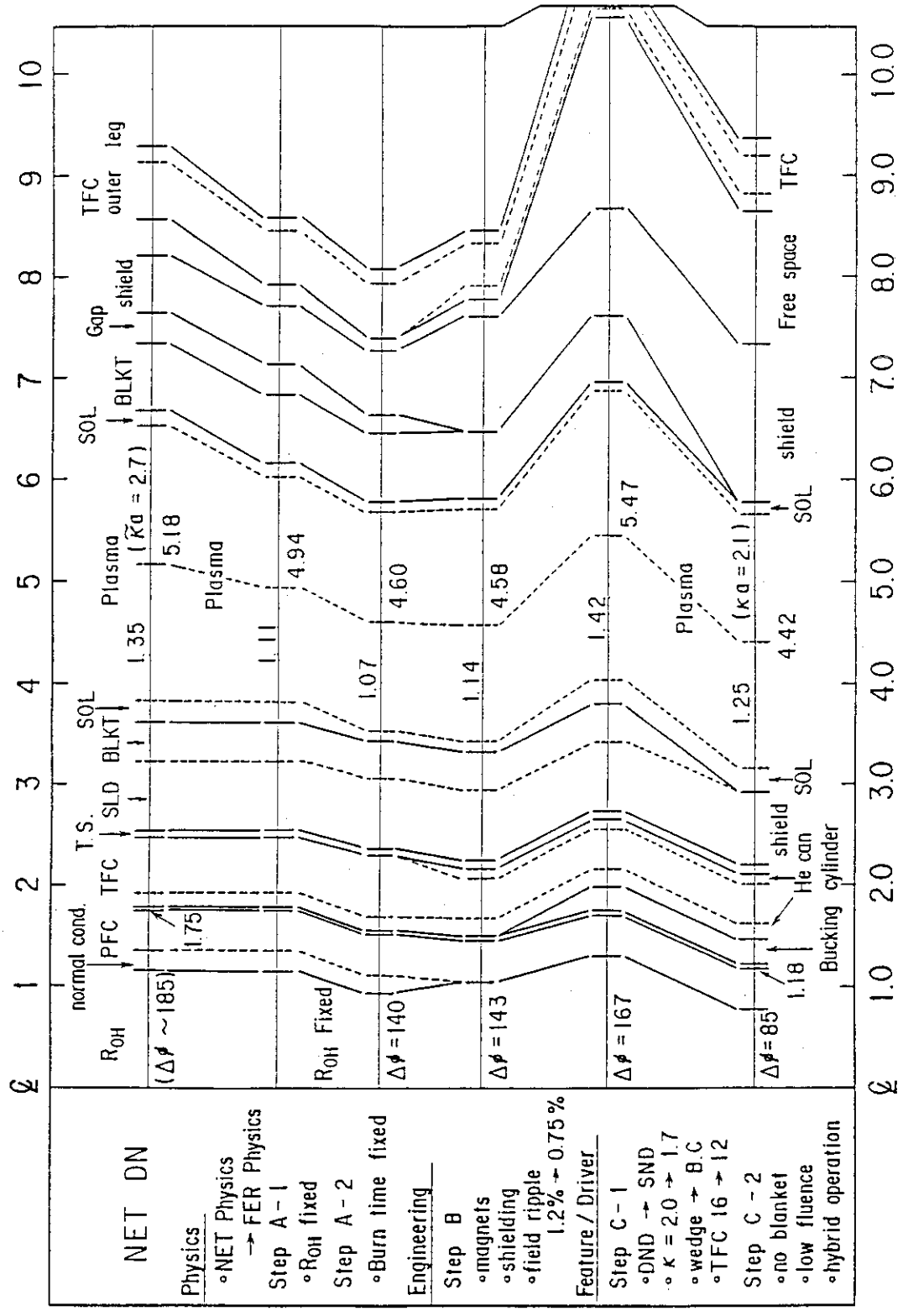

Fig. 9.1 Radial- build comparizon for NET and FER

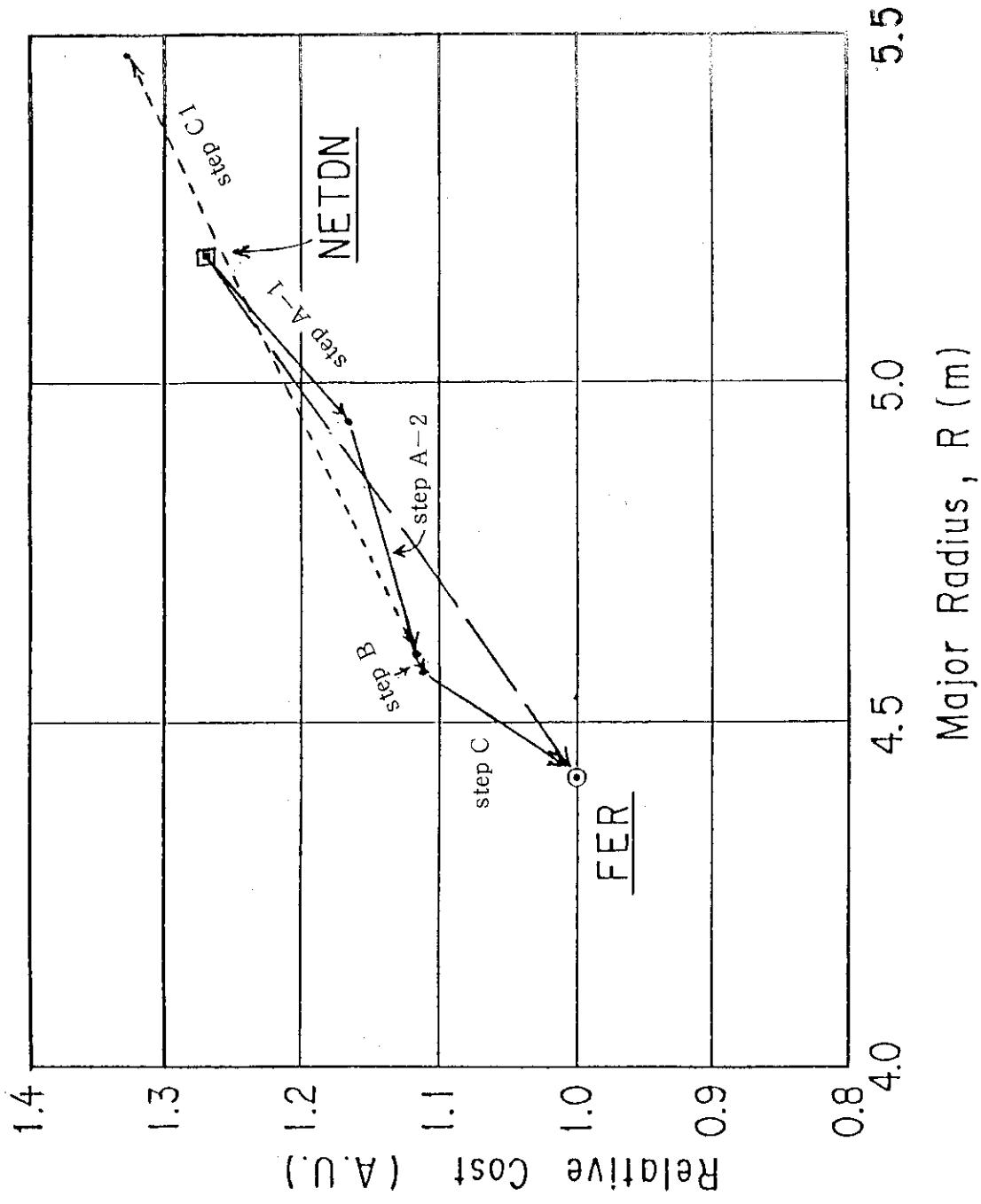

Fig. 9.2 Relative Cost of Each Step From NET to FER

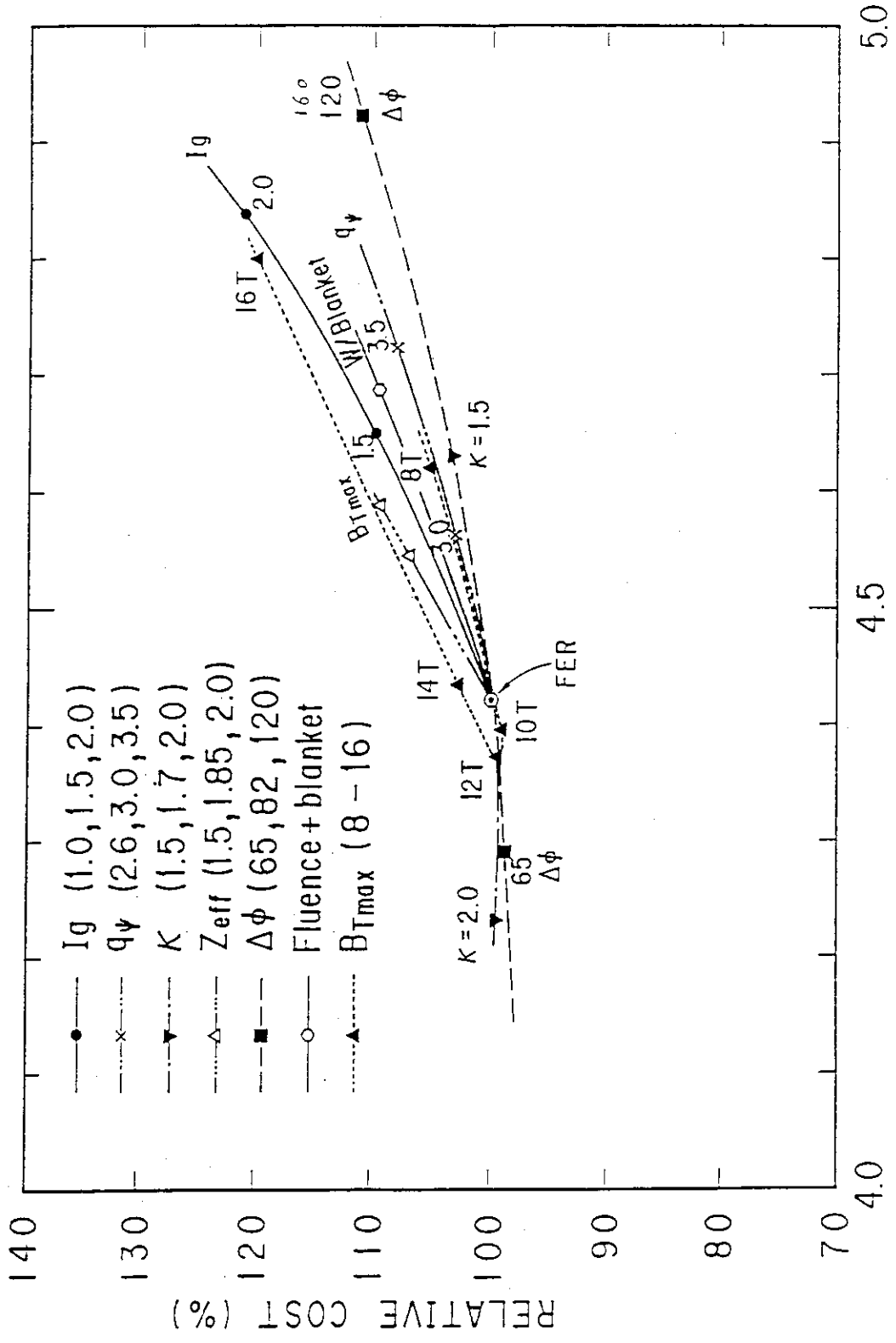

Fig. 9.3 Individual Sensitivity on Relative Cost and Major Radius

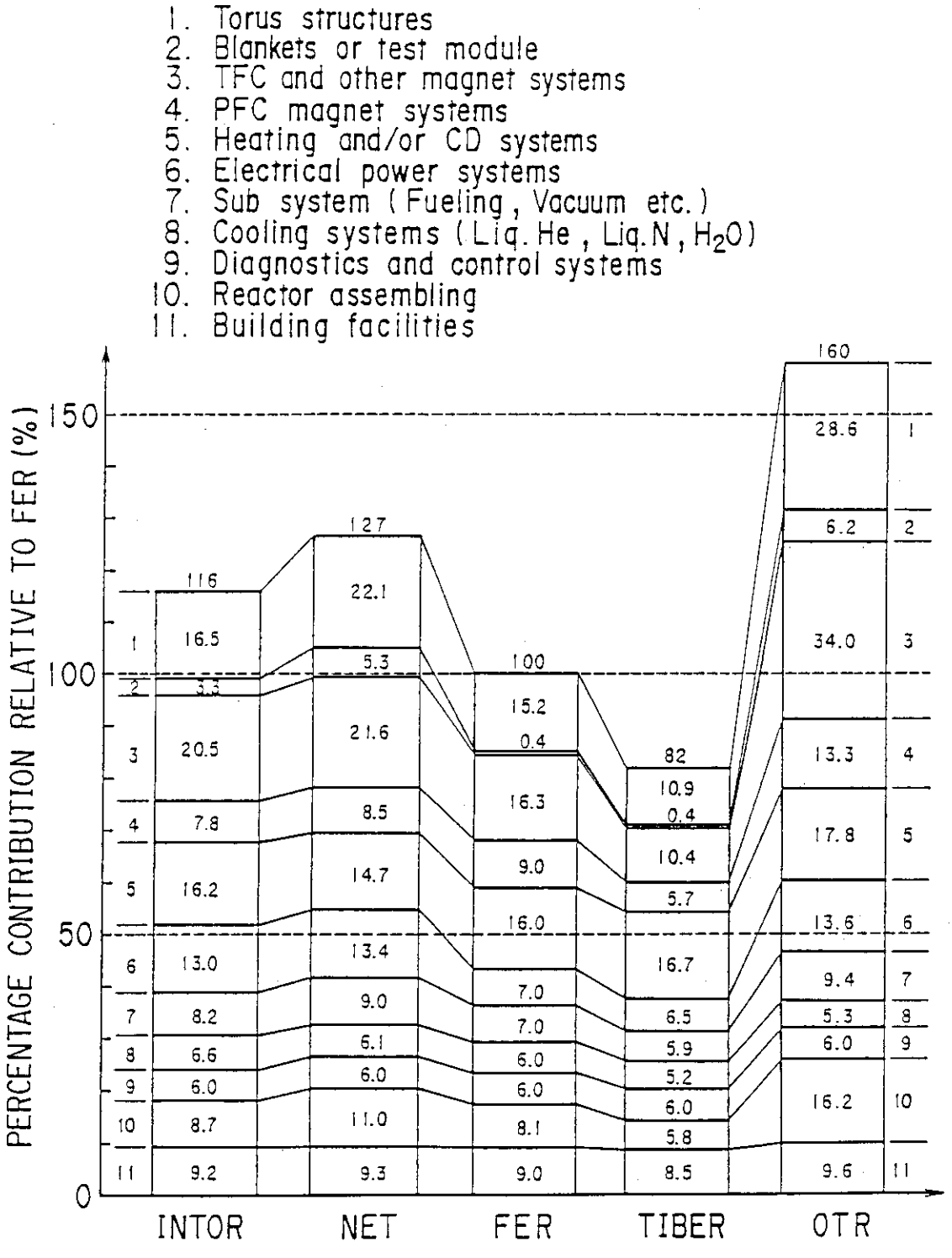

Fig. 9.4 Itemised direct capital cost breackdown relative to FER evaluated by TRESCODE.

References for Chapter Ⅱ

[1] INTOR GROUP, International Tokamak Reactor: Zero Phase(Rep. Int. Tokamak Reactor Workshop Vienna, 1979), International Atomic Energy Agency, Vienna(1980); see also Summary in Nucl. Fusion 20(1980)349.

[2] INTOR GROUP, International Tokamak Reactor: Phase One(Rep. Int. Tokamak Reactor Workshop Vienna, 1980-81), International Atomic Energy Agency, Vienna(1982); see also Summary in Nucl. Fusion 22(1982)135.

[3] INTOR GROUP, International Tokamak Reactor: Phase Two A Part 1(Rep. Int. Tokamak Reactor Workshop Vienna, 1981-83), International Atomic Energy Agency, Vienna(1983); see also Summary in Nucl. Fusion 23(1983)1513.

[4] INTOR GROUP, International Tokamak Reactor: Phase Two A Part 2(Rep. Int. Tokamak Reactor Workshop Vienna, 1984-85), International Atomic Energy Agency, Vienna(1986); see also Summary in Nucl. Fusion 25(1985)1791.

[5] INTOR GROUP, International Tokamak Reactor: Phase Two A Part 3(Rep. Int. Tokamak Reactor Workshop Vienna, 1985-87), International Atomic Energy Agency, Vienna(1988) (to be published).

[6] Report of a Specialists' Meeting on Tokamak Concept Innovations, (January 1986) IAEA-TECDOC-373.

[7] Report of IAEA INTOR-related Specialists' Meeting on Non-inductive Currnt Drive,(September 1986) IAEA-TECDOC-441.

[8] Report of INTOR-Related IAEA Specialists' Meeting on Engineering Test Reactor National design Concepts, (March, 1987), which is included in ref. [5].

[9] Report of INTOR-Related IAEA Specialists' Meeting on Plasma Disruptions, which is included in ref. [5].

[10] T. Mizoguchi, et al.,JAERI-M 88-045.

[11] T. Tsunematsu, et al., JAERI-M 88-029.

[12] K. Okano, et al., JAERI-M 87-209.

[13] Y. Kishimoto, et al., JAERI-M 87-204.

[14] K. Ushigusa, et al., JAERI-M 88-023.

[15] M. Kasai, et al., JAERI-M 88-010.

[16] H. Iida, et al., JAERI-M 88-011.

[17] T. Kobayashi, et al., JAERI-M 87-219.

[18] N. Fujisawa, et al., JAERI-M 87-093.
[19] R. Saito, et al., JAERI-M 87-137.
[20] M. Sugihara, et al., JAERI-M 87-216.
[21] T. Mizoguchi, et, et al., JAERI-M 88-062.
[22] A. Hatayama, et al., JAERI-M 88-006.
[23] K. Yoshioka, et al.,JAERI-M 87-177.